ATTENUATION STRUCTURE IN CENTRAL ANATOLIA USING BELBAŞI – KESKİN BOREHOLE ARRAY

by

Korhan Umut Şemin

M.S., Geophysics, Boğaziçi University, 2006

Submitted to the Kandilli Observatory and Earthquake
Research Institute in partial fulfillment of
the requirements for the degree of
Doctor of Philosophy

Graduate Program in Geophysics

Boğaziçi University

2018

ATTENUATION STRUCTURE IN CENTRAL ANATOLIA USING BELBAŞI – KESKİN BOREHOLE ARRAY

APPROVED BY:

Prof. Dr. Hayrullah Karabulut .....
(Thesis Supervisor)

Prof. Dr. Nurcan Meral Özel .....
(Thesis Co-supervisor)

Assoc. Prof. Gülüm Tanırcan .....

Prof. Dr. Eşref Yalçınkaya .....

Prof. Dr. Semih Ergintav .....

Prof. Dr. Şerif Barış .....

DATE OF APPROVAL: 08.10.2018

ACKNOWLEDGEMENTS

First and foremost, I would like to thank my parents and my sister, who gave me unrequited support and encouragement throughout my thesis studies. I thank sincerely to my fellow colleagues at Belbaşı Center for their confidence in me and making me comfortable to study at my will over the years.

I am grateful to my advisor/director Nurcan MERAL ÖZEL for accepting me as her student and her valuable guidance and support along my career. I am also grateful to my professors at Kandilli Observatory ERI Geophysics department for wonderful lessons during my studies. I thank to my thesis committee for their significant comments and suggestions.

Last but definitely not least, I thank my wife for the joy she brings into my life. She has inspired me since the moment she entered my life.

ABSTRACT

ATTENUATION STRUCTURE IN CENTRAL ANATOLIA USING BELBAŞI – KESKİN BOREHOLE ARRAY

The Multiple Lapse Time Window (MLTW) method has been applied to investigate the dominant attenuation mechanism of Central Anatolia region by separating scattering attenuation and intrinsic absorption that are affecting the seismic wave amplitudes. A total of 177 local earthquakes with magnitudes varying between 2.5 – 4.7 and hypocentral distances between 5 to 150 km recorded during 2008-2011 by two borehole type broadband seismometers as well as KOERI seismic stations were selected according to the criterion defined by SNR $>$ 3 (Signal-to-Noise Ratio). The single station approach of the MLTW allowed us to characterize the lateral variations of attenuation in the region by calculating the attenuation around each station individually for frequencies 1.5, 3, 6, 8, 9 Hz. Moreover, average attenuations were also estimated representing the whole region of Central Anatolia. Final results were compared with other studies conducted in different regions around the world. Results of this study show that for frequencies 3 Hz and higher the intrinsic absorption is more prominent than scattering attenuation for the whole of Central Anatolia, especially at south and southeastern parts due to Quaternary volcanism. Comparison of attenuation with different regions indicates that the Eastern Anatolia has higher attenuation than Central Anatolia whereas Western Anatolia has comparable values of attenuation.

ÖZET

BELBAŞI - KESKİN SİSMİK DİZİNİMİ VERİSİYLE ORTA ANADOLUDA SOĞURULMA YAPISI

Bu çalışmada, Orta Anadolu bölgesinde yayılan sismik dalgaların genliklerini etkileyen baskın soğurulma mekanizmalarından içsel soğurulma (anelastisite) ve saçılım soğurulması, MLTW (Multiple Lapse Time Window) yöntemi kullanılarak belirlenmiştir. Çalışmada 2008 ve 2011 yılları arasında büyüklükleri 2.5 ile 4.7 arasında değişen ve odak uzaklıkları 5 - 150 km arasında kalan 177 deprem verisi kullanılmıştır. Çalışmadaki veriler, iki kuyu tipi genişbantlı sismik dizinim istasyonlarına ek olarak, KRDAE'nin istasyonları tarafından da kaydedilen ve Sinyal/Gürültü oranı 3 ve üzerinde olan depremler arasından seçilmişdir. 1.5, 3, 6, 8 ve 9 Hz frekans bantları için MLTW yönteminin tek istasyon yaklaşımı kullanılarak her bir istasyonun çevresindeki soğurulma değerleri hesaplanmış ve soğurulmanın yanal değişimleri gözlemlenmiştir. Ek olarak ortalama soğurulma değerleri hesaplanarak bölgeyi temsil eden tek bir ortalama soğurulma değeri hesaplanmıştır. Bulunan sonuçlar dünya'nın farklı bölgelerinde aynı yöntem ile yapılan çalışmaların sonuçlarıyla karşılaştırılmıştır. Özellikle 3 Hz ve üzerindeki frekanslar için Orta Anadolu'da içsel soğurulmanın saçılmaya oranla daha hakim bir rol oynadığı görülmektedir. Bölgenin Güneyi ve Güneydoğusu Kuvaterner volkanizmaya da bağlı olarak en yüksek toplam soğurulmaya sahiptir. Doğu Anadolu'nun Orta Anadolu'ya oranla daha yüksek soğurulma gösterdiği, Kuzey-Batı Anadolu'nun soğurulma seviyesinin ise Orta Anadolu'yla benzer olduğu sonucunu elde edilmiştir.

TABLE OF CONTENTS

LIST OF FIGURES

LIST OF TABLES

LIST OF SYMBOLS

A_0	Initial seismic wave amplitude
$A(x)$	Seismic wave amplitude at distance x
A_{obs}	Observed mean-squared wave amplitude envelope
A_{syn}	Synthetic mean-squared wave amplitude envelope
B_0	Seismic albedo
e_n	Integrated energy density
$E_{n\ obs}$	Normalized observed energy density
$E_{n\ syn}$	Normalized synthetic energy density
f	Frequency
g	Scattering coefficient
h	Intrinsic absorption strength
L_e^{-1}	Extinction Length of S-wave energy
Q	Quality factor
Q_P	P-wave Quality factor
Q_S	P-wave Quality factor
Q_c^{-1}	Coda attenuation
Q_i^{-1}	Intrinsic attenuation
Q_s^{-1}	Scattering attenuation
Q_t^{-1}	Total attenuation
r	Hypocentral distance
r_m	Hypocentral distance of m^{th} seismogram
t_{ref}	A fixed reference lapse time
t_s	Arrival time of S-wave
c	Seismic wave velocity
w	Angular frequency

LIST OF ACRONYMS/ABBREVIATIONS

BNTMC	Belbaşı Nuclear Tests Monitoring Center
CAFS	Central Anatolia Fault System
CSS3.0	Center for Seismic Studies data format 3.0
CTBTO	Comprehensive Nuclear Test-Ban Treaty Organization
DEPAR	Deprem Sonrası Acil Gözlem Araştırmaları
EAFS	East Anatolia Fault System
F/K	Frequency-Wavenumber Analysis
GMT	Generic Mapping Tools
IMS	International Monitoring System
İAESZ	İzmir-Ankara-Eskişehir Suture Zone
İEFS	İzmir-Eskişehir Fault System
KB	Kırşehir Block
KOERI	Kandilli Observatory and Earthquake Research Institute
MLTW	Multiple Lapse Time Window Method
NAFS	North Anatolia Fault System
RETMC	Regional Earthquake and Tsunami Monitoring Center
SAC	Seismic Analysis Code
TGFZ	Tuz Gölü Fault Zone
TÜBİTAK	The Scientific and Technological Research Council of Turkey

1. INTRODUCTION

Determining the attenuation variation within the lithosphere, especially when combined with velocity studies would yield valuable results for tectonic processes that are dominant in the region of interest. The common methods of attenuation studies from short-period S-waves either directly or using decay rate of coda, estimate a total attenuation value that is a combination of scattering Q_s^{-1} and intrinsic absorption Q_i^{-1}. However, those methods do not estimate the relative contributions of each type of attenuation present within a region. Since the mechanisms that cause a specific attenuation are different, separating the attenuation contribution in a region allows us to quantify the underlying processes that effect the seismic wave propagation and gives better insight on the lithospheric structure of the study region.

Following the two mid-sized earthquakes (Ml 5.7, 5.5) occurred within a week (20-27 Dec 2007) near the town of Bala, a district of the capital city Ankara, it was necessary to quantify the seismic hazard and the crustal structure in the Central Anatolia region. These earthquakes were felt strongly in cities such as Ankara, Bolu, Kırşehir, Yozgat, Aksaray, and the surrounding villages. Initial reports indicated that no one was killed, but the damage was considerable, especially in the villages. Tan et al. [1] studied the event aftershocks using temporary stations deployed immediately after the first mainshock. They pointed out the importance of these recent Bala earthquakes as they are in close proximity to Tuz Gölü Fault which has been quiet for some time and their noticeable effects in nearby populated areas. Previous powerful earthquakes that occurred in Ankara and its vicinity are as follows; Kırşehir-Keskin earthquake (1938-M=6.6), Bolu-gerede (1944-M=7.3), Kulu-Bala (1983 M=4.7), and again in Bala (2005 M=4.9).

The Keskin Seismic Array located in town Keskin (Kırıkkale) 60 km NE of the epicenters of the mainshocks recorded more than 1100 aftershocks with Ml magnitudes ranging from 1.5 to 5.0 within this one-week period. Keskin array is a short period circular array with 6 SP and one BB instrument in the centre. This array

was established in the 1950s and had seen a couple of upgrades over the years. It is currently operated by Kandilli Observatory and Earthquake Research Institute (KOERI) – Belbaşı Nuclear Tests Monitoring Center (BNTMC) in Ankara and is one of the certified primary stations of the International Monitoring System (IMS) of the Comprehensive Nuclear Test-Ban Treaty Organization (CTBTO) used in the global monitoring of nuclear explosions. The most important feature of the array, apart from the array processing techniques, is that the instruments are installed at boreholes and therefore, have very good background noise levels compared to surface installations. Consequently, the seismic data recorded by the array is very high quality and suitable for scientific studies. In this thesis, I have utilized the high-quality array data along with data from other stations operated by KOERI - Regional Earthquake-Tsunami Monitoring Center (RETMC) in order to study the regional attenuation structure of Central Anatolia. This study would also be beneficial to the nuclear test monitoring activities by contributing to the regional crustal models with more detailed attenuation structure measurements. Moreover, it will help in predictions of earthquake-generated ground-motion in making decisions for earthquake regulations for buildings.

1.1. Previous Studies

There have been numerous seismic studies using local and regional earthquakes to investigate the high frequency S-wave attenuation in a wide variety of regions all around the world. However, I have listed here the researches that only utilize the Multiple Lapse Time Window (MLTW) method to separate the scattering and intrinsic absorption effects. Fehler et al. [5] defined and applied the method for Kanto-Tokai region of Japan, using 20 local earthquakes recorded by 66 stations with focal depths lower than 50 km and using three time-windows (0-15s, 15-30s, 30-100s) to integrate the energy density. Similarly, Hoshiba [6] applied this technique to all Japan using the single-station approach in order to investigate the spatial variation of the attenuation. Attenuation curves for Central California, Long Valley and Hawaii regions estimated by Mayeda et al. [7] for frequency range of 1.5Hz to 15 Hz using MLTW. Following Mayeda's research, Jin et al. [8] investigated the relative contribution of scattering and

intrinsic absorption in southern California for 1.5 to 6 Hz and between 12 to 24 Hz frequency ranges. For southern Spain and Northwest Anatolia, Akinci et al. [9] applied the MLTW to local earthquakes for attenuation structure using different frequency ranges for the two studied regions. Pujades et al. [10] measured the Q_t^{-1}, Q_i^{-1} and Q_s^{-1} in the Almeria basin of the southern Iberia while Canas et al. [11] studied the Canary Islands for the relative effects of the scattering and intrinsic attenuation using local earthquakes. In the same year, Ugalde et al. [12] using coda waves separated the total attenuation of Northeastern Venezuela to find spatial variations of scattering and intrinsic components. Dominant attenuation mechanism around the Erzincan basin of North Anatolia Fault zone was investigated by Akinci and Eyidoğan [13] using the MLTW method for five centre frequencies between 1.5 to 12 Hz with local earthquakes in the hypocentral distances smaller than 45 km. These studies assumed uniform velocity and spatial uniformity of scattering and intrinsic attenuation. Hoshiba et al. [14] investigated the depth dependence of attenuation by comparing the uniform and depth dependent models in the Northern Chile using the MLTW and pointed out the importance of velocity structure when measuring any kind of attenuation. Bianco et al. [15], [16] using numerical simulations of uniform model (uniform velocity in a half space) measured the scattering and intrinsic attenuation in the southern Apennines (2002) and later on studied the depth dependence of attenuation in northeastern Italy in 2005 using the MLTW method. Tuvè et al. [17] also applied the MLTW method to estimate the Q_s^{-1} and Q_i^{-1} in southern Italy and found out that both types of attenuation are almost equally contribute to the total attenuation for frequencies higher than 3 Hz in the region. In southwestern Anatolia, main attenuation mechanism was estimated to be intrinsic absorption rather than scattering processes according to the study by Şahin et al. [18]. Another application of the MLTW method is the study of the attenuation mechanism of Garwhal-Kumaun region in the Himalayas conducted by Mukhopadhyay et al. [19]. He concluded that the region is dominated by scattering attenuation due to high heterogeneity. Carcolé and Sato [20] investigated lateral variation of scattering and intrinsic absorption of S-waves in Japan using the MLTW analysis using a very dense network of Hi-net stations. They were able to map the spatial distribution of both attenuation types in several frequency ranges and compared their results with the

previous work in the same region.

1.2. Tectonic Setting

The Central Anatolia region is surrounded by two major tectonic structures of Turkey namely the North Anatolian Fault (NAF) and the East Anatolian Fault (EAF) and moves westward as a result [21]. Along with the westward motion, Anatolian block rotates counter-clock wise between 25° and 18° from east to west according to several studies ([22–24]). Consequently, these deformations cause several left and right-lateral strike-slip faults with NW-SE and NE-SW directions as can be seen in Figure 1.3 [25].

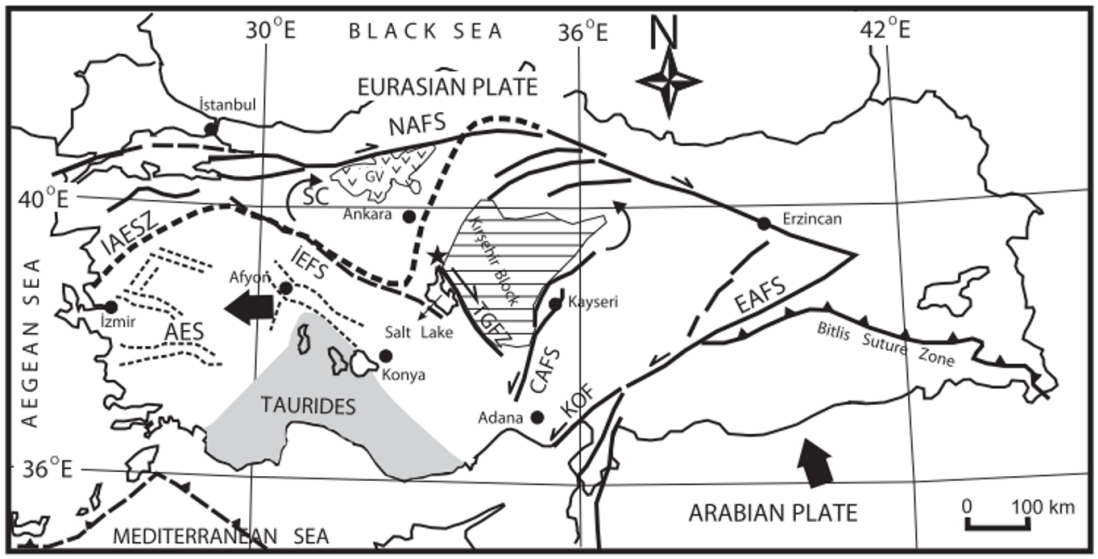

Figure 1.1. Simple tectonic map of Turkey. Major faults featured in the map are North Anatolian Fault System (NAFS), East Anatolian Fault System (EAFS), Central Anatolian Fault System (CAFS), İzmir-Eskişehir Fault System (İEFS), and Tuz Gölü Fault Zone (TGFZ). Bala earthquakes locations are denoted as star symbol on the map. (from Tan et al., [1])

Central Anatolia has a few paleotectonic structures such as the İzmir-Ankara-Erzincan Suture Zone (İAESZ), the Sakarya Continent (SC) İzmir-Eskişehir Fault System (İEFS), and the Kırşehir Block (KB) as shown in Figure 1.1 [1]. The most active fault system of the Central Anatolia is the 200 km long [26] Tuz Gölü Fault System

(TGFS), comprising a NW-SE trending right-lateral strike-slip fault. In addition, many authors also claimed that the TGFS has considerable normal component ([26–28]).

Another important structure in Central Anatolia is the Central Anatolian Fault System (CAFS), with left-lateral strike slip motion located in the east-southeast section of the Anatolian Plate. There is much debate about the existence of this fault system [25]. The region is also separated from the Isparta Angle by the İzmir-Eskişehir Fault System. Historical seismicity indicates that the western part of the Anatolian Block is more active compared to the eastern part and that the central part has the least activity with the absence of major faults.

Collision of Eurasian and Arabian plates also led to very dominant volcanism in the Central Anatolia that started in the Neogene and continued throughout the Quaternary and believed to be sourced from the upper mantle [29].

Many researchers reported low seismic velocities in the upper mantle characterized by a hot and thin lithospheric mantle in the Anatolian plateau including the Central Anatolia ([30–34]).

1.3. Seismic Wave Attenuation

In a perfectly elastic Earth, seismic waves once excited would propagate indefinitely. However, the real Earth is not homogeneous or perfectly elastic, and seismic waves lose energy and attenuate with time due to various mechanisms. Observed seismic wave amplitudes decay exponentially with increasing distance. The term attenuation refers to the rate of this energy loss. Study of high-frequency seismic wave attenuation is essential in learning the physical characteristics of the Earth. The amplitude and attenuation of seismic waves depend on three major factors namely, source of the earthquake (size and type), path (the distance of the earthquake to the site and the geology of the medium which the wave travels) and site effects (local geological characteristics), which results in regionally different attenuation values. Attenuation is usually represented by the quality factor Q. In the Earth, the Q value varies inversely

with the attenuation. Large Q values mean low attenuation vice versa. Q is dependent on the frequency at high frequencies (1 Hz and above), and generally increases as the frequency increases. The P-wave Q value is denoted as Q_P and S-wave Q value as Q_S and generally, Q_P is larger than Q_S in the Earth. Q for seismic waves is usually independent of frequency for frequencies lower than 1.0 Hz and varies greatly from region to region, especially with respect to velocity changes as shown in Figure 1.1. Q Quality factor can be described as the ratio of energy loss per cycle to total energy.

$$\frac{1}{Q(w)} = \frac{\Delta E}{2\pi E} \tag{1.1}$$

where E is the total strain energy, w, angular frequency, and ΔE represent the energy loss per cycle. How energy loss is related to amplitude is given by the following relationship,

$$\Delta E = A^2(1 - e^{-2\pi/Q}) \tag{1.2}$$

A very important aspect of attenuation is the definition of the distance parameter; because attenuation is the change of ground motion with location. The equation of seismic wave amplitude as a function of distance can be written as in Shearer [35];

$$A(x) = A_0 e^{-wx/2cQ} \tag{1.3}$$

where x is the distance in the propagation direction, c denotes the seismic wave velocity and A_0 represents the initial wave amplitude. Seismic velocity $c = \alpha$ for P-waves along with the quality factor Q_α and $c = \beta$ for S-waves with quality factor Q_β. Equation 1.3 shows that for a constant value of Q, a high-frequency wave will attenuate more rapidly than a low-frequency wave since the high-frequency wave for a certain distance oscillates more than a low-frequency wave will do [36]. The amplitude decline and number of oscillations can be expressed as complex values with exponential real and

imaginary parts.

$$A(x,t) = A_0 e^{-wx/2cQ} e^{-iw(t-x/c)} \tag{1.4}$$

And then complex exponential parts of the equation 1.4 can be combined to incorporate the effects of Q to the calculation of synthetic seismograms in seismic survey techniques such as reflection studies [35]. According to equation 1.3, a 1 Hz seismic wave with a velocity of 5 km/s propagating 100 km within a medium with quality factor of Q= 100 will keep only 53% of its initial amplitude.

Like seismic velocities, attenuation is also very sensitive to the variations in temperature within the earth. In tectonically active regions, attenuation is more pronounced than in the other regions due to the high heat flow and because of this feature, Q measurements can reveal the thermal mechanisms in different depths. A joint study of velocity and attenuation will be even better in resolving the Earth's structure [37].

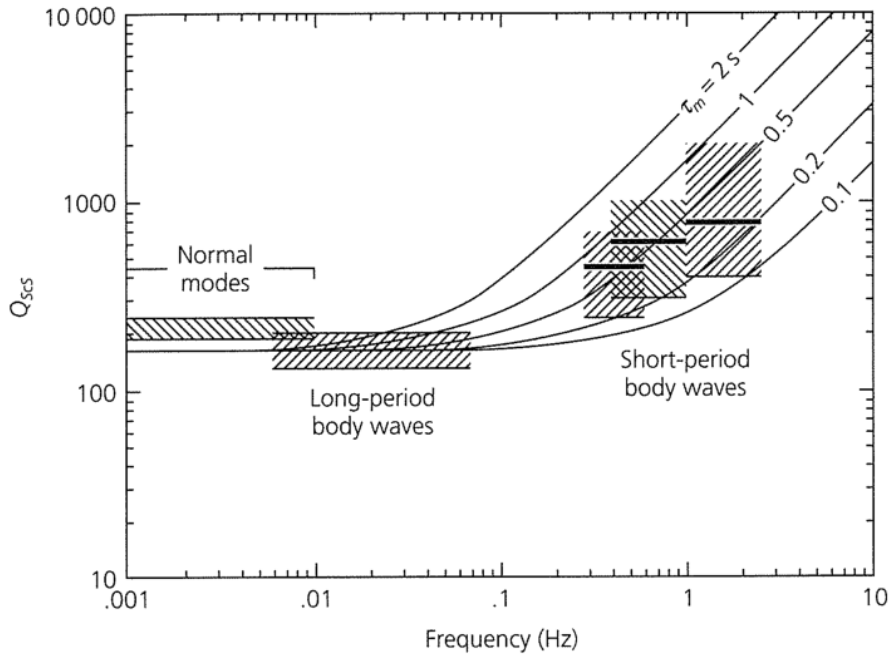

Figure 1.2. Variation of Q with frequency in the mantle. Q value is almost constant for frequencies lower than 1 Hz (From Sipkin and Jordan [2]).

There are two major effects that cause seismic wave attenuation in the Earth, scattering loss and the intrinsic absorption. Scattering loss occurs due to heterogeneities within the medium and depends on the velocity and density variations. On the other hand, intrinsic absorption refers to the conversion of the seismic energy to heat due to anelasticity [6]. It is important to determine the attenuation mechanism since it shows substantial differences in different regions.

1.3.1. Scattering Attenuation

Scattering within the Earth changes the directions of the propagating seismic waves or lowers their amplitude by distributing the energy due to randomly distributed heterogeneities, especially for local earthquakes with high-frequency content. Energy loss by these elastic processes is called scattering attenuation and is represented by the quality factor Q_s^{-1}. Coda waves which comprise the tail portion of local seismograms are the result of scattering process and have a smooth decaying envelope with increasing lapse time from the origin time of the earthquake [38].

The type and the strength of the scattering is usually characterized by the autocorrelation function of the random medium which involves the size of the scatterers and the wavelength of seismic waves. There are three types of ACF namely, Van Karman, Gaussian, and exponential with different correlation lengths. The relative size of the hetereogeneities compared to seismic wavelenghts determine the type of ACF (Figure 1.3). If the wavelength of the seismic wave is much bigger than the hetereogeneity than the medium is characterized by Gaussian ACF, whereas for hetereogeneities much bigger than the wavelength, then the medium has exponential ACF and scattering becomes isotropic [3].

1.3.2. Intrinsic Attenuation

Anelasticity or intrinsic attenuation is described as conversion of seismic energy to heat as the result of processes such as friction, thermal relaxation, and viscosity. Contrarily, the other effects that modify seismic waves such as geometrical spreading

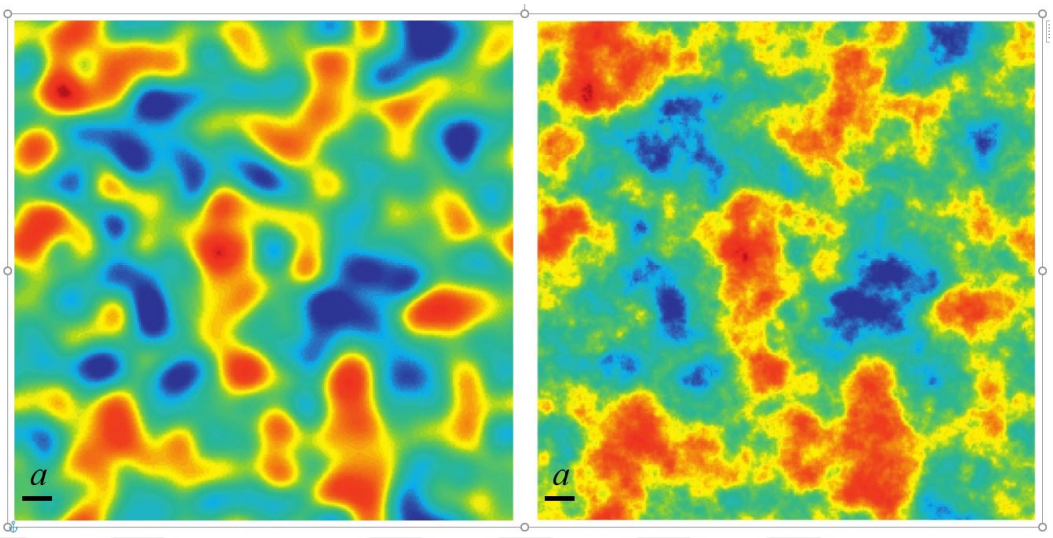

Figure 1.3. Two examples of random medium gaussian on the left and exponential on the right. a shows the correlation distance of the heterogeneities. Exponential media has more structure compared to Gaussian for the same correlation distance (From Treatise on Geophysics [3]).

and scattering are all elastic processes that conserve the seismic energy. Small-scale heterogeneities cause scattering of the seismic waves. On the other hand, intrinsic attenuation is usually more prominent for frequencies where wavelengths of the seismic wave are much longer than the heterogeneities in the medium [36]. Intrinsic attenuation which is represented by the quality factor Q_i^{-1} is predicted by numerous models of mechanisms based on microscopic cracks, pores filled with fluids, and physical properties of the elements in the rocks by many researchers. The variation of intrinsic attenuation in the medium depends on the temperature, pressure, fracture dimensions, and liquid inclusions.

1.3.3. Geometrical Spreading

One of the most obvious reasons for the decay of seismic energies with increasing distance is due to geometrical spreading effect. Geometrical spreading effect differs for surface and body waves. For spherical waves originated from a point source, energy in the unit volume decreases as the wave front expands proportionally to $1/r^2$

whereas amplitude decays by $1/r$ according to energy conservation. However, for an inhomogeneous medium, variation of amplitudes depends on the velocity structure of the medium [37]. We usually multiply energy densities by $4\pi r^2$ in order to remove the geometrical spreading effect in analysis.

1.3.4. Multipathing

The change in the seismic wave amplitude by lateral variations of the velocities in addition to vertical variations in the medium is characterized by multipathing. Multipathing is important in some cases as it can sway our interpretation of seismic data as small velocity variations can cause big differences in amplitude of teleseismic distances [37].

1.4. Coda Waves

Coda waves have several properties such as incoherency and lapse time dependence. Rautian and Khalturin [39] showed that the decay rate of the coda envelope is independent of the epicentral distance of the earthquake. Array analysis methods such as frequency – wavenumber power spectrum (F/K) analysis is used to determine the propagation direction and the apparent velocity of the coherent signal of interest that crossing the array. F/K shows the direction of the signal and the apparent velocity as a peak on the contour plot of slowness plane. However, if the signal of interest is not coherent over the array elements there will be no single definite peak showing the back-azimuth as is the case for coda waves.

An example of F/K analysis of direct and coda waves can be seen in Figure 1.4. The analysis of vertical seismograms recorded on an eight-element array located in New Mexico, USA was conducted for direct P, S and S-coda portions of the seismograms. The data are bandpass filtered in narrow bands according to phases of the interest (2-5 Hz for P, and 1.3-3 Hz for S and S-coda). The F/K analysis of waveform data in Figure 1.4b and 1.4c indicate that for direct waves contour plot shows clear singular peaks in the SSE region of the plots indicating the direction of the event. On the other hand,

S-coda shows no obvious direction of arrival as can be seen in Figure 1.4d. Therefore, these results indicate that the high-frequency coda waves are highly incoherent and propagate omni-directionally in the medium [4].

Nowadays, coda waves do not only represent the tail portion of the seismograms but also used for the wave trains that follow the direct arrivals of P and S-waves as P-coda and S-coda respectively.

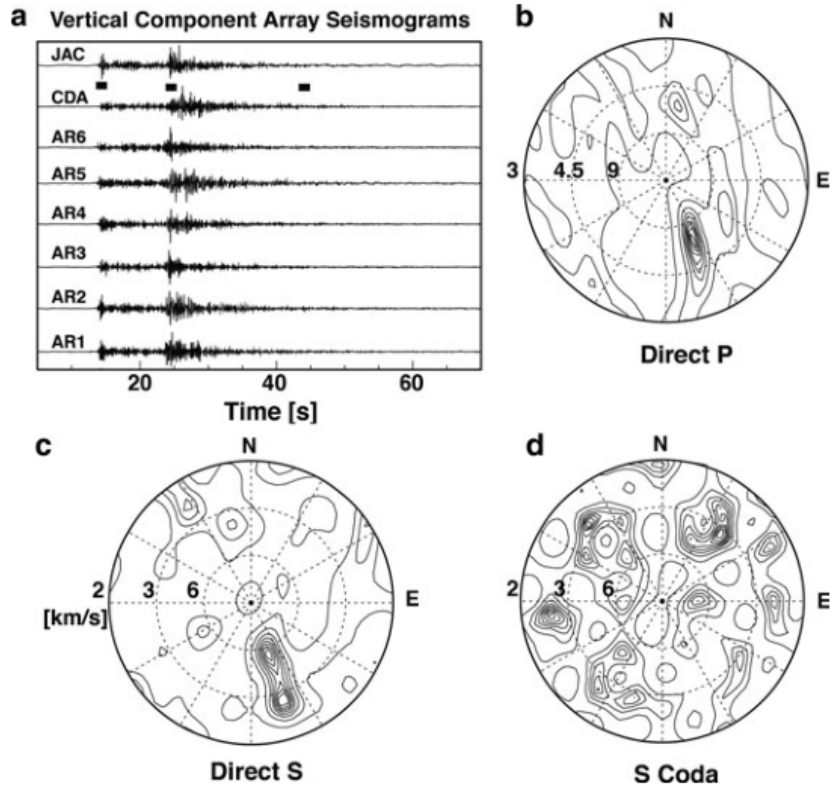

Figure 1.4. Array analysis of coda waves. a) a local earthquake recorded by an eight-element array located in New Mexico, USA. b) F/K analysis of the direct P-arrival. c) F/K analysis of the direct S-arrival. d) F/K analysis of S-coda after 20-seconds from the direct S-arrival. The numbers on the inside circles denote the apparent velocity values of the seismic waves crossing the array (From Sato et al., [4]).

One of the most common and effective methods of attenuation determination is coda Q (Q_c^{-1}) which utilizes the decay rate of the coda amplitude envelope within different lapse time windows to characterize the attenuation structure of the medium

assuming single scattering mechanism. Many researches used the method for various regions around the globe. Although coda Q consist of both types of attenuation, according to Aki [40] and several other authors, Q_c^{-1} represents the intrinsic absorption rather than the scattering loss in the propagating medium. In addition, numerical [41] and laboratory experiments [42] suggests that the coda Q_c^{-1} should only include intrinsic attenuation. According to Akinci and Eyidoğan [13] observational results do not agree with the numerical simulations and laboratory experiments and the coda Q_c^{-1} varies between intrinsic Q_i^{-1} and total attenuation Q_t^{-1}. There are several models for the estimation of attenuation quality factor from coda waves such as single scattering, single backscattering, single isotropic scattering and multiple scattering.

1.4.1. Single backscattering

The single backscattering model assumes that the source and the receiver locations are common, therefore the scattered waves arrives the station from the opposite direction of the first propagation direction. Single backscattering model which was introduced by Aki and Chouet [43] incorporate both body and surface wave scattering and Coda waves have been suggested to be a combination of waves that are scattered backwards from a plurality of scattered scatterers (Aki, 1969). The model that creates the coda waves formed by the constructive or disturbing interference of the waves showing the scattering as a result of the lateral and vertical different heterogeneities in the place is called the single scattering model. In this model, it is recommended that the media has a poor scattering feature. Thus, the wave shows scattering due to a single scattering and this scattering wave is a weak energy wave, so it does not have any other scattering.

1.4.2. Single isotropic scattering

In this model scattering is assumed to be isotropic and the energy of the elastic waves radiate spherically from the source. Single isotropic model which was developed on top of single backscattering model by Sato [44] is especially used for the epicentral distances bigger than 100 km. In single isotropic scattering model energy does not turn

into heat for non-dispersive elastic medium, hence the amplitude of the waves decreases as a results of geometrical spreading without any shape deformation [44]. Scattering coefficient g is described by Sato [44] as the scattering power per unit volume. By averaging g in all directions, we obtain the total scattering coefficient g_0 which can be expressed as $g_0 = l^{-1} = Q_s^{-1}k$ where l is the mean free path and k denotes the seismic wavenumber.

1.4.3. Multiple scattering

Multiple scattering model were developed as a result of the need to model higher order multiple scatterers randomly and homogeneously distributed in a medium for increasing lapse times. Energy is again radiates spherically from the source. Multiple scattering becomes dominant for longer lapse times, thus the direct energy is assumed to be weak compared to multiply scattered energy density. This model is especially useful to separate the intrinsic and scattering attenuation in a region of interest.

Solutions to the multiple scattering of the wave energy first began with Wu [45] as he separated the scattering and intrinsic attenuation based on the Radiative Transfer Theory assuming isotropic scattering and no spatial heterogeneity. Following Wu, an analytical solution of the energy transfer formulas was provided by Zeng et al. [46] describing the single and multiple scattering of energy with uniform earth model. Hoshiba [47] approached the problem with Monte Carlo simulations of multiple scattered coda wave energy based on the energy conservation law. He emphasized the importance of the selection of different lapse time windows and named his method as the Multiple Lapse Time Windows (MLTW) method. Coincidently, Fehler et al. [5] in his study adopted Zeng's method to find the relative contributions of scattering and intrinsic absorption by integrating the energy densities over three consecutive time windows and also called it the Multiple Lapse Time Window Method.

In summary, multiple scattering of coda wave energy has been researched by either numerical simulations (e.g [5–7, 9, 47]) or using analytical solutions of Zeng (e.g [8, 10, 11]). However, for non-uniform earth models such as depth dependent there

is no analytical solution and therefore numerical simulations are required according to Hoshiba et al. [14]. One of the most common methods to simulate synthetic seismograms according to multiple scattering model is Monte Carlo simulation method. In this method, random propagation of millions of particles that are scattered in a 2D isotropic medium is simulated by the computer. Figure 1.5 displays an example of the Monte Carlo simulation process. Dots are coloured according to number of times the particle was scattered as the time increases in a isotropic medium. Particles are spread in all directions from the source with constant scattering probability defined by l the mean free path length [3].

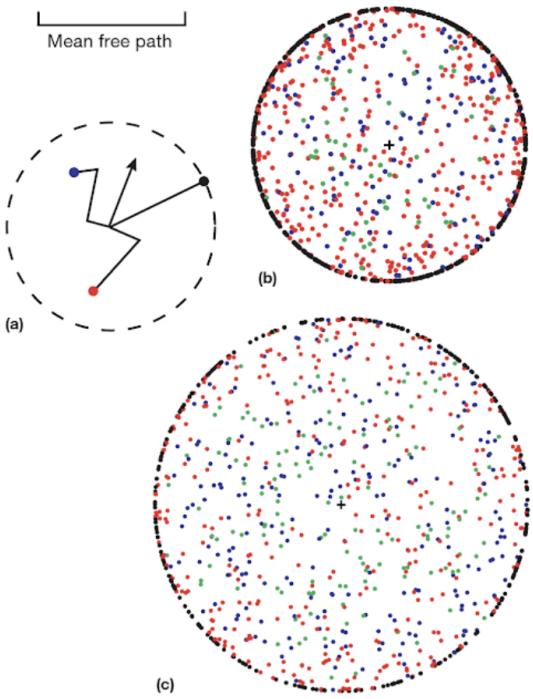

Figure 1.5. Example of Monte Carlo Simulation. a) Black dots are not yet scattered, red dots show the particles scattered once, and blue dots denote particles scattered twice. b) Results for 1000 particles after time $t = 0.8/v$, where v is velocity. c) Results for 1000 particles after $t = 0.8/v$ (From Treatise on Geophysics [3]).

2. DATA AND METHOD

2.1. Data Collection and Preparation

The seismic data in this study were acquired from two different seismic networks operated by Boğaziçi University, Kandilli Observatory. The first set of data were obtained from the array stations in the Central Anatolia, which are labeled as the Belbaşı array. The Belbaşı array is composed of two sub-arrays, Ankara and Keskin. The medium-period array with a 40 km radius located in Ankara and the short-period array with 3 km radius located in Keskin. Each array has a broadband element located in the middle of the circular geometry. Short period instruments (Geotech 23900) are installed at depth 30 metres from the surface while medium and broadband instruments (Geotech KS54000) are installed at a depth of 60 m from the surface. The short period instruments are vertical velocity type borehole sensors and they record data at a rate of 20 samples per second with a 24-bit resolution. The seismograms recorded with array stations have very high quality and signal to noise ratio (SNR) due to very low noise levels at the stations. This is one of the advantages of borehole instruments. Furthermore, the array has its advantages over single stations with the signal processing capabilities such as beamforming to further increase the signal to noise ratio for a much better phase identification. In addition to array stations, some of the Boğaziçi University Regional Earthquake-Tsunami Monitoring Center's (RETMC) permanent seismic stations that are in Central Anatolia were used in the study. These stations include Guralp surface type 3-component broadband sensors (3T, 3ESP, 6T) and Guralp digitizers (DM24, CD24).

In this study, with two BB stations from the Belbaşı and Keskin arrays, a total of 16 seismic stations listed in Table 2.1 were used to acquire quality seismic data. Medium period and short period array station data were not used since their sampling rates (4 sps and 20 sps) are not suitable for high-frequency attenuation study. The TUBITAK temporary network (DEPAR) that had been installed in the vicinity of Bala, also recorded many aftershocks [1], however, the instruments were mostly consist

of geophones and therefore, their data was also not suitable for this study due to the high damping of the geophones.

177 earthquakes were selected between the years 2008 and 2011 for this study. The magnitude range of the selected events varies between 2.5 and 4.7. The events recorded with both networks were selected depending on the quality of the data, such as unclipped waveforms with high SNR, and on the criteria for hypocentral parameters required by the data processing methods. All the events occurred in focal depths less than 20 km with an average depth of 6 km. The hypocentral distances of the events range between 15 and 150 km. The key factor for selection of data is high SNR value since I am looking to work with S waves and the coda part of the waveforms. Noisy data were discarded and only the waveforms with SNR > 3 were selected.

The locations of the stations and the chosen events are shown in Figure 2.1 on a map drawn by the excellent Generic Mapping Tools (GMT) software of Wessel et al. [48]. The circles represent the selected events while the inverted black triangles denote the seismic stations used in the study. The colour bar shows the depth of the events. A list of the events used in the study and their hypocentral parameters is given in Appendix A in Table A.1.

Due to the difference in the waveform data formats between the array and the other stations, waveforms were converted to SAC (Seismic Analysis Code) format in order to process all the data together. GEOTOOL software provided by the PTS (Provisional Technical Secretariat - CTBTO) was used to cut continuous array data into 3 minutes of event data and then convert from CSS3.0 (Center for Seismic Studies) to SAC format. The waveform data from RETMC stations were already in SAC format and did not need to be converted. All the waveforms were instrument corrected using the pole-zero responses in SAC format by built-in SAC “Transfer” command and phase picked.

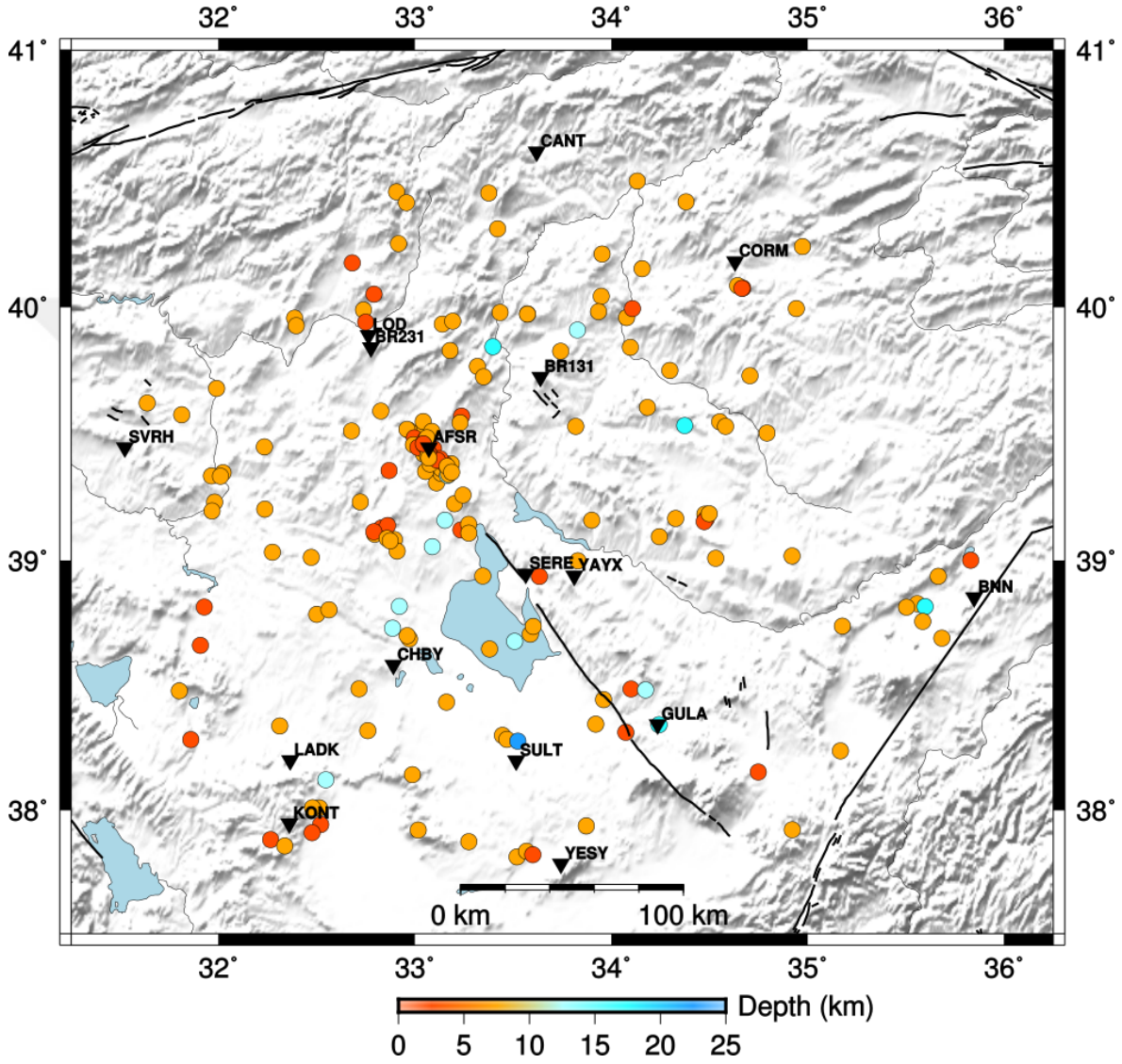

Figure 2.1. The location map shows the study area and the selected earthquakes as circles while presenting the seismic stations as inverse triangles. Colors vary depending on the depth of the event. Small map shows the study region in respect to Turkey.

Table 2.1. List of seismic stations used in the study.

STATION	LAT	LON	SENSOR	DIGITIZER
BR131	39.7250	33.6390	KS54000	AIM24
BR231	39.8417	32.7759	KS54000	AIM24
AFSR	39.4468	33.0707	3ESP	DM24
BNN	38.8522	35.8472	3T	DM24
CANT	40.6062	33.6197	3T	DM24
CHBY	38.5823	32.8902	6T	CD24
CORM	40.1785	34.6302	3ESP	DM24
GULA	38.3444	34.2360	6T	CD24
KONT	37.9453	32.3605	3T	DM24
LADK	38.2000	32.3648	3T	DM24
LOD	39.8893	32.7640	3T	DM24
SERE	38.9463	33.5640	6T	CD24
SULT	38.1988	33.5157	3T	DM24
SVRH	39.4470	31.5230	3T	DM24
YAYX	38.9387	33.8115	6T	CD24
YESY	37.7825	33.7432	6T	CD24

2.2. Method

In this dissertation, I have applied the multiple lapse time window (MLTW) analysis to determine the level of contribution of scattering and intrinsic absorption to total attenuation in the Central Anatolia region. Spatial and temporal variation of the multiple scattered seismic wave energy is modeled by Hoshiba [47] using the following assumptions:

- Scattering is isotropic;
- Scattered waves are considered as incoherent waves;
- Spherically radiated S waves;
- Constant S wave velocity;
- No intrinsic absorption of the energy in the medium.

Monte Carlo simulation method of Hoshiba [49] was used to simulate the energy density of the multiple scattered coda waves using many particles that have unit energies at the event source. Determined by Snell's Law, the effects of reflection/transmission, scattering, intrinsic absorption and geometrical spreading all contribute to the calculation of the simulated energy densities [14]. The details of the computer simulation are given in the paper by Hoshiba [49]. This method allows us to estimate the extinction length L_e^{-1} and Seismic Albedo B_0, which are described as the decay of direct S-wave energy by e^{-1} and the ratio of scattering to total attenuation, respectively.

Coda waves have been studied extensively by many researchers for attenuation determination due to easy applicability. Coda $Q(Q_c^{-1})$ represents both intrinsic and scattering attenuation in a region while assuming single scattering in the medium. Coda Q involves calculating the envelope of the coda portion of seismograms and measuring the decay rate to obtain the frequency-dependent attenuation in a region. Several authors concluded that the Q_c^{-1} attenuation mostly consists of intrinsic absorption rather than scattering attenuation [40–42, 47, 50].

Multiple scattering models have been adopted following the single scattering stud-

ies. In this model, direct S wave and coda wave amplitudes both decrease with the propagation distance with intrinsic absorption, on the other hand, scattering reduces the direct wave amplitude while amplifying the coda amplitude [14]. Separation of scattering and intrinsic attenuation using multiple scattering investigated by Wu [45] using the Radiative Transfer Theory with an assumption that has no spatial heterogeneity in the medium. Zeng et al. [46] and Sato [51] solved the multiple scattering model analytically. Hoshiba [47] synthesized the energy density of the multiple scattered coda waves using a Monte Carlo simulation method based on energy conservation law and obtained comparable results with the analytical solutions. According to his study the selection length of lapse time is crucial and vital for the correct representation of the attenuation structure. He used three-time windows to model the multiple scattered seismic wave energy and therefore called his method the Multiple Lapse Time Window (MLTW) method. The common ground of these studies is the assumptions such as uniformity in velocity structure of the medium and the Quality factors for scattering (Q_s^{-1}) and intrinsic (Q_i^{-1}) attenuations.

All the waveforms were bandpass filtered in five frequency bands with center frequencies 1.5, 3, 6, 8, and 9 Hz with bandwidths of ± 0.5, ± 1, ± 2, ± 3, ± 3 respectively. Mean square amplitudes of the waveforms were calculated following the filtering process to obtain the signal envelopes. The Envelopes for three-components were summed up in order to reduce fluctuations [52]. In Figure 2.2, these processing steps are clearly presented. The BR131 station, one of the elements of the short period array, was used as an example in this case. Raw, filtered waveforms and the signal envelopes are shown from top to bottom of the figure.

The last row in the figure shows the time-windows (t_1, t_2, t_3) that are used in the MLTW analysis to obtain the S and coda wave energy integrals. Let us call the mean-squared amplitude envelopes as $A_{obs}(r_m, t)$, where t is the time measured from origin time and rm represents hypocentral distance for each seismogram. The mean-squared envelopes were integrated in three consecutive time-windows 0-15, 15-30, and 30-45s

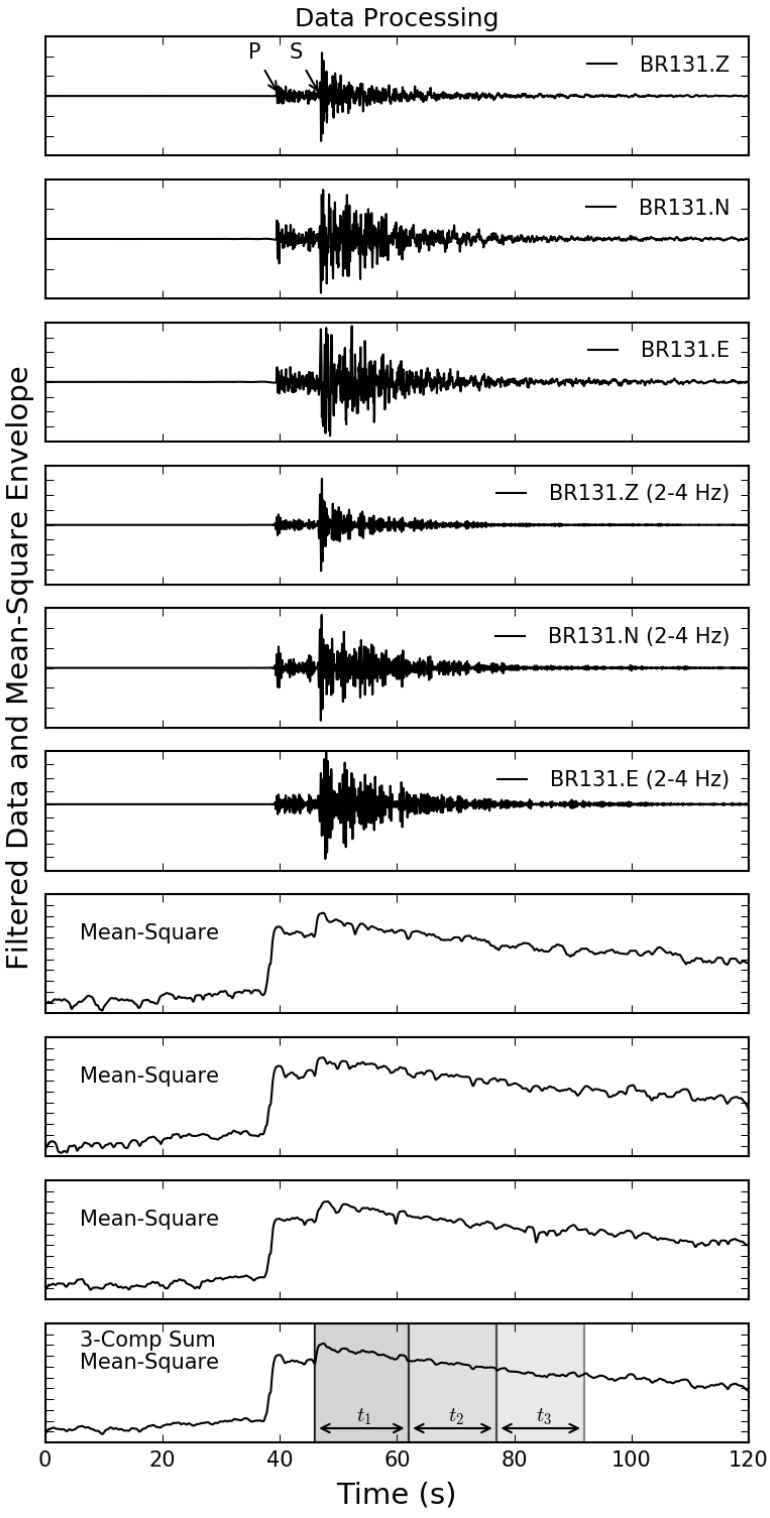

Figure 2.2. Data processing steps for the MLTW analysis. Top three rows show the raw broadband data, the middle rows show the filtered waveforms while the bottom rows present the mean-squared signal envelopes and their summation in the final row.

starting from the S-arrival time,

$$\begin{aligned} e_1(r_m, f) &= \int_{t_s}^{t_s+15s} A_{obs}(r_m, t)dt \\ e_2(r_m, f) &= \int_{t_s+15s}^{t_s+30s} A_{obs}(r_m, t)dt \\ e_3(r_m, f) &= \int_{t_s+30s}^{t_s+45s} A_{obs}(r_m, t)dt \end{aligned} \tag{2.1}$$

$e_n(r_m, f)$ (n=1,2,3) stands for the integrated observed mean squared amplitudes for three consecutive time-windows where r_m is the distance and f, is the frequency, and t_s denotes the arrival time of the S phase. Three factors affect the wave amplitude; source power, local site effects, and wave propagation effect. The coda normalization method [53] was used in order to remove the source and site effects before applying the Multiple Lapse Time Window method. A fixed reference time, t_{ref} was chosen based on the condition, $t_{ref} \geq 2r_m/v$ so that the direct S wave energy does not interfere with the coda energy. In this study, t_{ref} was chosen as 65 seconds from the origin time for all the hypocentral distances. Implementing the coda normalization technique involves normalizing the integrated mean-squared amplitudes with the coda energy at the reference time t_{ref}. Hence, the normalized energy is represented by the following formula;

$$E_n(r_m, f) = \frac{e_n(r_m, f)}{A_{obs}(r_m, t_{ref})} \quad n = (1, 2, 3) \tag{2.2}$$

where, $A_{obs}(r_m, t_{ref})$ is the coda wave energy at the reference time t_{ref} and $E_n(r_m, f)$ indicate normalized energies for the nth time-window. According to Hoshiba [49, 54] coda normalization method is not suitable for data with separated focal depths, however, in our case, all events in the dataset are shallow crustal earthquakes which are suitable for the coda normalization method.

Finally, the processing of the observed event data ends by correcting the energy densities for the geometrical spreading effect. The energy densities were multiplied by $4\pi r^2$, where r is the hypocentral distance.

The next step in the multiple lapse time window analysis is to generate synthetic energy density curves to compare with the observed data. A FORTRAN program for numerical simulations of Monte Carlo method of Hoshiba [49] was used in order to generate the synthetic curves. Defining $A_{syn}(r,t)$ as the synthetic energy densities computed by the software, then I apply the previous procedures (as in equation 2.2) to the synthetic data to calculate the integrated energy densities namely $E_{n\ syn}(r)$ as;

$$\begin{aligned} E_{1\ syn}(r,f) &= \int_{t_s}^{t_s+15s} A_{syn}(r,t)dt/A_{syn}(r,t_{ref}) \\ E_{2\ syn}(r,f) &= \int_{t_s+15s}^{t_s+30s} A_{syn}(r,t)dt/A_{syn}(r,t_{ref}) \\ E_{3\ syn}(r,f) &= \int_{t_s+30s}^{t_s+45s} A_{syn}(r,t)dt/A_{syn}(r,t_{ref}) \end{aligned} \tag{2.3}$$

Here, the synthetic energies are again normalized by the energies at time, t_{ref} indicated by the $A_{syn}(r,t_{ref})$ term in equation 2.3. An example of the synthetic energy envelopes and its energy density curves is shown in Figure 2.3. The different colours on the left figure vary with hypocentral distances, whereas integration of envelopes within three time-windows is represented by three curves on the right figure. Finally, I compare the observed $E_{n\ obs}(r_m,f)$ and synthetic $E_{n\ syn}(r,f)$ energy integrals to obtain the L_e^{-1}, B_0, and consequently, scattering Q_s^{-1} and the intrinsic Q_i^{-1} attenuation values.

The comparison between the observed and the synthesized energy curves was made using the grid search method, in order to find the best pair of L_e^{-1}, B_0 that give the smallest residual value as a result of the least squares method. 2668 pairs of L_e^{-1}, B_0 values were searched to find the best fit to the observed data. L_e^{-1} values range between 0.003 to 0.06 km^{-1}, and B_0 extends from 0.10 to 1.0. Therefore, the simulation code to generate the synthetic curves was run 2668 times for each frequency of interest and compared to observed curves using the least squares method. I have written an Obspy Python script to perform the grid search and plotted resulting figures using the Matplotlib library [55, 56].

As a side note, the run-time of the fitting process with a model configuration of

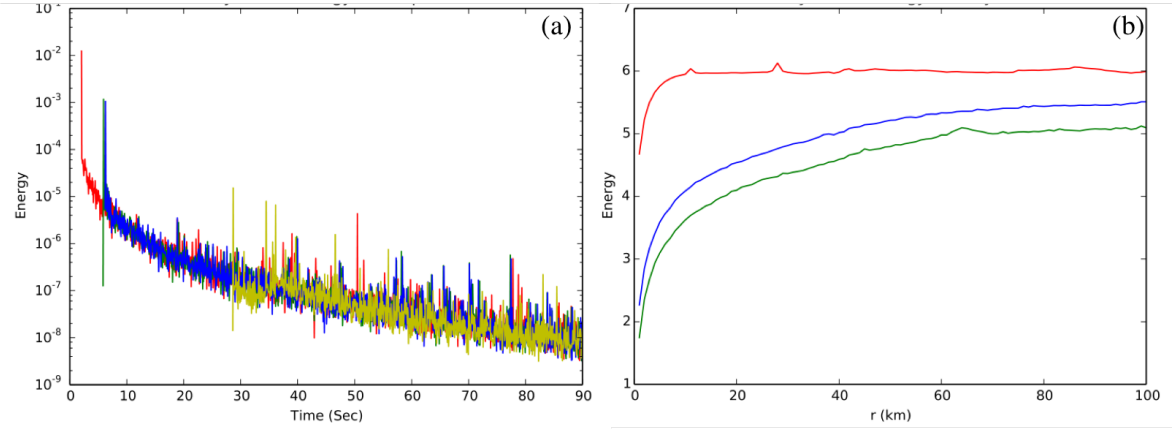

Figure 2.3. Synthetic energy envelopes (a) generated by Hoshiba's code and the energy density curves (b) calculated by integrating the envelopes on the left are shown.

two layers and 1000000 particles takes around five days to complete for a single centre frequency on a workstation with a i5 CPU. The best pair which give the least residual was chosen based on the following formula;

$$\begin{aligned} &Residual(L_e^{-1}, B_0) \\ &= \frac{1}{M}\sum_{n=1}^{3}\sum_{m=1}^{M}[\log(4\pi r^2 E_{n\ obs}(r_m)) - \log(4\pi r^2 E_{n\ syn}(r))]^2 \\ &(n = 1, 2, and\ 3) \end{aligned} \tag{2.4}$$

where M is the number of seismograms used in the process. To determine the errors in pairs of L_e^{-1}, B_0, values 10% larger than the minimum residual were chosen to be the limits of the errors. Final attenuation quality factors for total, intrinsic and scattering are determined from the best B_0 and L_e^{-1} values simply by calculating the following equation 2.5,

$$Q_t^{-1} = \frac{L_e^{-1}}{v}, \quad Q_s^{-1} = \frac{B_0 L_e^{-1} v}{w}, \quad Q_i^{-1} = \frac{(1 - B_0) L_e^{-1} v}{w} \tag{2.5}$$

where Q_t^{-1},Q_s^{-1},and Q_i^{-1} symbolize total, scattering, and intrinsic absorption respectively. w is angular frequency and v denotes shear-wave velocity.

3. SINGLE STATION MULTIPLE LAPSE TIME WINDOW ANALYSIS

Here I present the results of the analysis starting with the comparison of the observed data and the synthetic energy density curves and followed by residual values for each site. The results are expressed for each station individually in order to show the spatial variety of the attenuation structure in the region. This model assumes an average shear wave velocity of 3.2 km/s for crust, 2.8 g/cm3 density, and an average of 6 km focal depth for the earthquakes as illustrated in Table 3.1. The lapse time is selected as 65 seconds according to the data. Average Shear-wave velocity is calculated for each station as a ratio of hypocentral distance versus arrival times of the events recorded at that station and then averaged. Since there were no significant variation in seismic velocities between regions around each station, an overall velocity of 3.2 km/s has been chosen for the simulation.

Table 3.1. Model parameters for Hoshiba's synthetic simulation code.

Depth (km)	V_s **(km/s)**	g **(1/km)**	h **(1/km)**
6	3.2	0.01	0.0049

g parameter is the scattering power per unit volume (scattering coefficient), and h represents the intrinsic absorption strength. Depth is the average source depth of the events.

Geometrical spreading corrected energy densities are integrated over three-time windows (0-15s, 15-30s, and 30-45s) and plotted versus hypocentral distance then, compared to the synthetic curves simulated by Monte Carlo simulations of many particles. The least square method was employed to find the best match of the curves with the observed data. 0-15s time-window from the direct S-arrival is proportional to total attenuation in the medium, the second and especially third time-windows represents the amount of scattering attenuation since the late arriving energy is composed of S-coda

waves. Residual maps of the fitting process (least squares) are plotted to determine the error margins for the best L_e^{-1} and B_0 pair. The residual values of each iteration were normalized by the minimum residual and plotted so that the best solution is represented by value of 1.0 and star symbol on the residual map figures in the next section. 90% of confidence is chosen for the level of uncertainty.

3.1. Comparison of Observed and Best-Fitting Energy Distance Curves

Afşar (AFSR) station located within approximately 15 km SW of Bala earthquakes recorded many aftershocks after the Bala events. The result of the analysis and the residuals are shown in Figure 3.1 and Figure 3.2. The fitting process shows good correlation with synthesized curves for all frequency ranges. Observations have good coverage in terms of hypocentral distance distribution as good quantity of earthquakes recorded by this station are in the distance range of 5 to 145 km. The first time-window of 0-15s shows more scatter of values compared to other time-windows. The reason for that could be related to non-spherical radiation pattern since the first time-window only includes direct S-wave energy which show large amplitude variation even after the normalization process [5]. However, Hoshiba et al. [14] argued that the scatter of energy in the first time-window was not originated by the effect of radiation pattern according to his corrections.

Energy-distance curves of the station Bünyan – Kayseri (BNN) suffers from the low number of earthquakes records in the vicinity and partly from the selection criteria of SNR > 3. I had to omit many earthquakes with low SNR values as it is important for this study to have clear direct S-waves and S-coda. Observed and synthetic data shows good fitting for all frequencies for the third-time window (E3) but have a lower degree of fit for first and second time-integrals (E1 and E2) for near hypocentral distances around 20 km (Figure 3.3). Residual maps in Figure 3.4 show that B_0 values decrease with increasing frequency from 0.5 to 0.28 according to the best pairs. This behaviour reflects the fact that the intrinsic attenuation is more effective for frequencies higher than 1.5 Hz in terms of the region around BNN station.

Figure 3.5 indicates that the synthetic curves matches very well with the observed data recorded by BR131 station in Keskin. For all the frequency ranges, the best pair of B_0 and L_e^{-1} matches very well the first and third energy curves (E1, and E3) in all hypocentral distances, yet does not show the same performance for the second time-window. The advantages of the borehole type seismometer are obvious in this case with a high number of good quality observations recorded by this station. There seems to be no gap in the hypocenter distribution. B_0 values vary between 0.34 and 0.3 (Figure 3.6) indicating that the intrinsic absorption is the dominant attenuation mechanism.

Results of the BR231 (Ankara) station, which is the other borehole array station in the study shows good fit of observed and synthetic data for all frequencies in Figure 3.7. The number of observations is sparser for distances higher than 100 km and the majority of the observed events are clustered mostly on the local distances. Nevertheless, model parameters are in accordance with the integrated observations for each time window. The negative slope of the curves is increases proportionally with frequency as the scattering effects becomes weaker against the intrinsic attenuation. This phenomenon is also confirmed by the B_0 values obtained from the minimum residuals at each frequency in Figure 3.8. At 1.5 Hz, seismic albedo B_0 is estimated as 0.46, whereas its value decreases steadily to 0.34 at 9 Hz.

Looking at the observations of Çankırı seismic station (CANT) located in northern part of the Central Anatolia, the observations cover the hypocentral distances from 20 km to 140 km with accumulation on the distant parts in Figure 3.9. Three Synthetic curves from the model parameters are in good agreement with the observed data again for all the centre frequencies. There are some spikes in the curves, especially at 1.5 Hz and 8 Hz frequencies and the reason for those is probably the low number of observations and the number of particles used in the Monte Carlo simulation. There is a trade-off between the accuracy and the computing time of the simulation. More particles in the simulation mean better accuracy albeit longer execution time. Figure 3.10 depicts the residuals for the best pair of L_e^{-1}, B_0. Lower frequencies have higher seismic albedo B_0 starting with 0.5 for 1.5 Hz and decreases to 0.28 as the frequencies increase. CANT displays attenuation characteristic very similar to BNN station

although the greater distance between these two stations.

The data from the station CHBY in Cihanbeyli exhibits small changes in attenuation structure in terms of frequency compared to previous stations. Observations comprise of hypocentral distances between 40 to 140 km in a good distribution except the gap after the 110 km. Although, energy densities seem to be dispersed, overall fit to the data is in acceptable levels for all frequencies (Figure 3.11). Once more, a couple of spikes in synthetic curves exist at 8 Hz and 9 Hz frequencies around 60 km due to simulation parameters. Residual maps in Figure 3.12 reveal that the intrinsic attenuation is the main factor affecting the seismic wave amplitudes instead of scattering. As the downward trend of B_0 is an indication of high anelasticity in the medium.

Figure 3.13 belonging to the analysis results of CORM (Çorum) station located in the northeastern part of the study area exhibit similar behavior to CANT station. Both of those stations are closer to each other in spatially and in terms attenuation structure according to the related figures. Comparing the observed and simulated curves, hypocentral distance distribution of the events are adequate and the energy densities are fitted very well by the model at all frequencies. In addition, the integrated energy densities do not show much scatter. Attenuation structure defined by the best pair of parameters is shown in Figure 3.14. At a frequency of 1.5 Hz, the medium is characterized by almost equal scattering and intrinsic attenuation as the seismic albedo B_0 is estimated as 0.5. Like the other stations, as the frequency increases, intrinsic absorption takes over. The values of B_0 dips from 0.5 at 1.5 Hz to 0.28 at 9 Hz frequency.

GULA (Gülağaç) station near the city of Aksaray is the closest station to the Cappadocia volcanic province. Energy-distance curves belonging to this station are shown in Figure 3.15 followed by the respective residual maps in Figure 3.16. Most of the events by these stations are observed by between 60 – 120 km hypocentral distances. There are observational gaps due to low number of good quality (high SNR) events around the station. Observed and synthetic energy densities demonstrate good matches in all frequency ranges for three time-window integrals (E1, E2, E3).

Spikes are observed for E1 synthetic curve at 80 km and 100 km due to simulation parameters. Best fitting pair of values for each frequency range also indicates that the intrinsic attenuation is prominent for this area in line with the low seismic albedo $<$ 0.5.

KONT station located in the vicinity of Konya shows a lot of scatter in the first energy-distance curve (E1) as can be seen in Figure 3.17. The model fits the observations well in E2 and E3 curves; however, there is a lack of events between 20 km and 60 km hypocentral distances. All in all, simulated curves have a good fit to the observed data in all frequencies for distances higher than 60 km. The slope of the energy density curves increases with frequency, hence, high intrinsic attenuation. Residual maps shown in Figure 3.18 also confirms these findings with a yield of seismic albedo B_0 values 0.4 to 0.28 for the frequency range.

Figure 3.19 reveals the results of the comparison between observed and synthetic data for the station LADK (Ladik). At the first glance, it seems that the events are spread out more or less with regular intervals for the hypocentral distance range. The model does good work for the third curve (E3), but somehow underestimates the second time-window curve (E2). The scatter of points in E1 is again present due to non-spherical radiation of the earthquakes. Residual maps for LADK station are shown in Figure 3.20. B_0 values obtained from the residuals indicate very strong intrinsic attenuation in the medium with the values changing between 0.36 to 0.16 for each frequency.

LOD (Lodumlu) station is expected to display similar results to BR231 station since both of them are close to each other. The results presented in Figure 3.21 indicates that the model does not fit the observations well especially for E2 (green curve) for frequencies higher than 3 Hz because of dispersed data. E1 and E3 curves fits the data much better for all frequencies. In addition, I observe that the curves are not bending downwards with increasing frequency. Seismic albedo values measured by the best fitting process are shown for each frequency in Residual Maps (Figure 3.22). All of the B_0 values are found to be lower than 0.5, meaning that intrinsic attenuation is

the major factor affecting the seismic wave amplitudes.

SERE (Şereflikoçhisar) station is located in the southern part of the Tuz Gölü Fault. The results of the analysis displayed in Figure 3.23 indicates that the simulations fit the data well over the range of hypocentral distance and all frequencies. On the other hand, the quantity of data is low compared to northern stations due to low seismicity. Looking at the residual maps in Figure 3.24, scattering attenuation is higher than the intrinsic absorption for frequencies 1.5 Hz and 3 Hz, evident from estimated seismic albedo values of 0.56 and 0.52, respectively. Intrinsic attenuation becomes more prominent when the frequency rises as the seismic albedo diminishes to 0.34 at 8Hz, and then rises to 0.38 at 9 Hz. Close proximity to the fault line might be the reason of predominant scattering attenuation for low frequencies.

The next station in the processing is the SULT (Sultanhanı) station located in the south of Tuz Gölü. Least squares fitting results of the simulated data are presented in Figure 3.25. Observations contain a good quantity of data and spread over the hypocentral range between 40-150 km. Synthetic curves fit the observations well for all frequencies. In addition, it can be seen that three curves are very near to each other for 1.5 Hz frequency and move apart with higher frequencies. This situation indicates rapid change in attenuation structure. If the three curves are close to each other, that could be interpreted as higher scattering attenuation in the medium since second and third curves are proportional to the scattering attenuation. Residual maps in Figure 3.26 also confirms the frequency dependent attenuation mechanism variation. Scattering is the dominant factor only for 1.5 Hz frequency with B_0 value of 0.62. However, higher frequencies are affected by the intrinsic attenuation as can be inferred from the best fit parameters (B_0=0.46, 0.42, 0.36).

SVRH (Sivrihisar) covers the western part of the study area. Results of the MLTW analysis are shown in Figure 3.27 and the residual maps are presented in Figure 3.28. I observe that the integrated energy densities for the first time-window (E1 – red dots) exhibit a lot of scatter and the observations between 20-60 km range have especially abnormal behavior as their amplitudes are much lower than the rest of them,

consistently for all frequencies. Moreover, the second best fit curve (E2) also displays similar behavior for data closer than the 100 km range. The majority of the events are accumulated at distance range of 110-150 km. Therefore, the best fit curves are determined according to this distance range by the least squares fit. Obtained values of L_e^{-1} and B_0 indicates that the intrinsic attenuation is higher in this area. However, these results might not be reliable due to anomalies in the observed data.

Results obtained for station YAYX (Yaylak) from the analysis of MLTW method are shown in Figure 3.29. Observed and synthesized energy densities match well for all frequency and distance ranges except a small mismatch for the second curve (E2). Hypocenters cover a distance of 5 km to 150 km albeit with low quantity of earthquakes. The slope of the curves increases proportionally with frequency indicating that the intrinsic attenuation is becoming more pronounced in the region. Residual maps that are shown in Figure 3.30 gives us the best L_e^{-1}, B_0 pairs that fit the model to the data. According to seismic albedo B_0 values, scattering attenuation is on par with intrinsic absorption for 1.5 Hz, but decreases rapidly and becomes weaker for higher frequency ranges.

MLTW analysis results from the station YESY are given in Figure 3.31. Due to lack of events in this area, the best fitting of model to the data could be unreliable. It was hard to find good quality records for this station. There are a few gaps in hypocentral distances, namely between 20-60 km, 80-110 km, and 110-140 km. The curves obtained from the best fit of current data shows big uncertainties as expected. Residual maps in Figure 3.32 have large dark red coloured areas meaning high uncertainty in the solutions. The uncertainties also increase with frequency as can be easily seen in the figure. The medium is characterized by scattering attenuation with B_0 value of 0.56 for 1.5 Hz and 0.5 for 3 Hz. As the frequency goes up the intrinsic attenuation becomes stronger but not by a large margin.

The following pages show the related figures of the MLTW analysis for each analyzed station. The exact values of L_e^{-1}, B_0 pairs and their uncertainties are given in the final attenuation tables in Section 3.2.

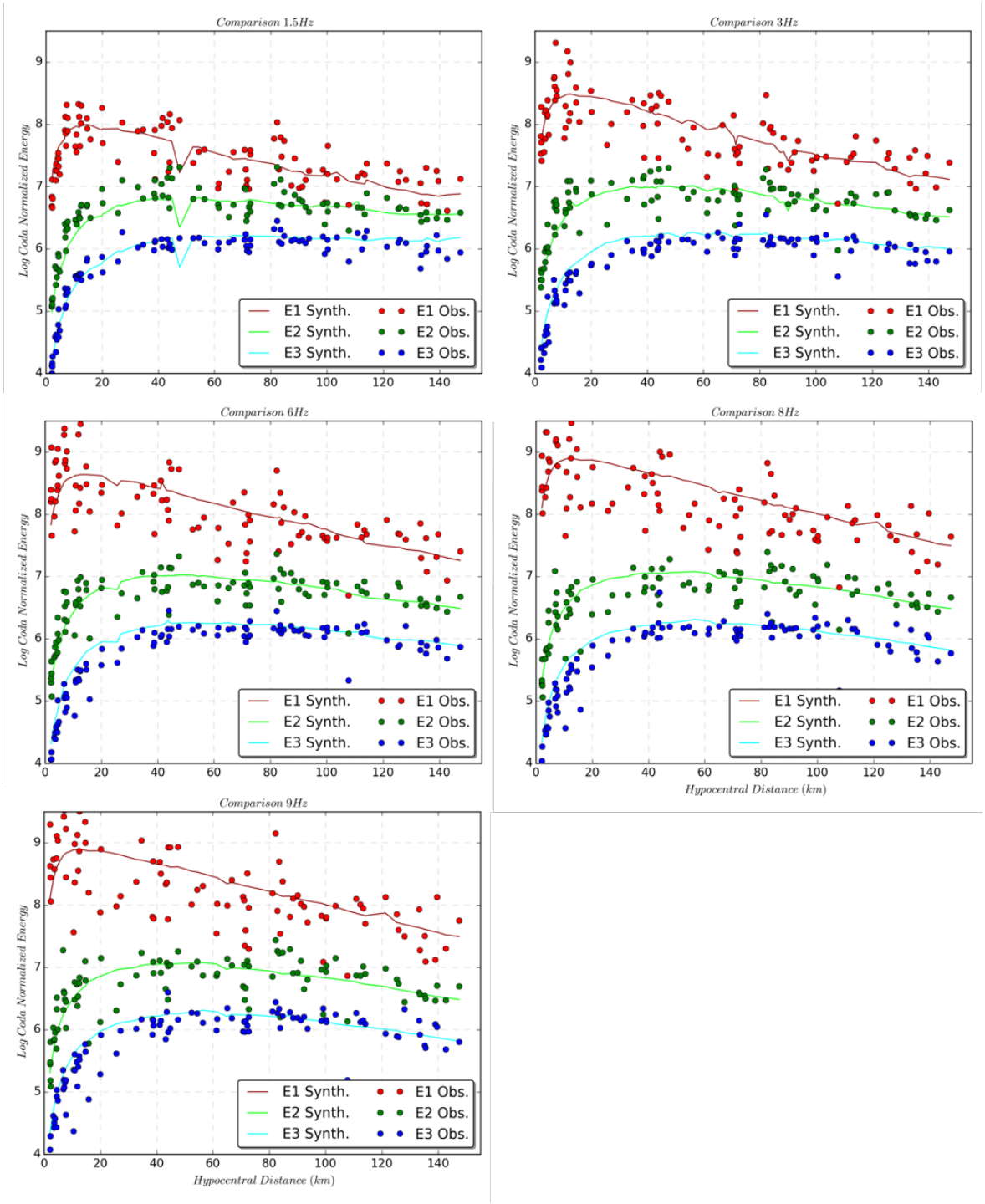

Figure 3.1. Comparison of observed energy density(circles) and the synthetic energy curves given by the best pair of L_e^{-1} and B_0 versus hypocentral distance for AFSR station. Colors represents each time-windows.

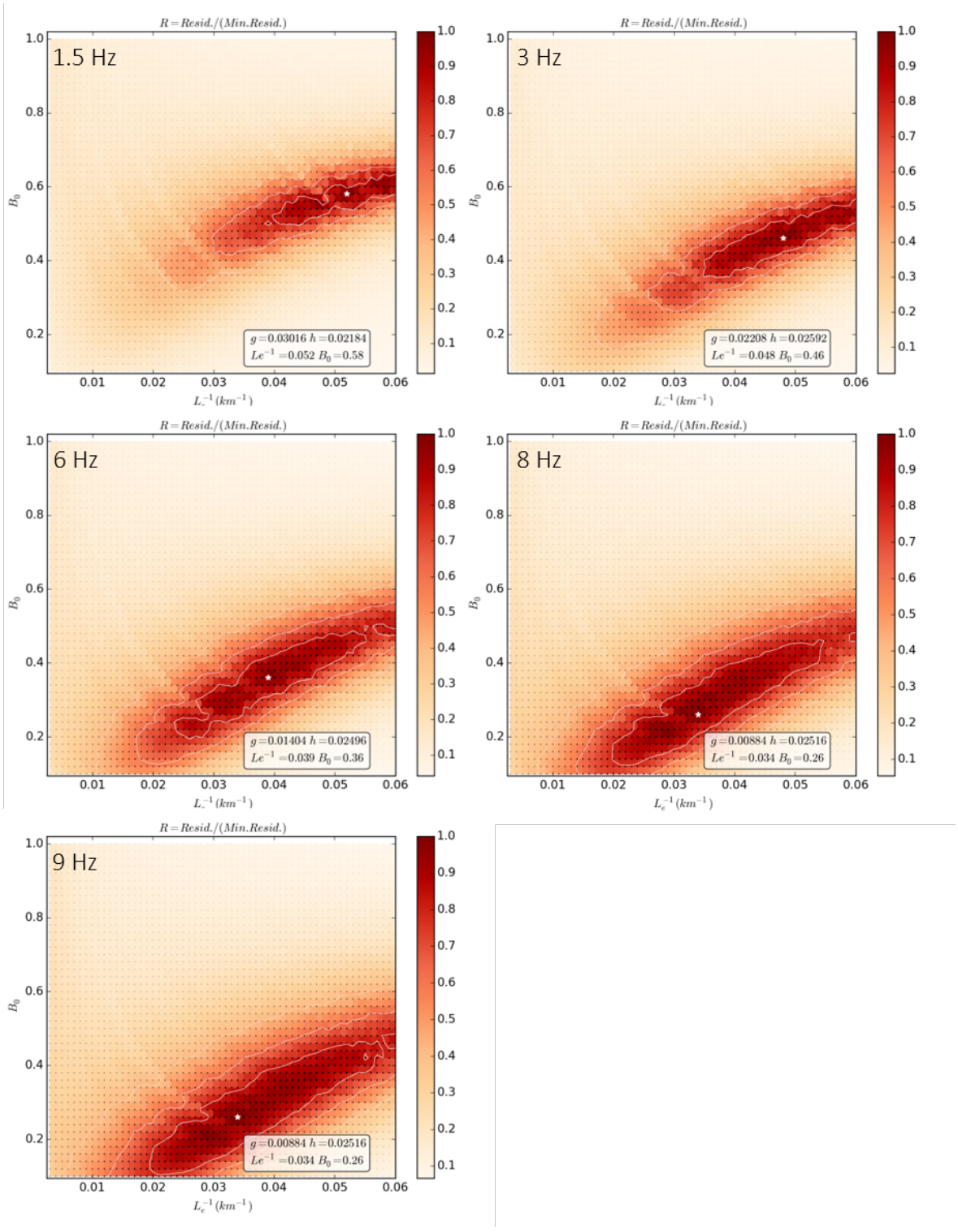

Figure 3.2. Residual maps of best fitting process of AFSR station for each center frequency is shown. Colors vary according to normalized residual value. The white star shows the best pair that fits the observed data.

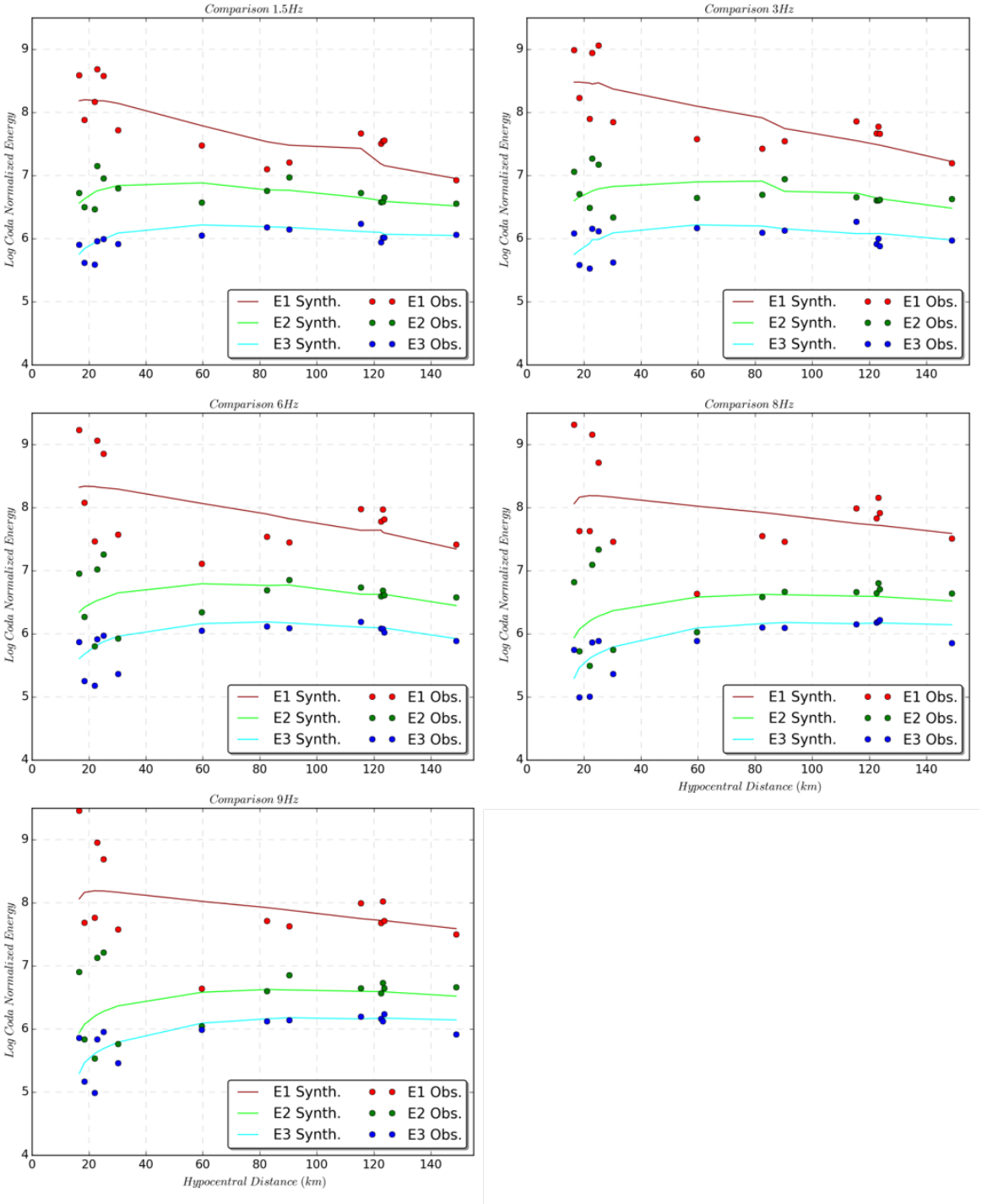

Figure 3.3. Comparison of observed energy density(circles) and the synthetic energy curves given by the best pair of L_e^{-1} and B_0 versus hypocentral distance for BNN station. Colors represents each time-windows.

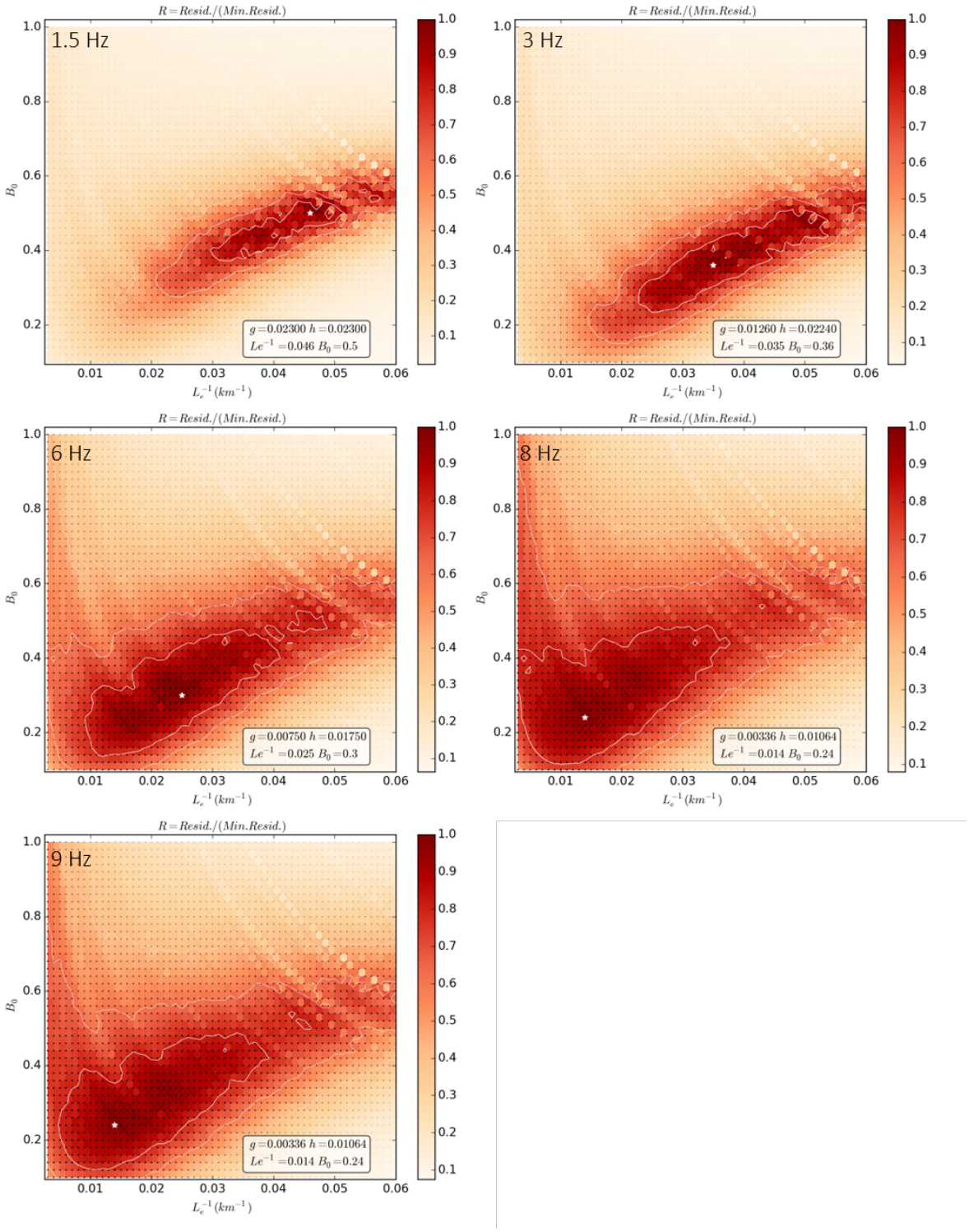

Figure 3.4. Residual maps of best fitting process of BNN station for each center frequency is shown. Colors vary according to normalized residual value. The white star shows the best pair that fits the observed data.

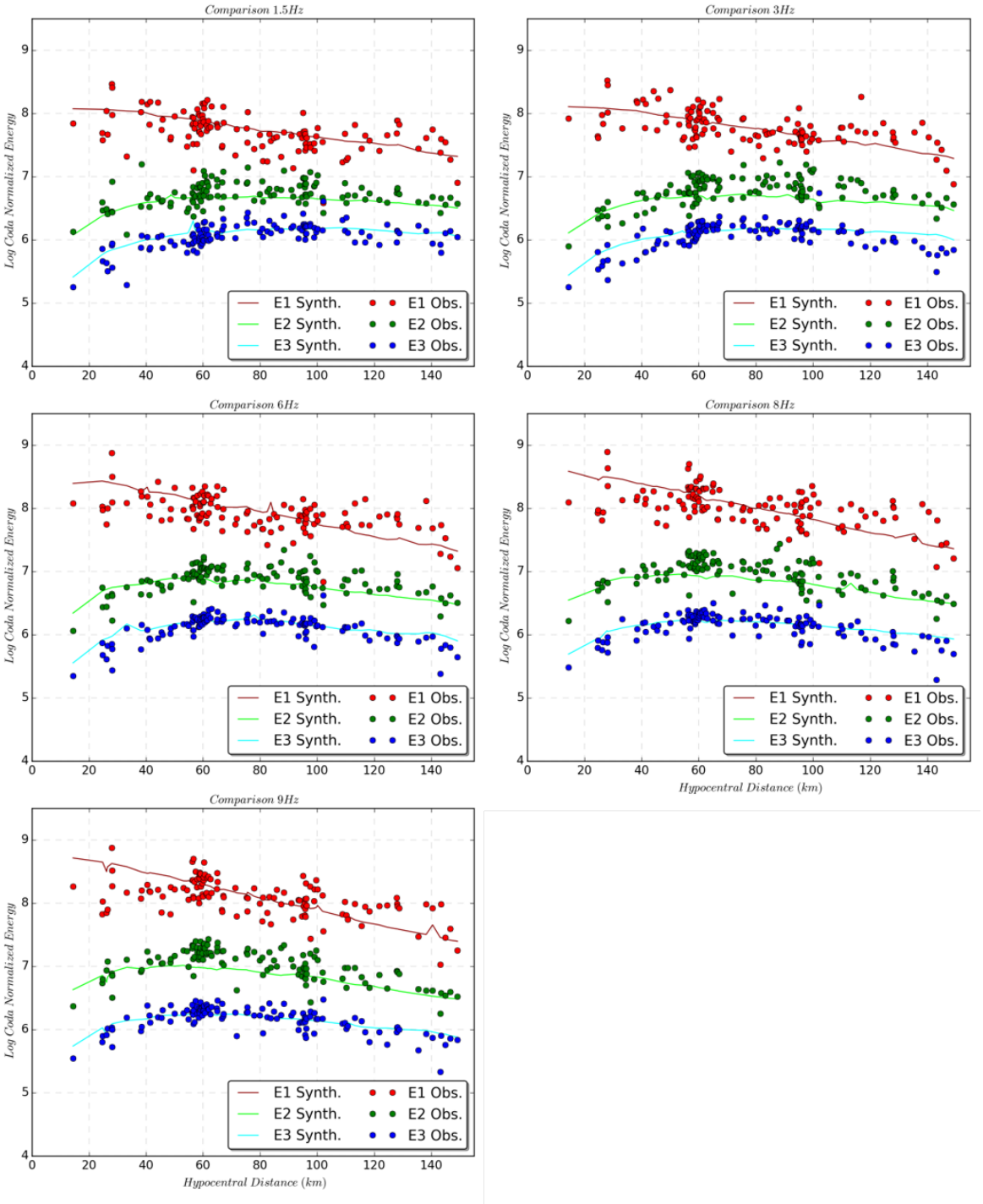

Figure 3.5. Comparison of observed energy density(circles) and the synthetic energy curves given by the best pair of L_e^{-1} and B_0 versus hypocentral distance for BR131 station. Colors represents each time-windows.

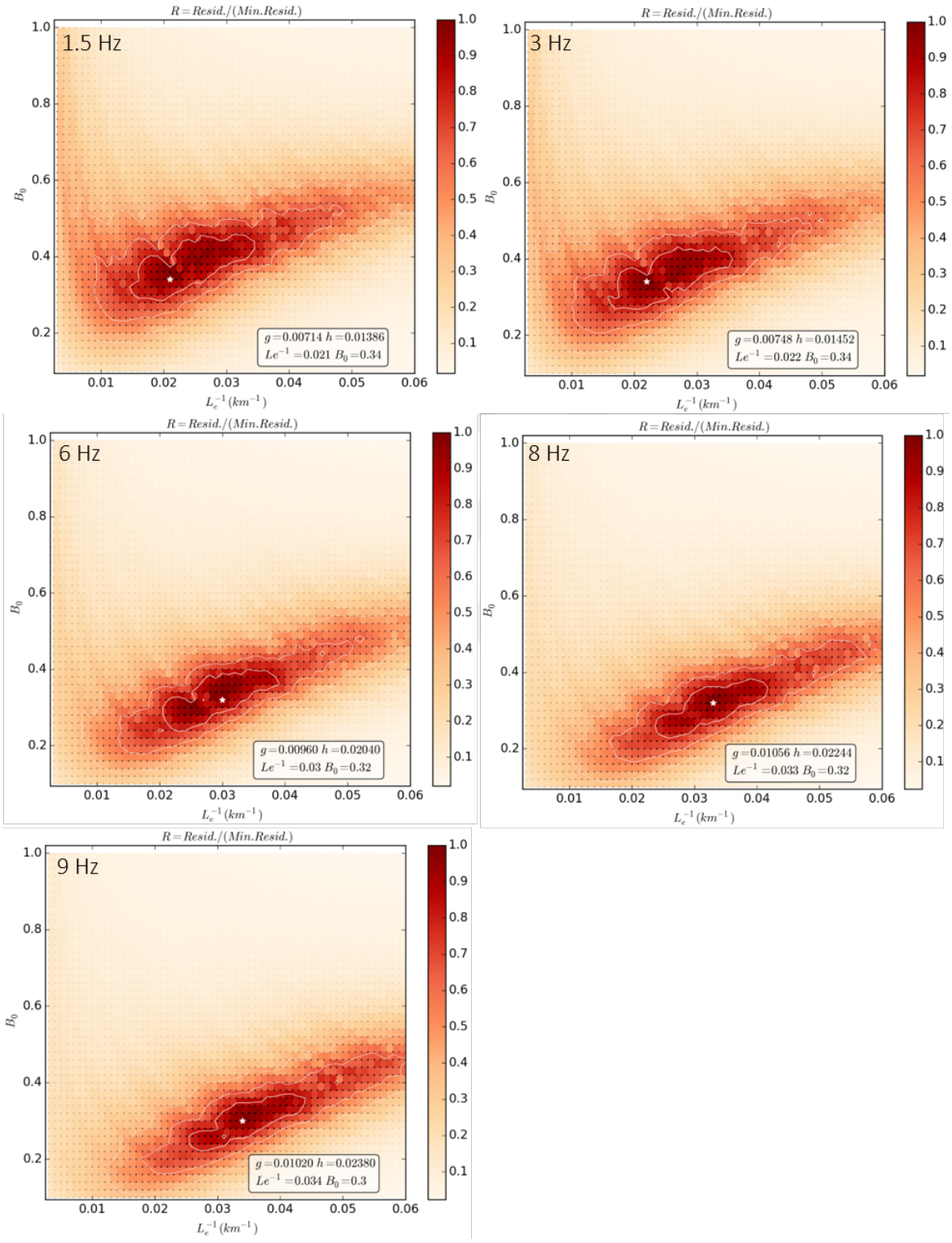

Figure 3.6. Residual maps of best fitting process of BR131 station for each center frequency is shown. Colors vary according to normalized residual value. The white star shows the best pair that fits the observed data.

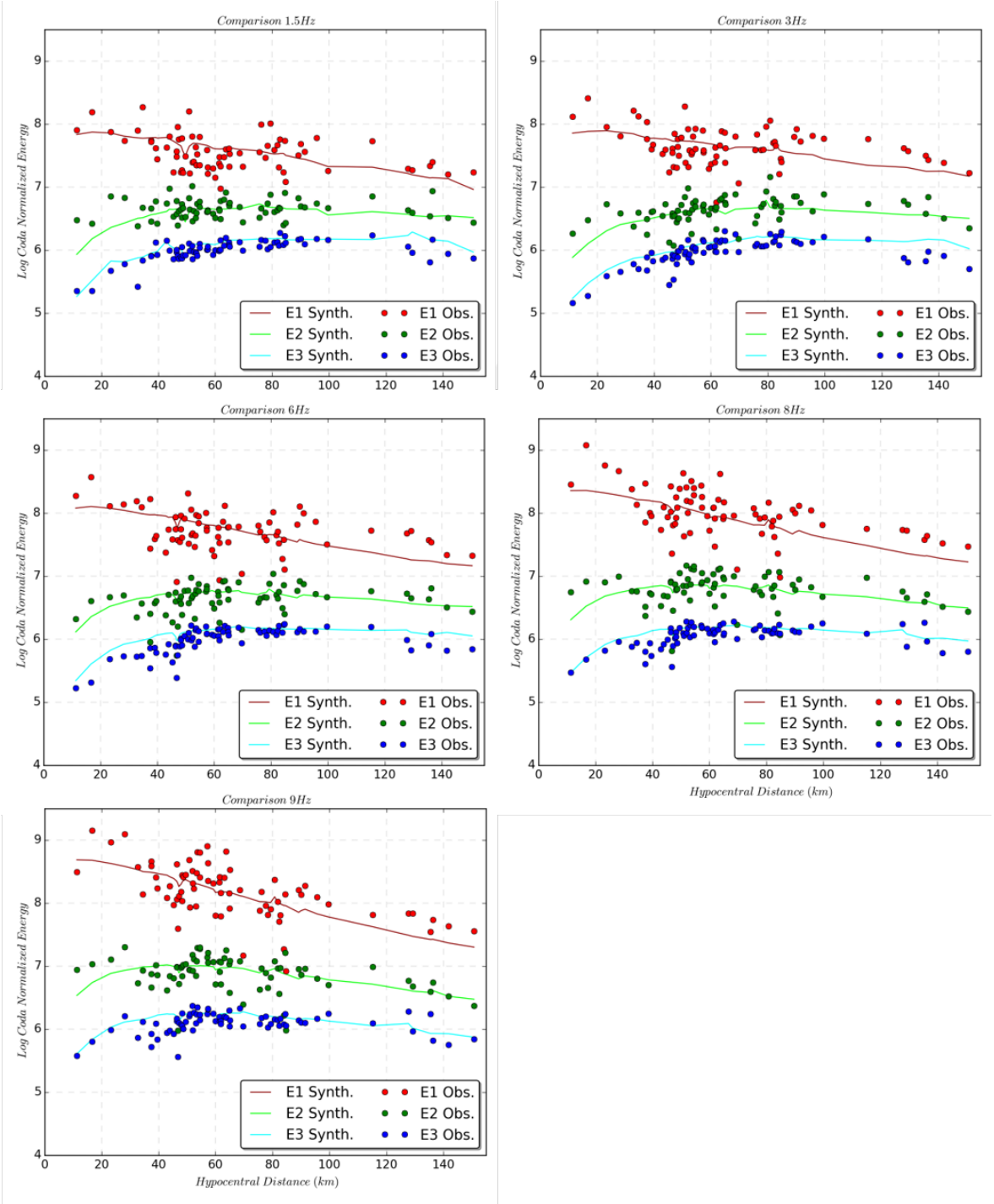

Figure 3.7. Comparison of observed energy density(circles) and the synthetic energy curves given by the best pair of L_e^{-1} and B_0 versus hypocentral distance for BR231 station. Colors represents each time-windows.

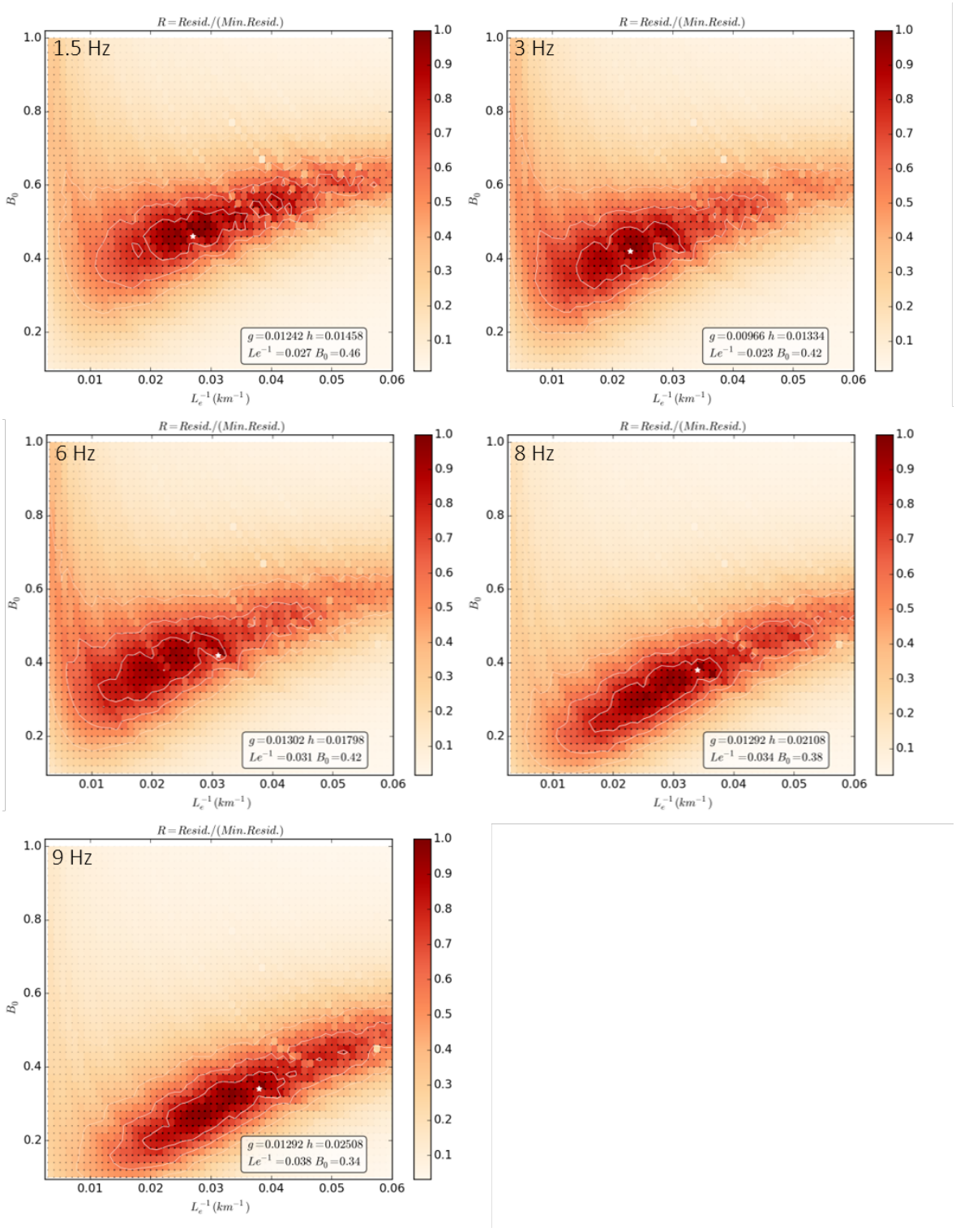

Figure 3.8. Residual maps of best fitting process of BR231 station for each center frequency is shown. Colors vary according to normalized residual value. The white star shows the best pair that fits the observed data.

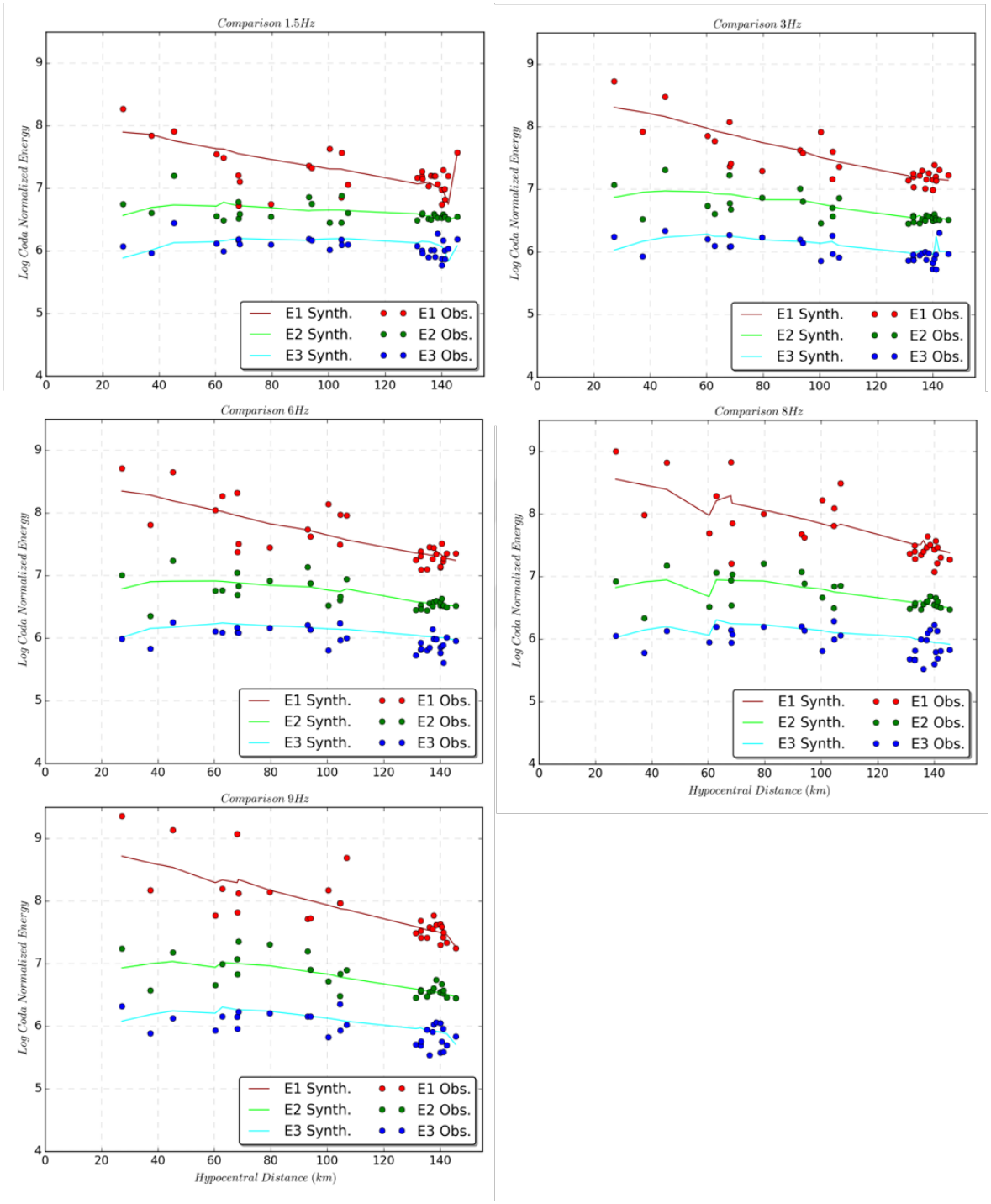

Figure 3.9. Comparison of observed energy density(circles) and the synthetic energy curves given by the best pair of L_e^{-1} and B_0 versus hypocentral distance for CANT station. Colors represents each time-windows.

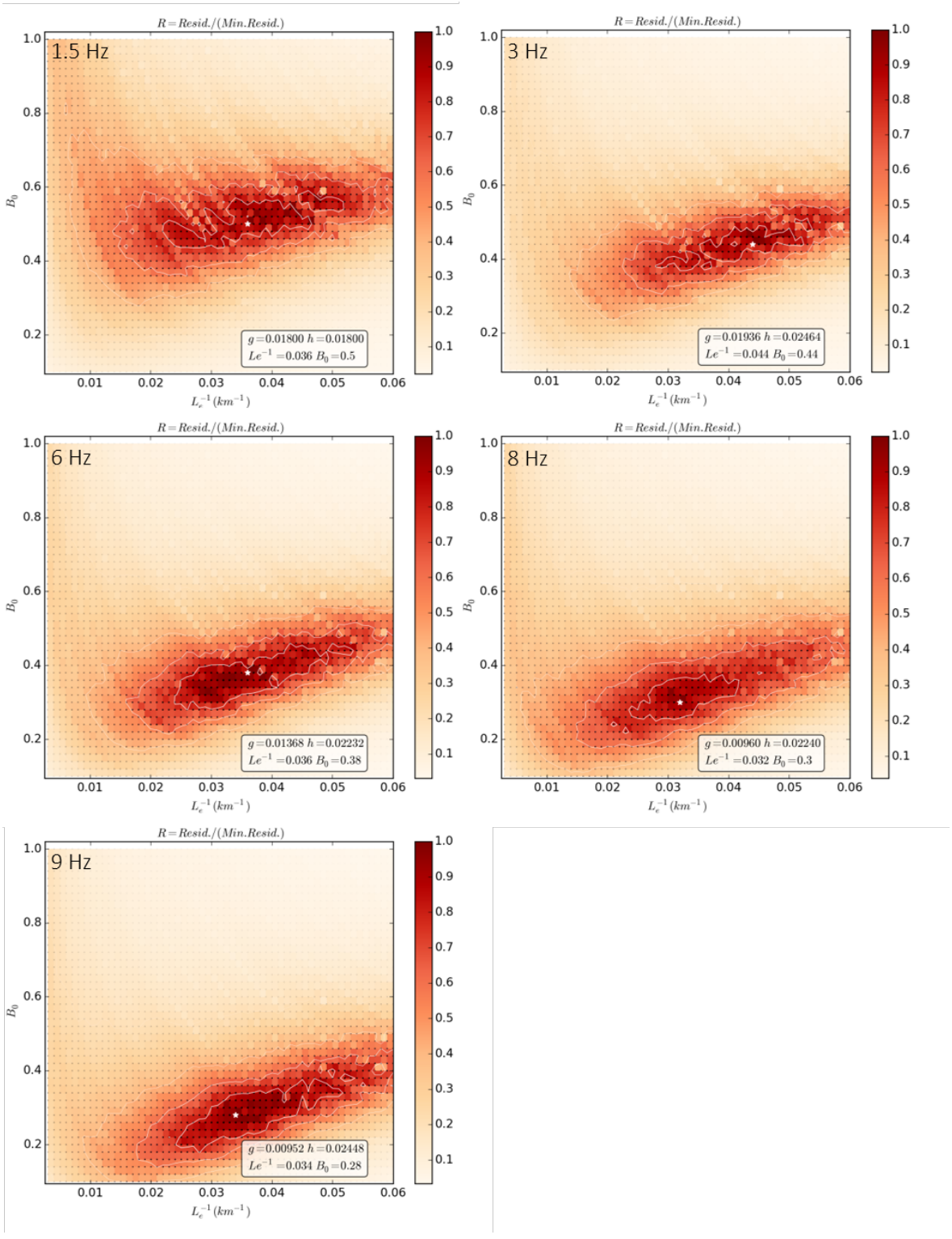

Figure 3.10. Residual maps of best fitting process of CANT station for each center frequency is shown. Colors vary according to normalized residual value. The white star shows the best pair that fits the observed data.

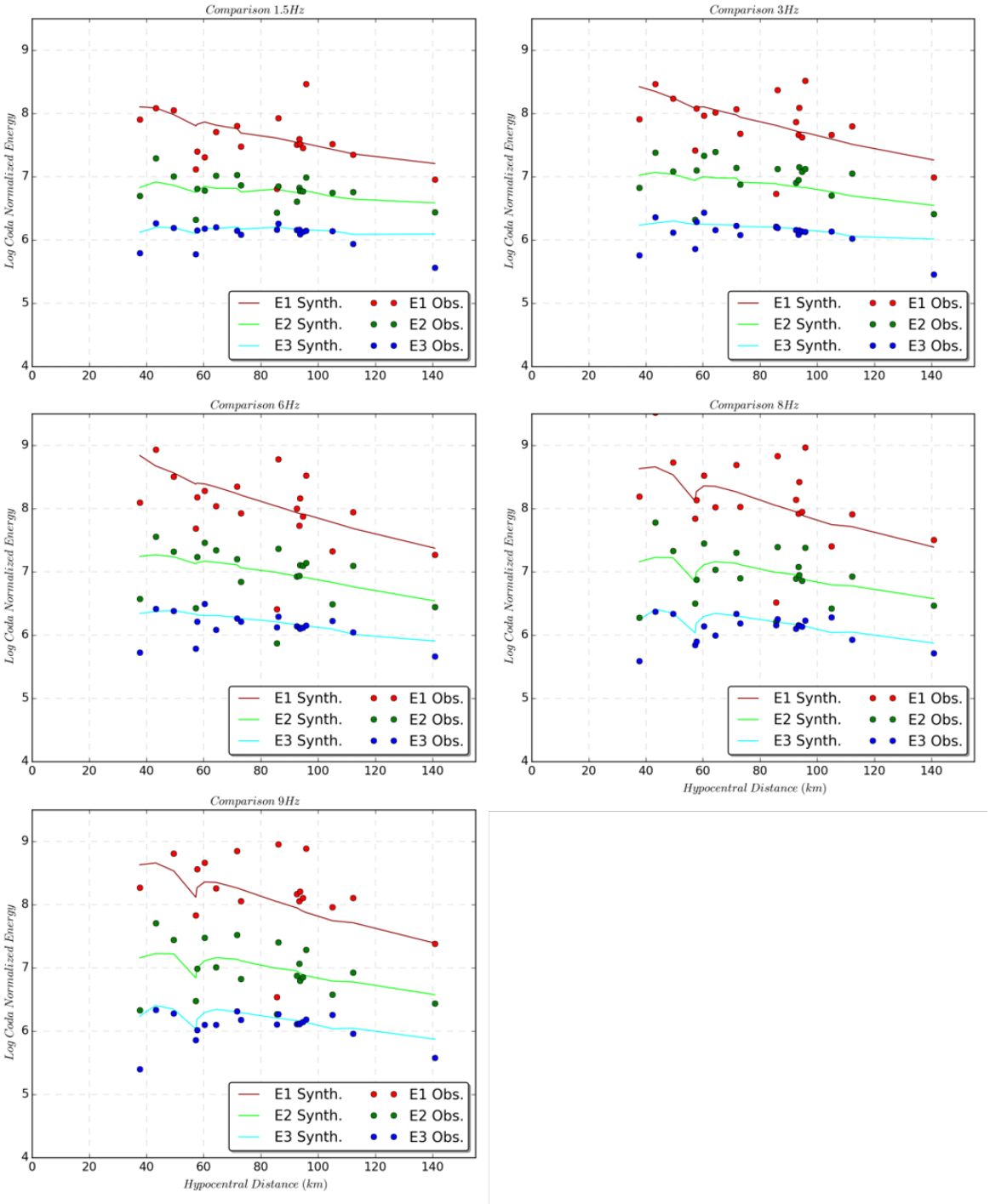

Figure 3.11. Comparison of observed energy density(circles) and the synthetic energy curves given by the best pair of L_e^{-1} and B_0 versus hypocentral distance for CHBY station. Colors represents each time-windows.

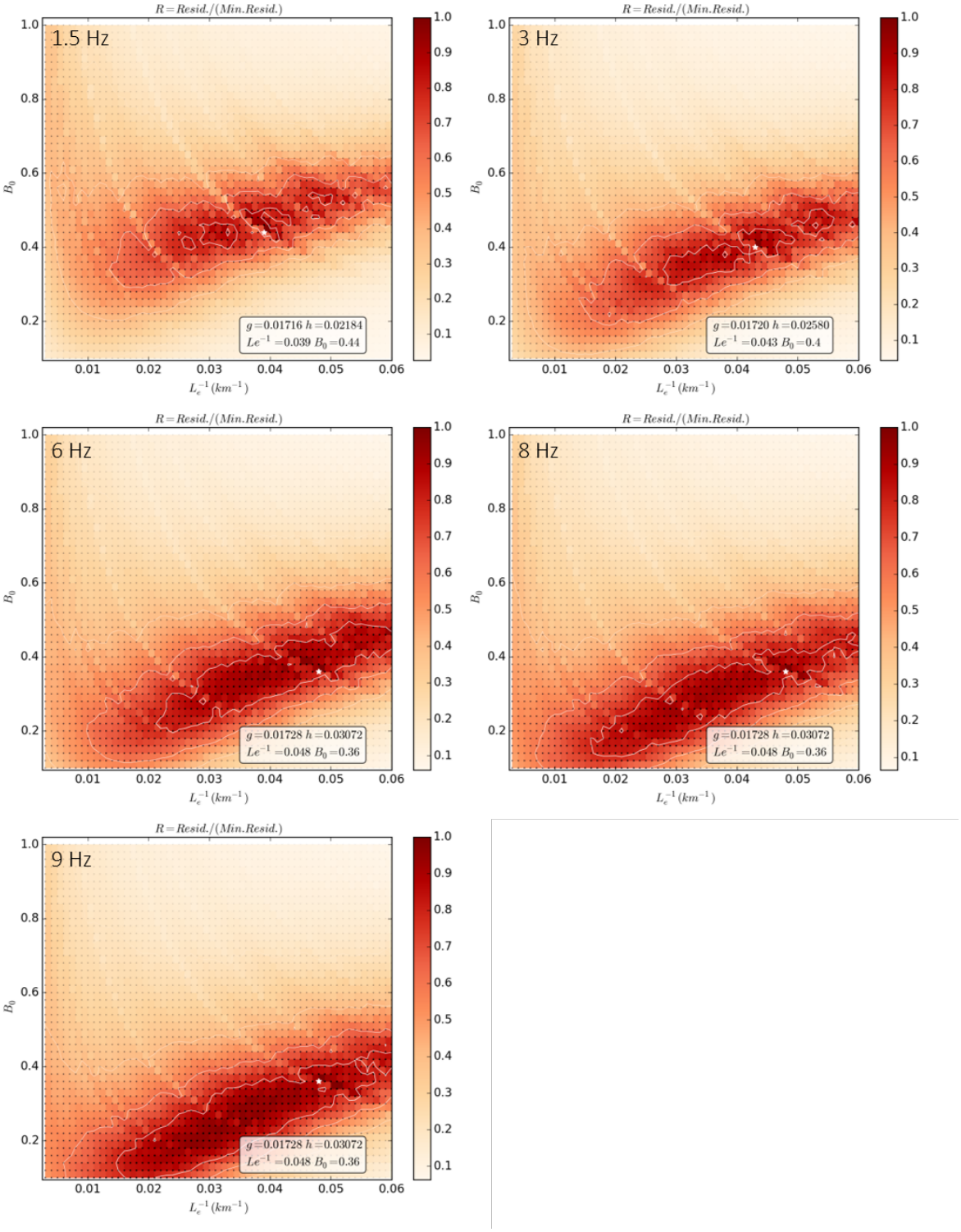

Figure 3.12. Residual maps of best fitting process of CHBY station for each center frequency is shown. Colors vary according to normalized residual value. The white star shows the best pair that fits the observed data.

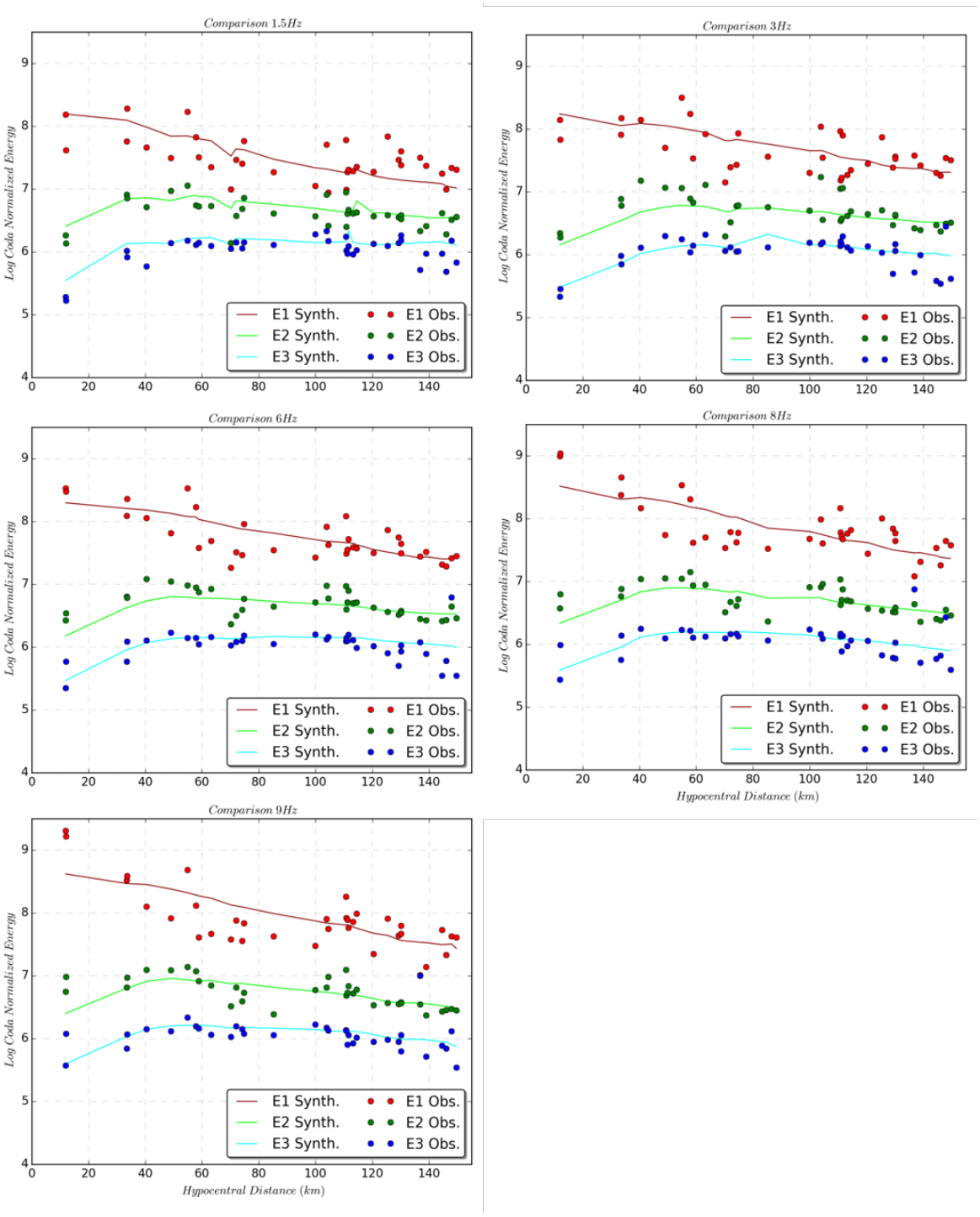

Figure 3.13. Comparison of observed energy density(circles) and the synthetic energy curves given by the best pair of L_e^{-1} and B_0 versus hypocentral distance for CORM station. Colors represents each time-windows.

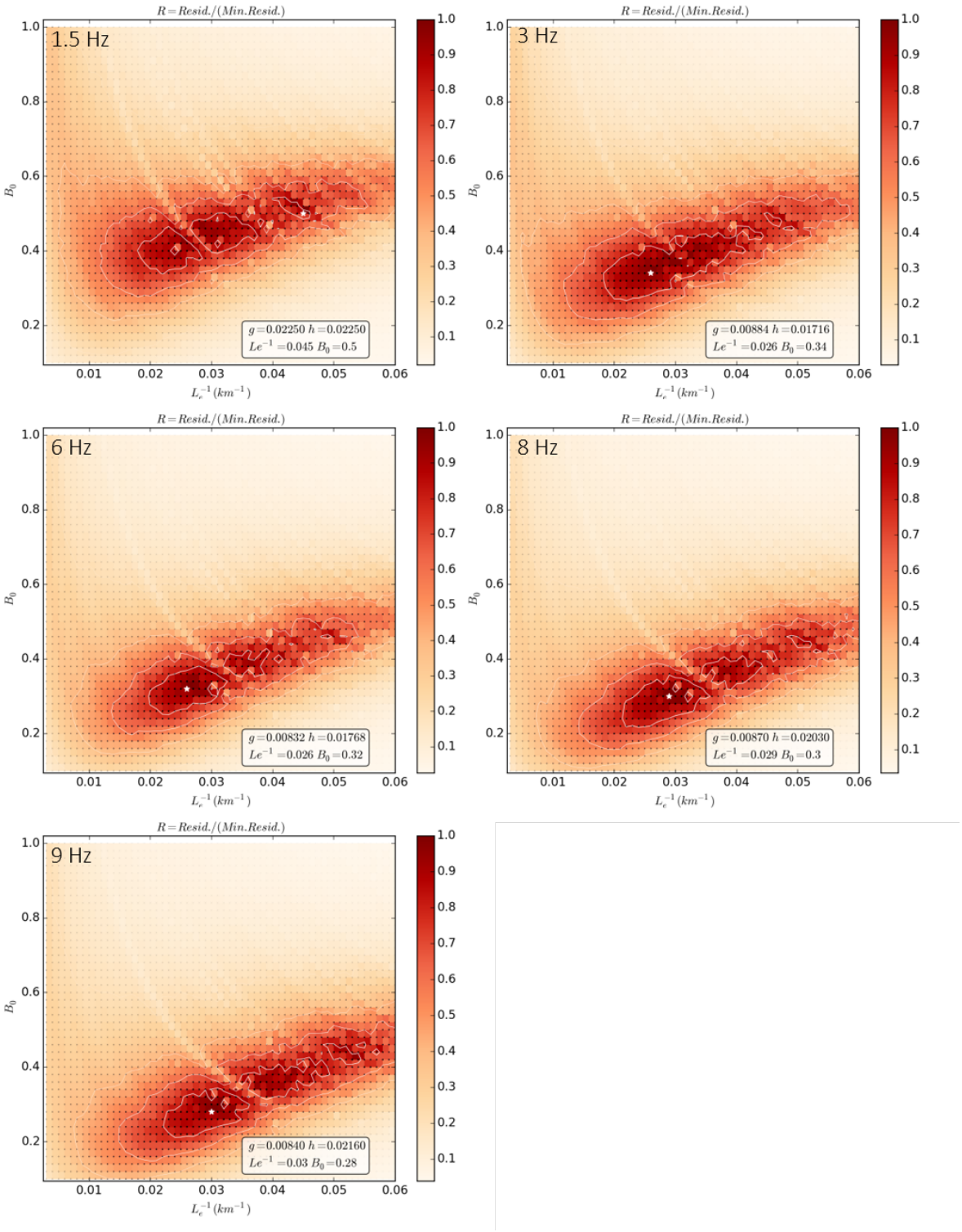

Figure 3.14. Residual maps of best fitting process of CORM station for each center frequency is shown. Colors vary according to normalized residual value. The white star shows the best pair that fits the observed data.

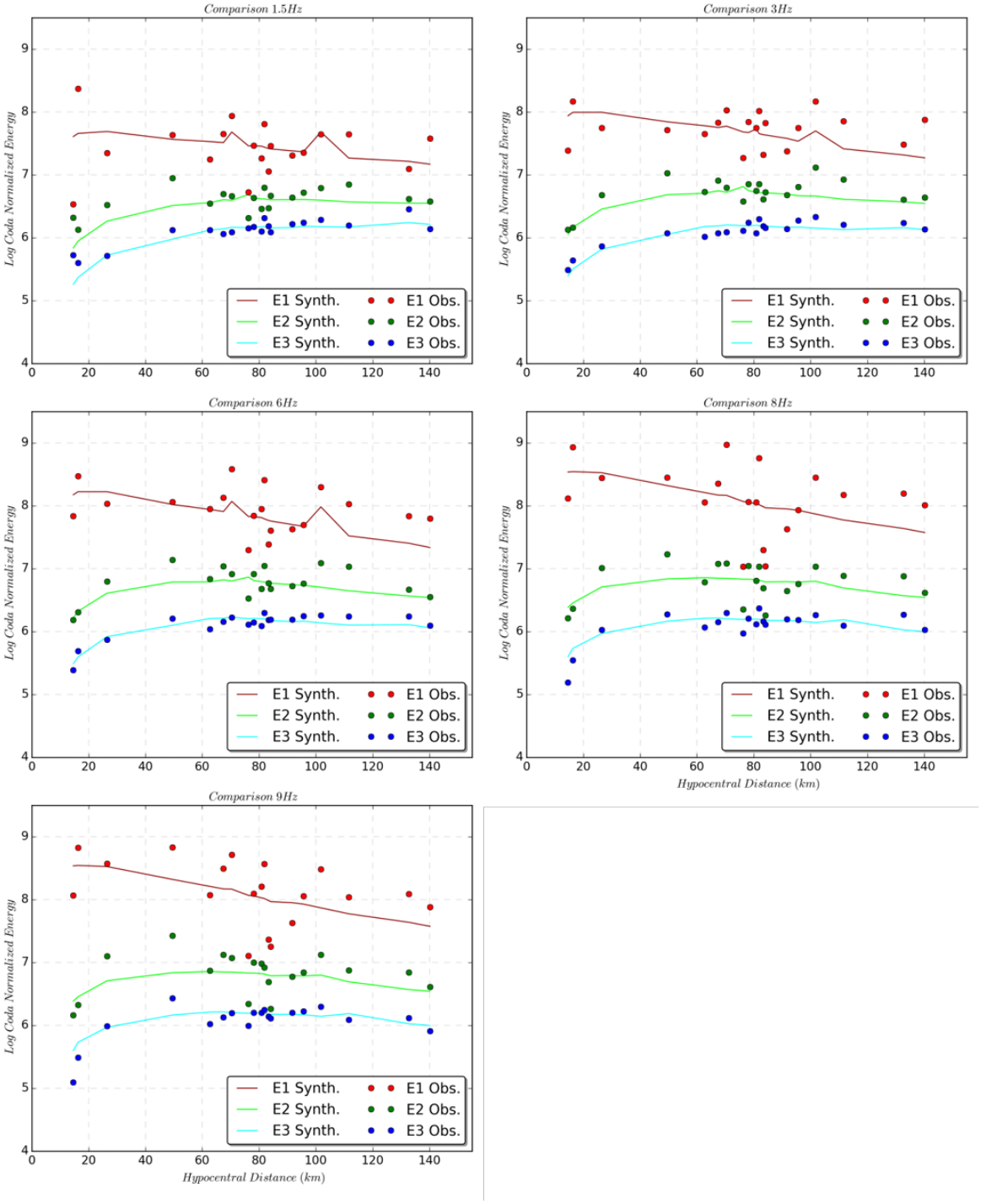

Figure 3.15. Comparison of observed energy density(circles) and the synthetic energy curves given by the best pair of L_e^{-1} and B_0 versus hypocentral distance for GULA station. Colors represents each time-windows.

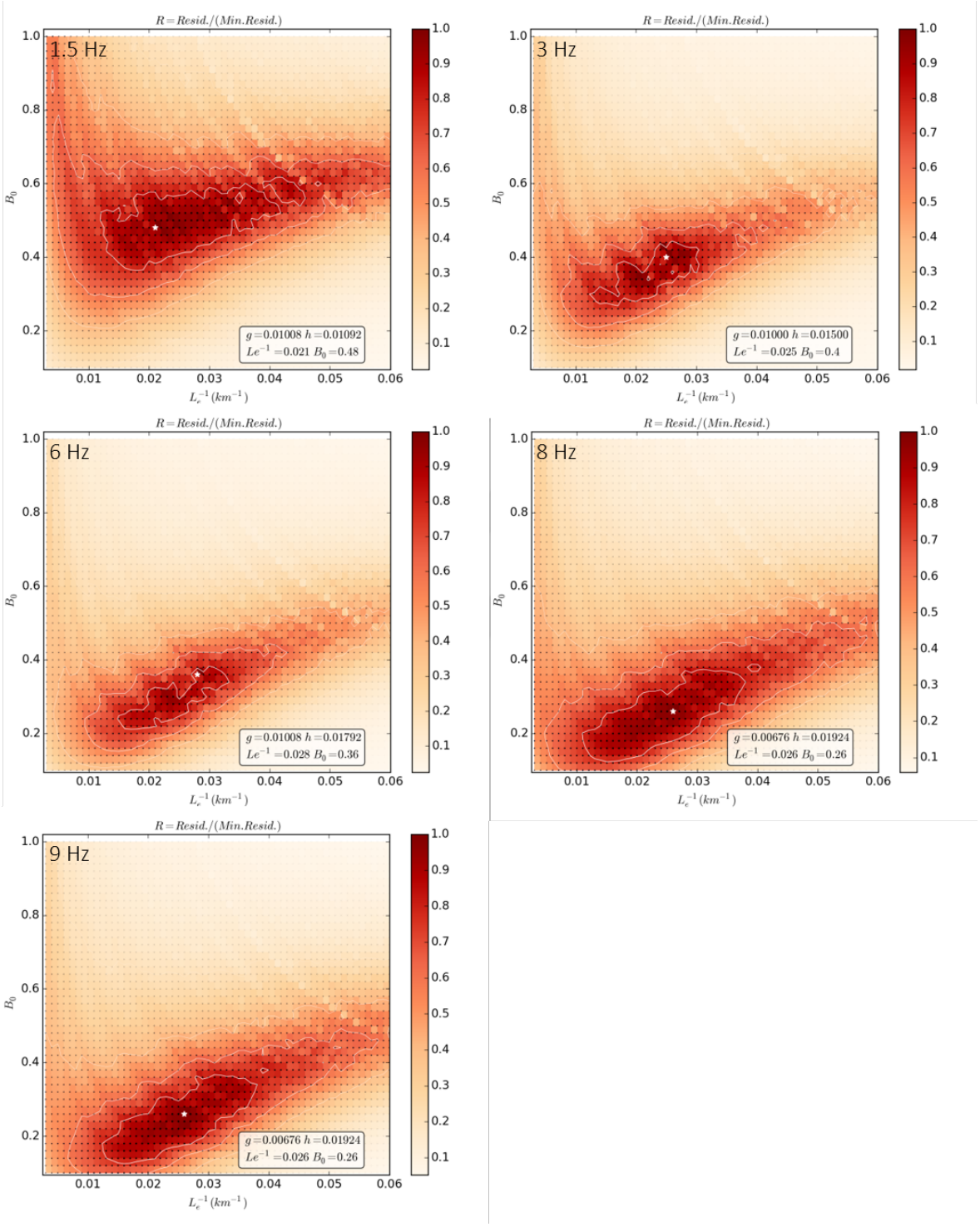

Figure 3.16. Residual maps of best fitting process of GULA station for each center frequency is shown. Colors vary according to normalized residual value. The white star shows the best pair that fits the observed data.

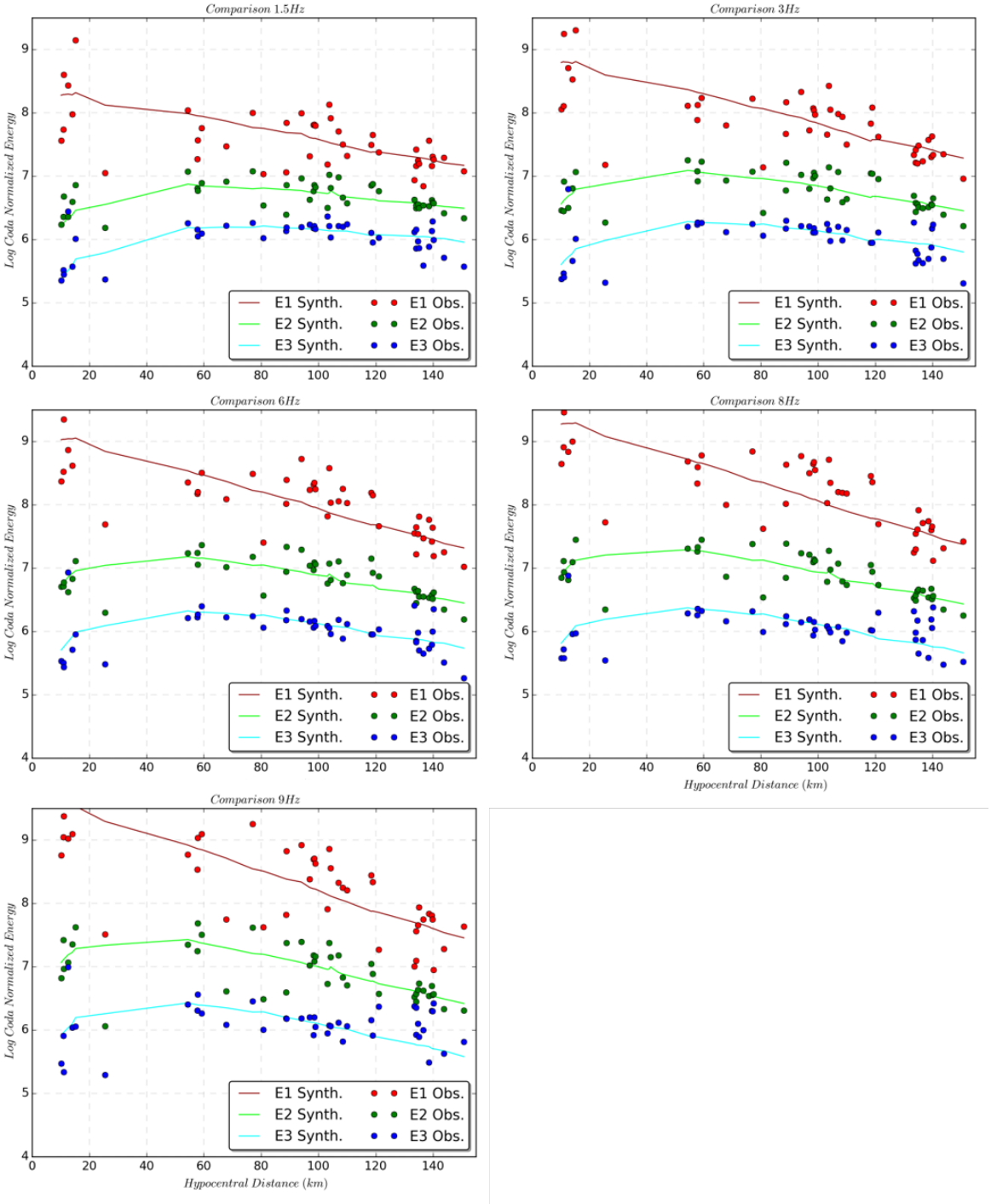

Figure 3.17. Comparison of observed energy density(circles) and the synthetic energy curves given by the best pair of L_e^{-1} and B_0 versus hypocentral distance for KONT station. Colors represents each time-windows.

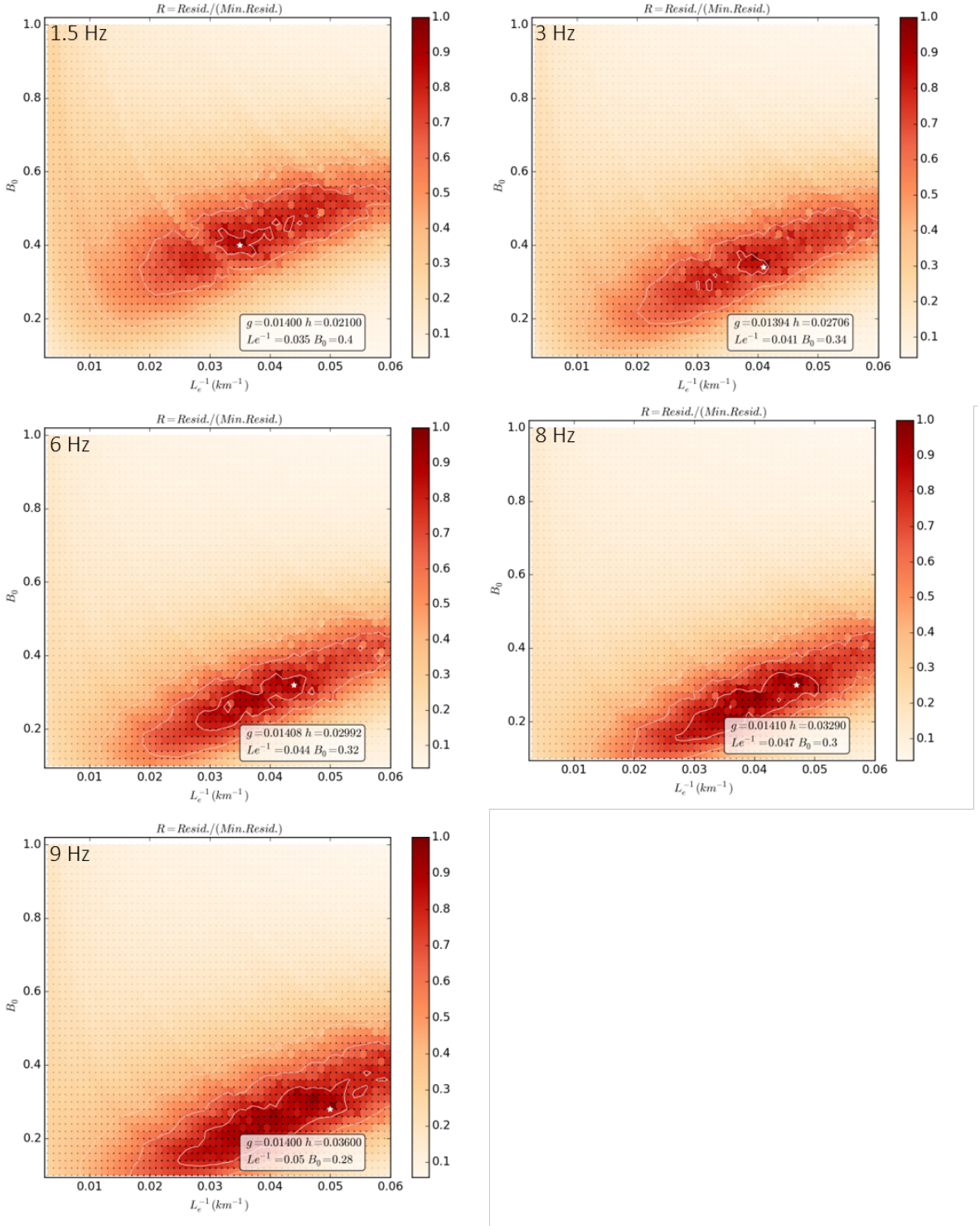

Figure 3.18. Residual maps of best fitting process of KONT station for each center frequency is shown. Colors vary according to normalized residual value. The white star shows the best pair that fits the observed data.

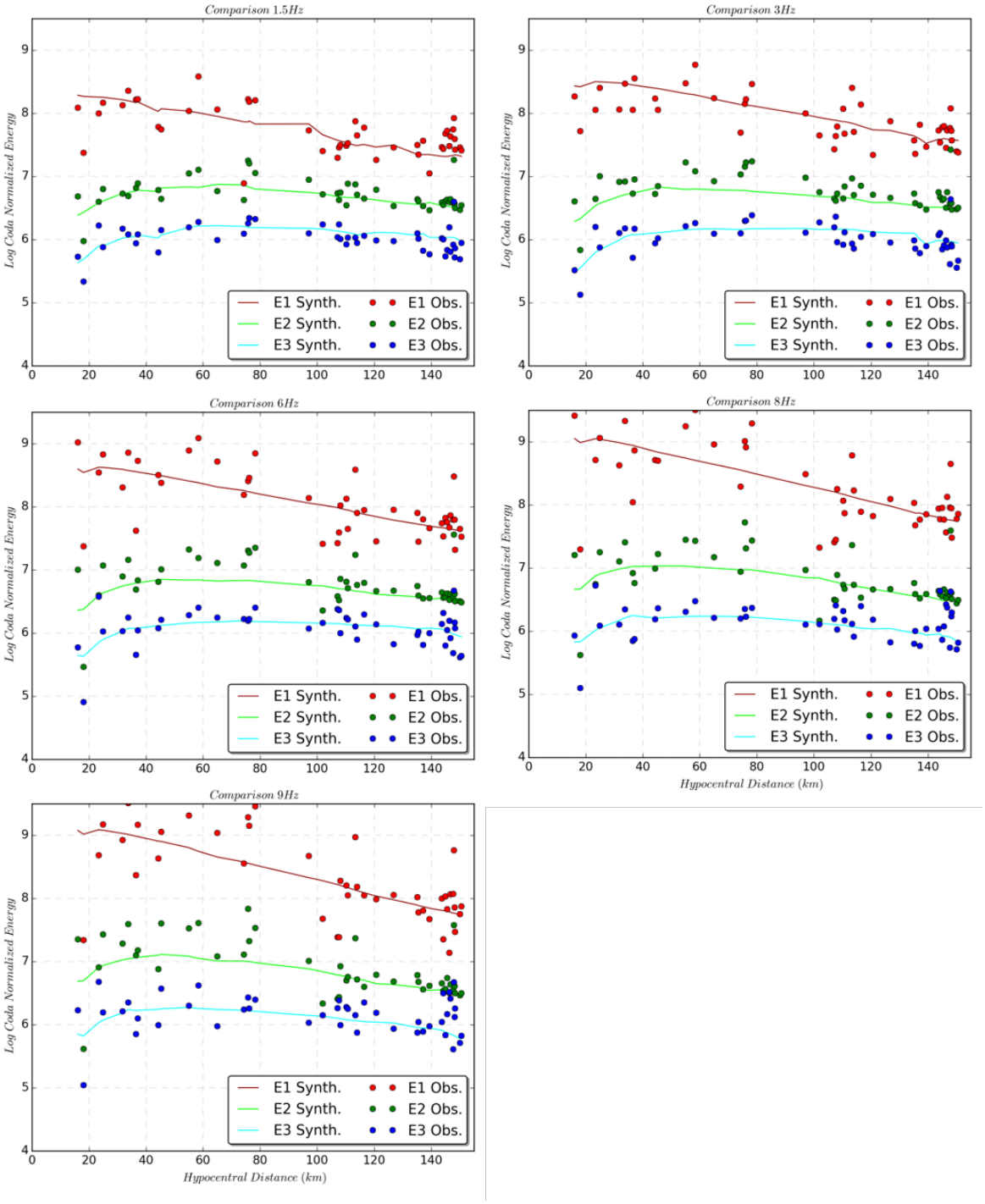

Figure 3.19. Comparison of observed energy density(circles) and the synthetic energy curves given by the best pair of L_e^{-1} and B_0 versus hypocentral distance for LADK station. Colors represents each time-windows.

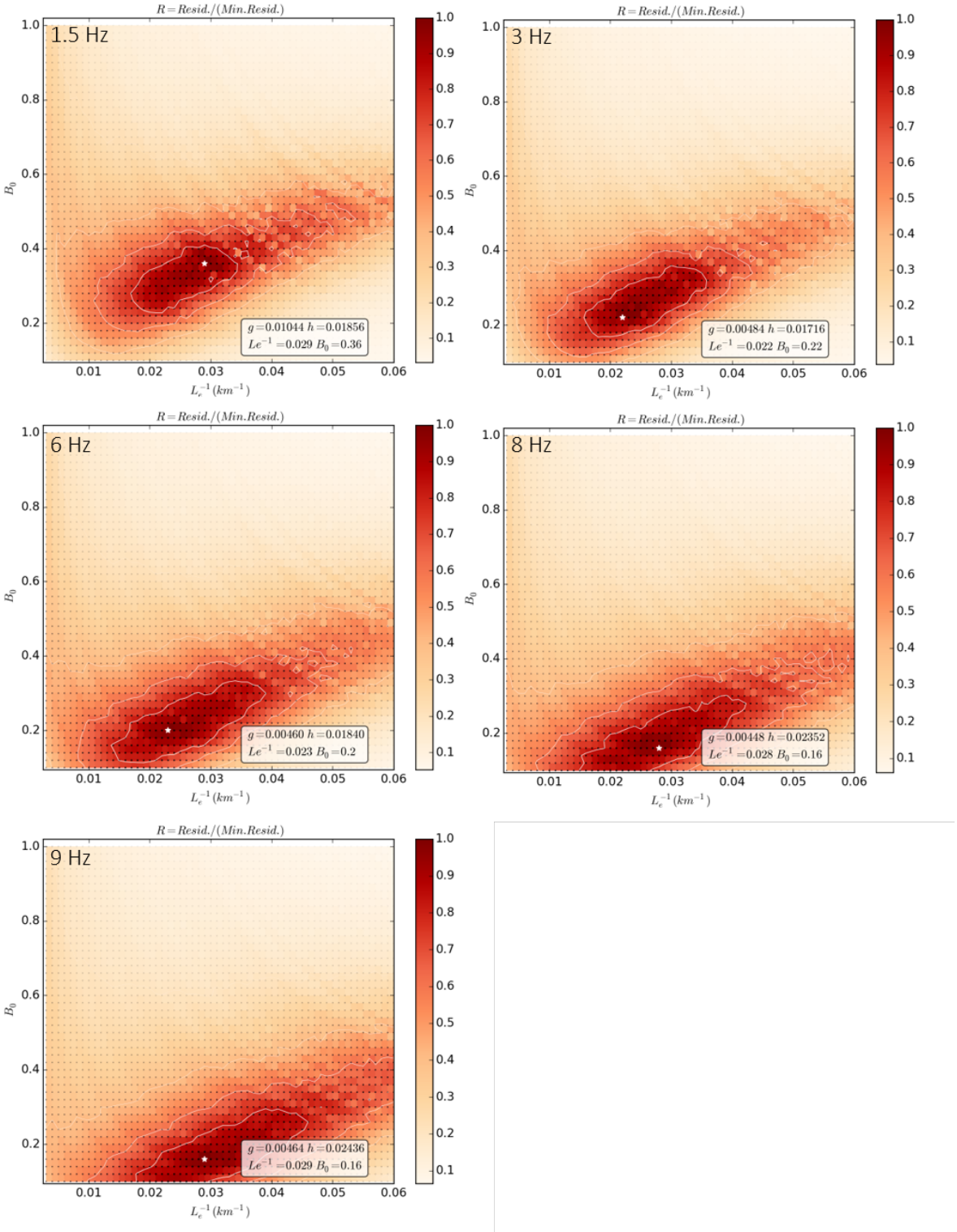

Figure 3.20. Residual maps of best fitting process of LADK station for each center frequency is shown. Colors vary according to normalized residual value. The white star shows the best pair that fits the observed data.

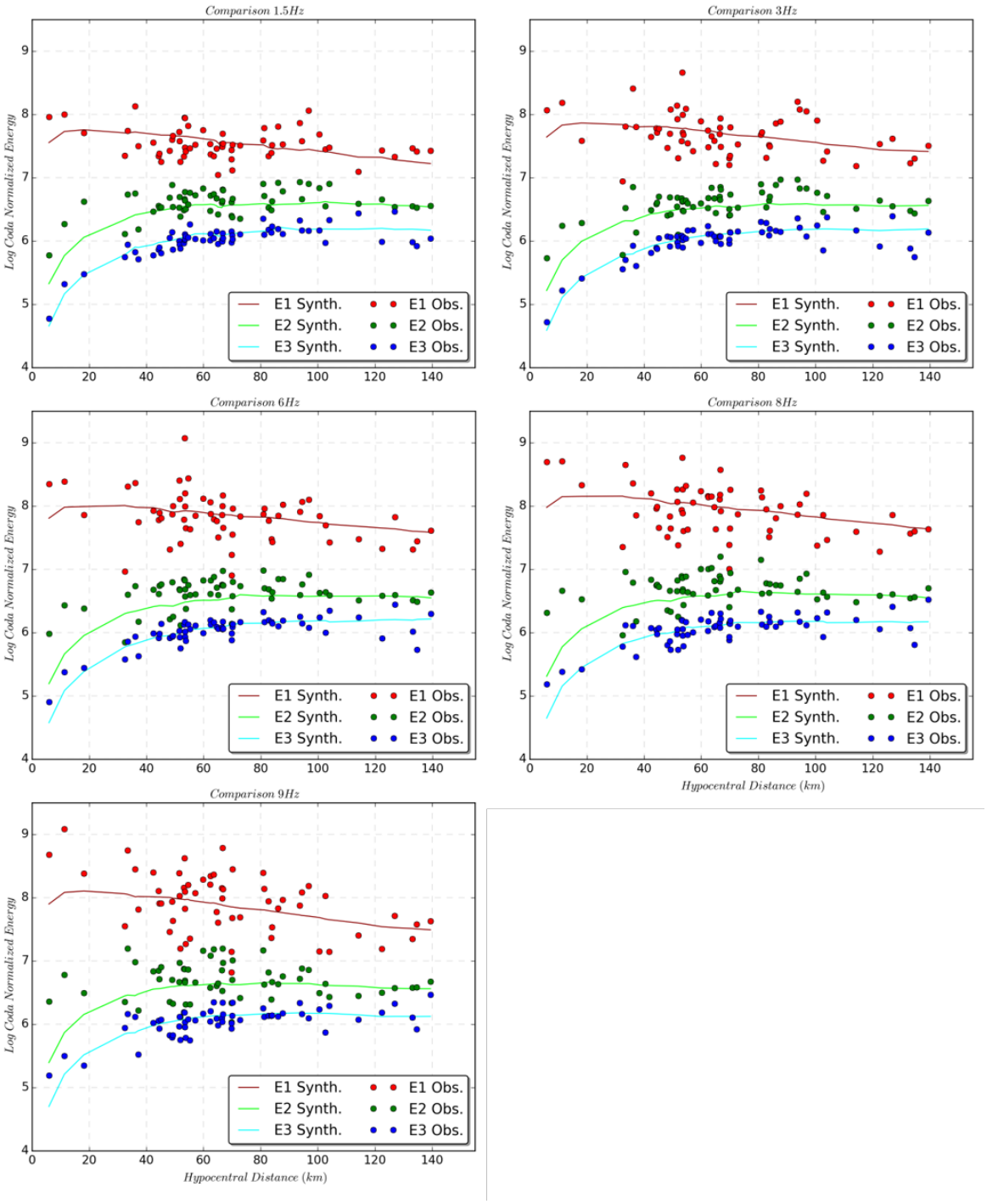

Figure 3.21. Comparison of observed energy density(circles) and the synthetic energy curves given by the best pair of L_e^{-1} and B_0 versus hypocentral distance for LOD station. Colors represents each time-windows.

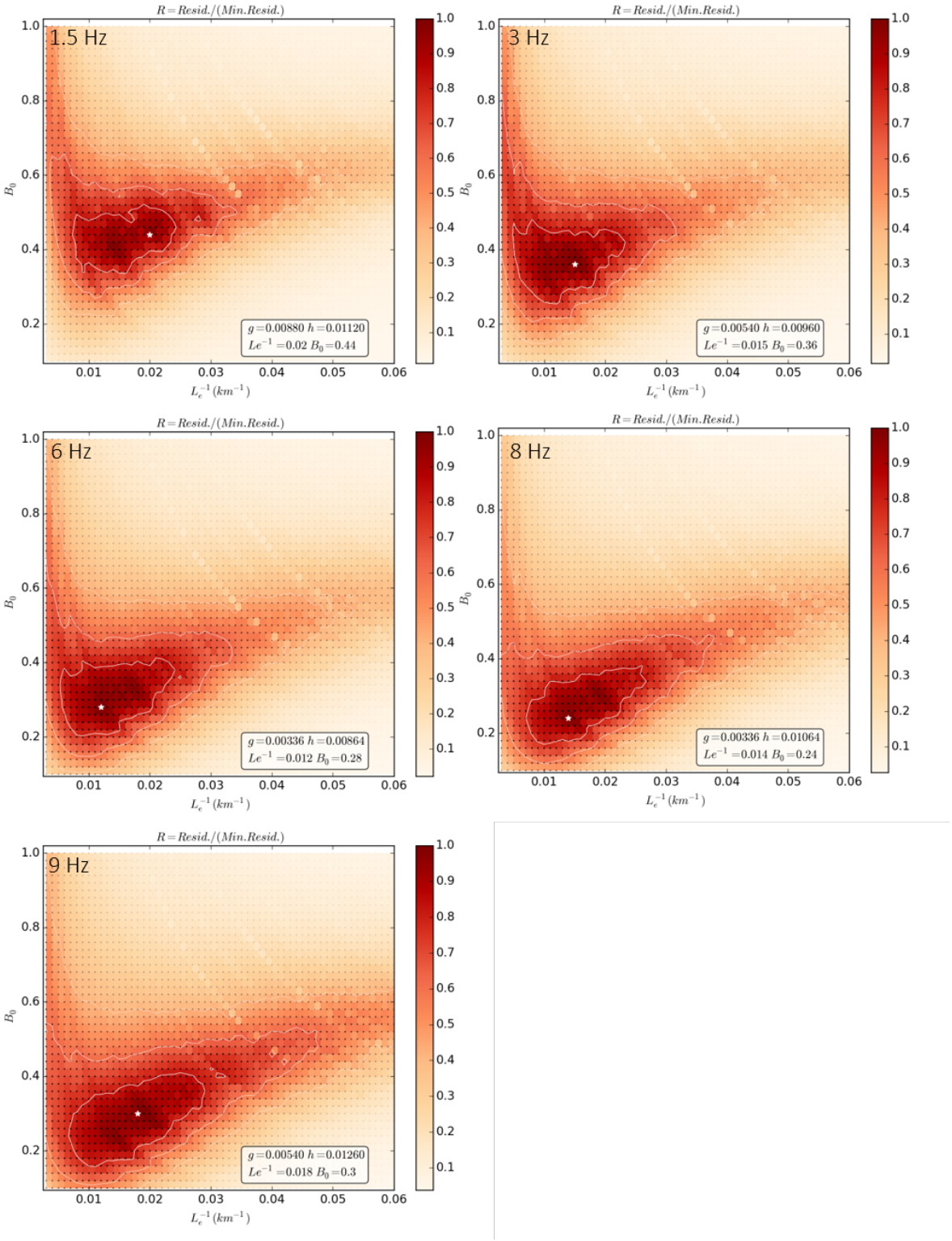

Figure 3.22. Residual maps of best fitting process of LOD station for each center frequency is shown. Colors vary according to normalized residual value. The white star shows the best pair that fits the observed data.

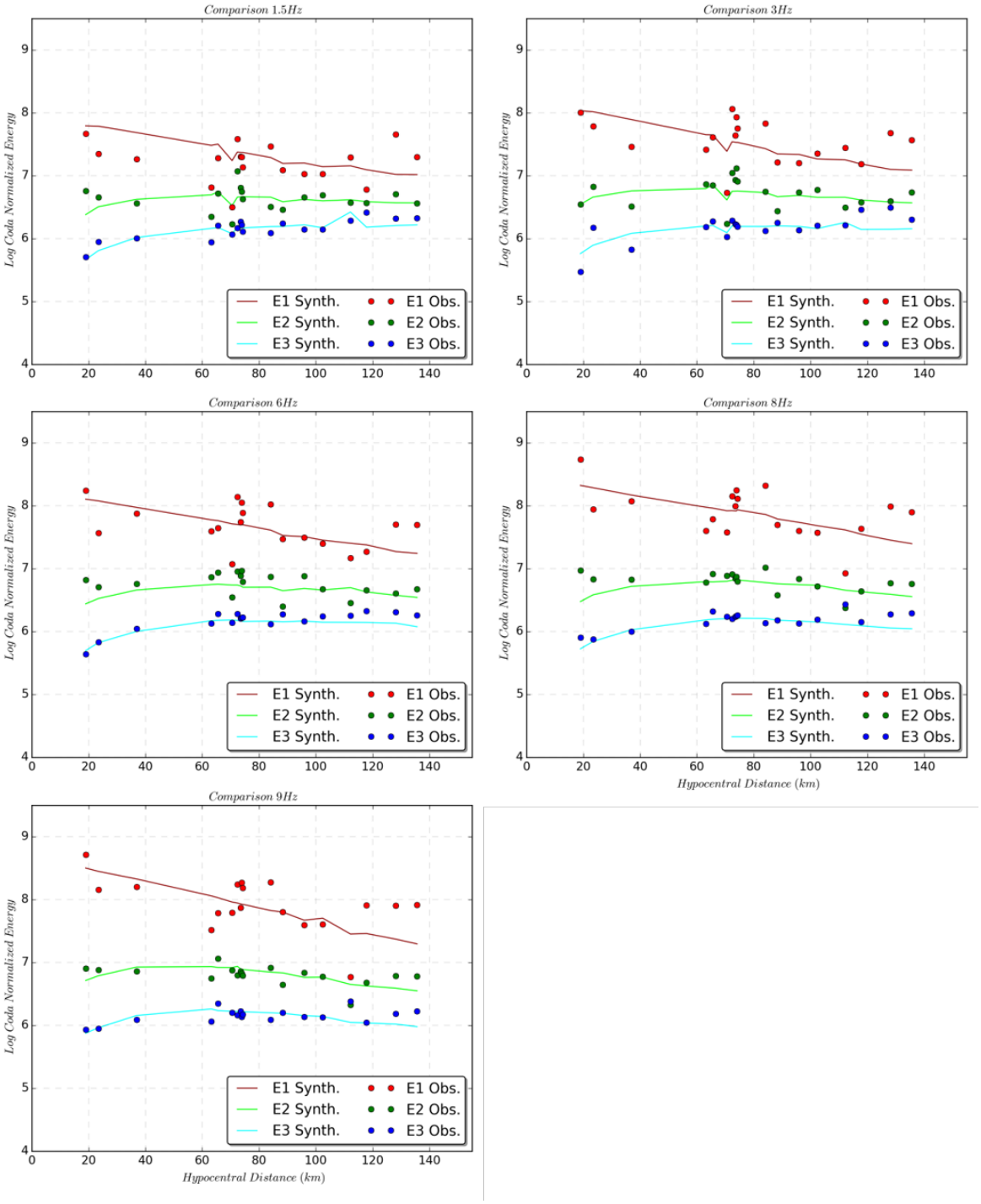

Figure 3.23. Comparison of observed energy density(circles) and the synthetic energy curves given by the best pair of L_e^{-1} and B_0 versus hypocentral distance for SERE station. Colors represents each time-windows.

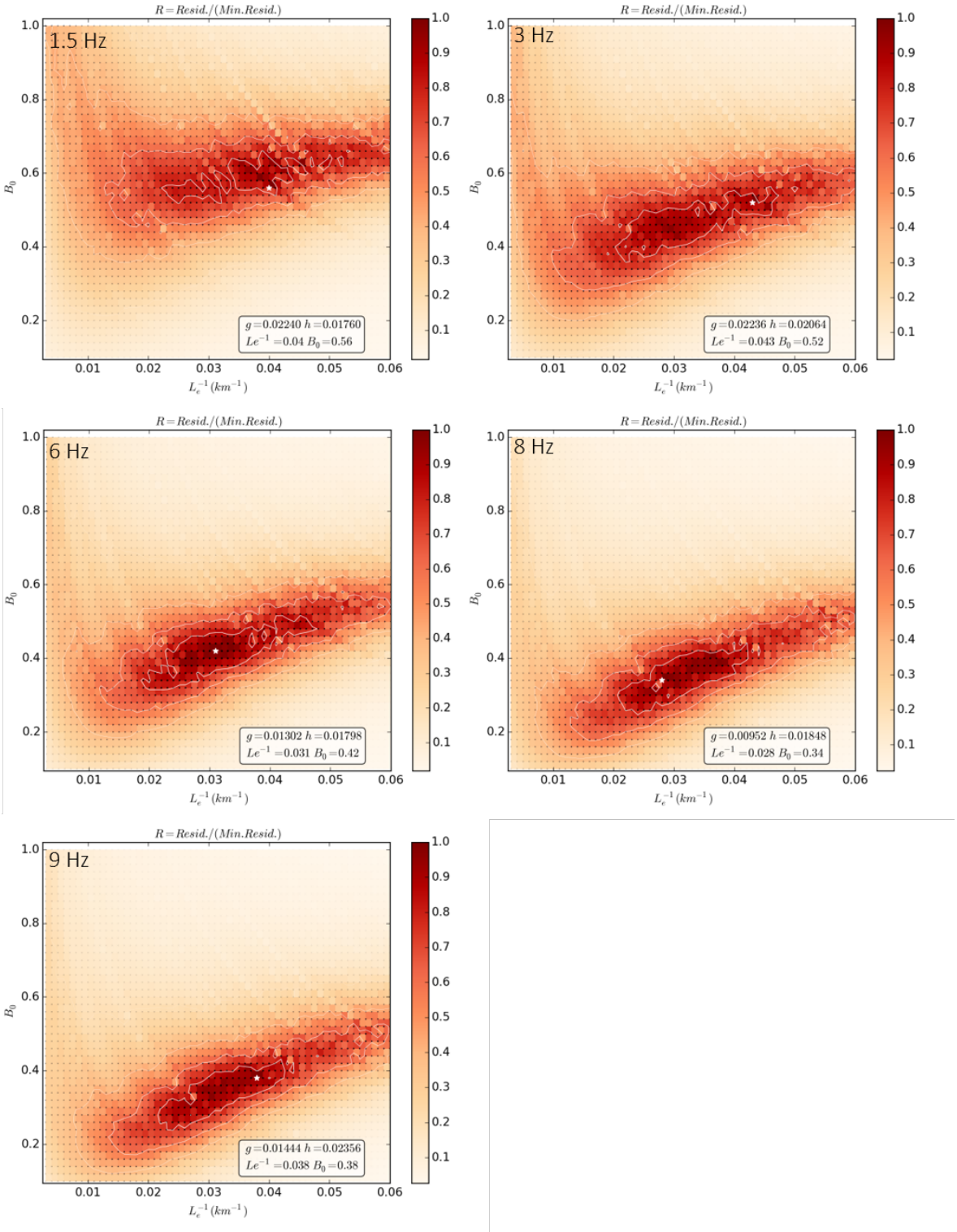

Figure 3.24. Residual maps of best fitting process of SERE station for each center frequency is shown. Colors vary according to normalized residual value. The white star shows the best pair that fits the observed data.

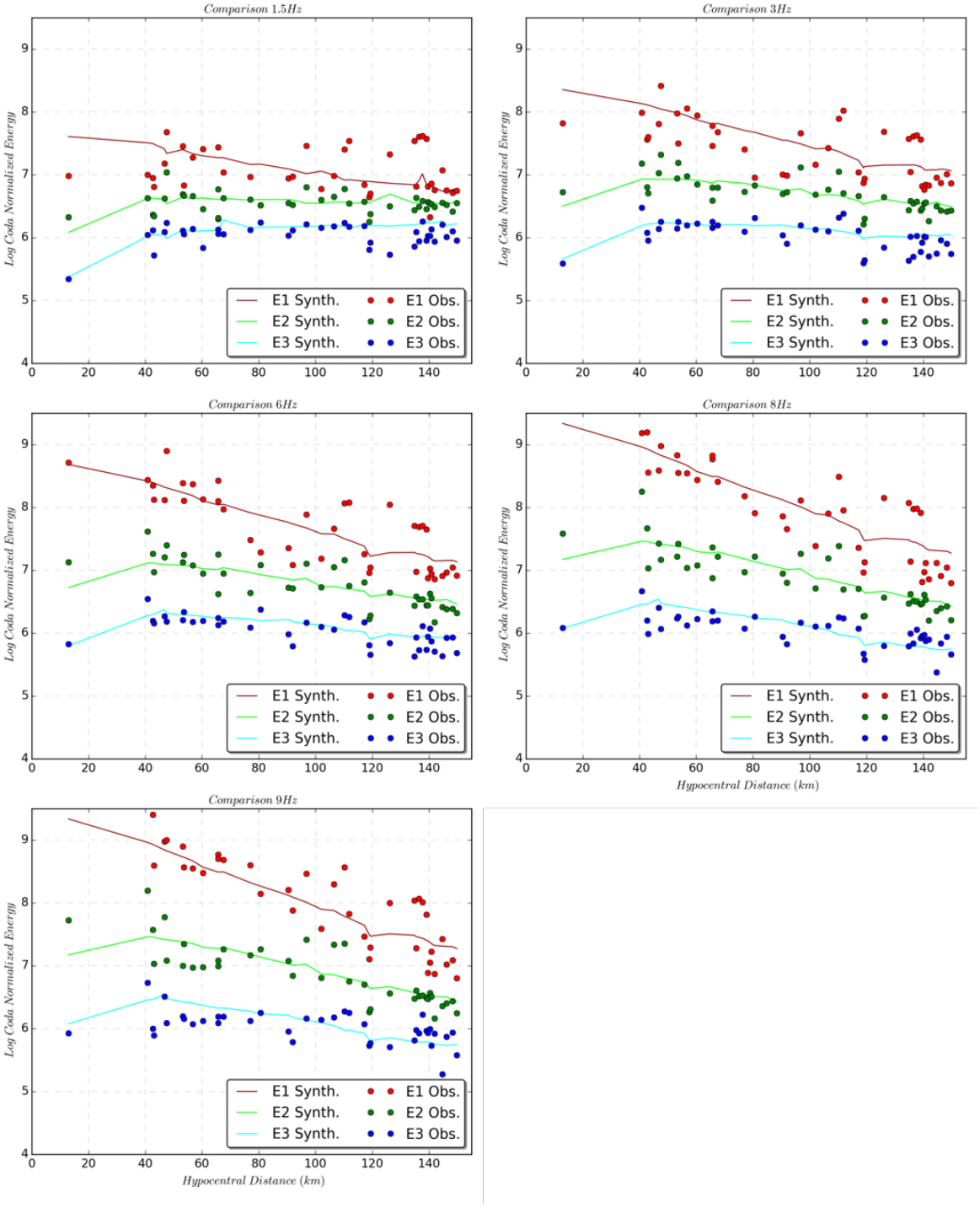

Figure 3.25. Comparison of observed energy density(circles) and the synthetic energy curves given by the best pair of L_e^{-1} and B_0 versus hypocentral distance for SULT station. Colors represents each time-windows.

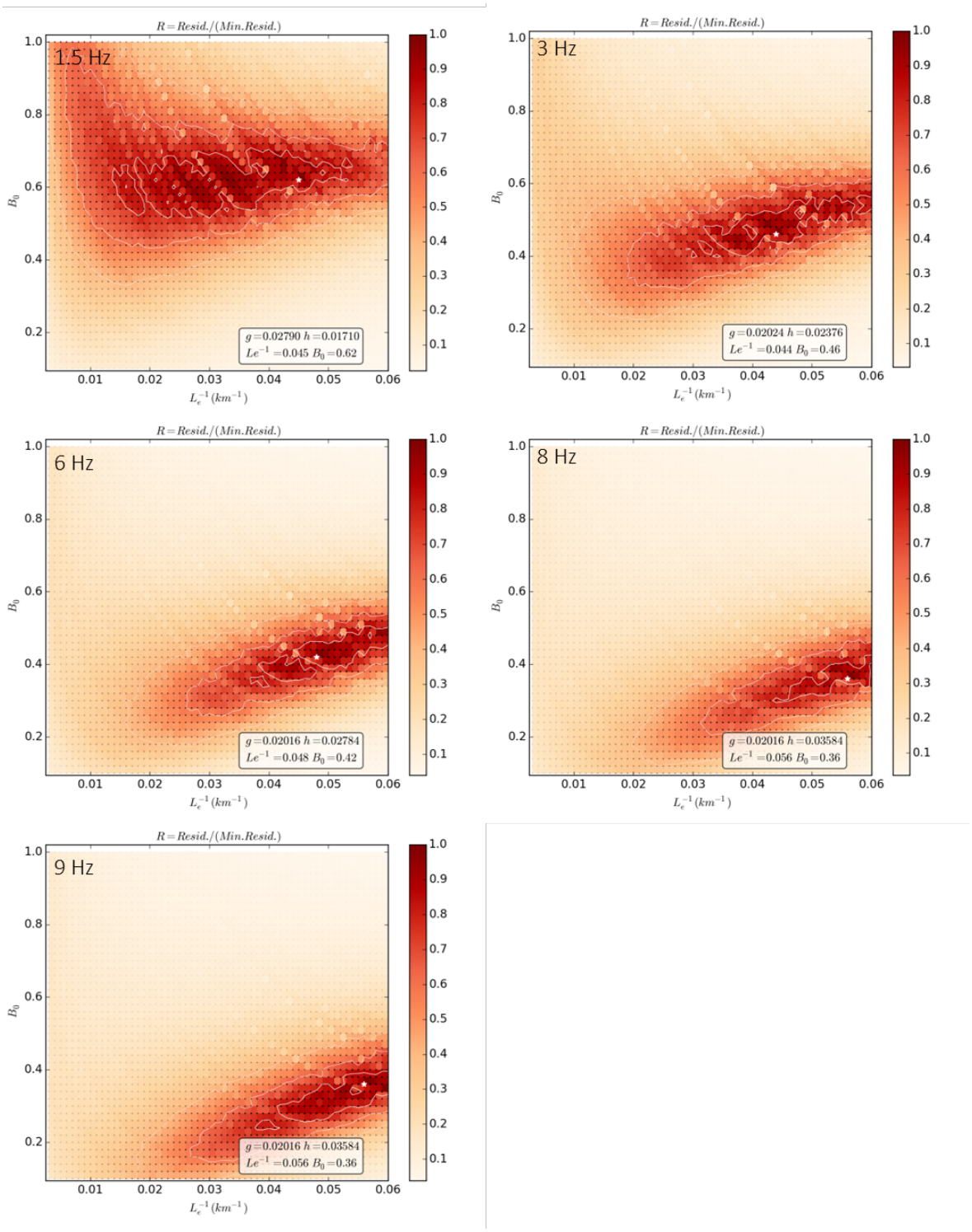

Figure 3.26. Residual maps of best fitting process of SULT station for each center frequency is shown. Colors vary according to normalized residual value. The white star shows the best pair that fits the observed data.

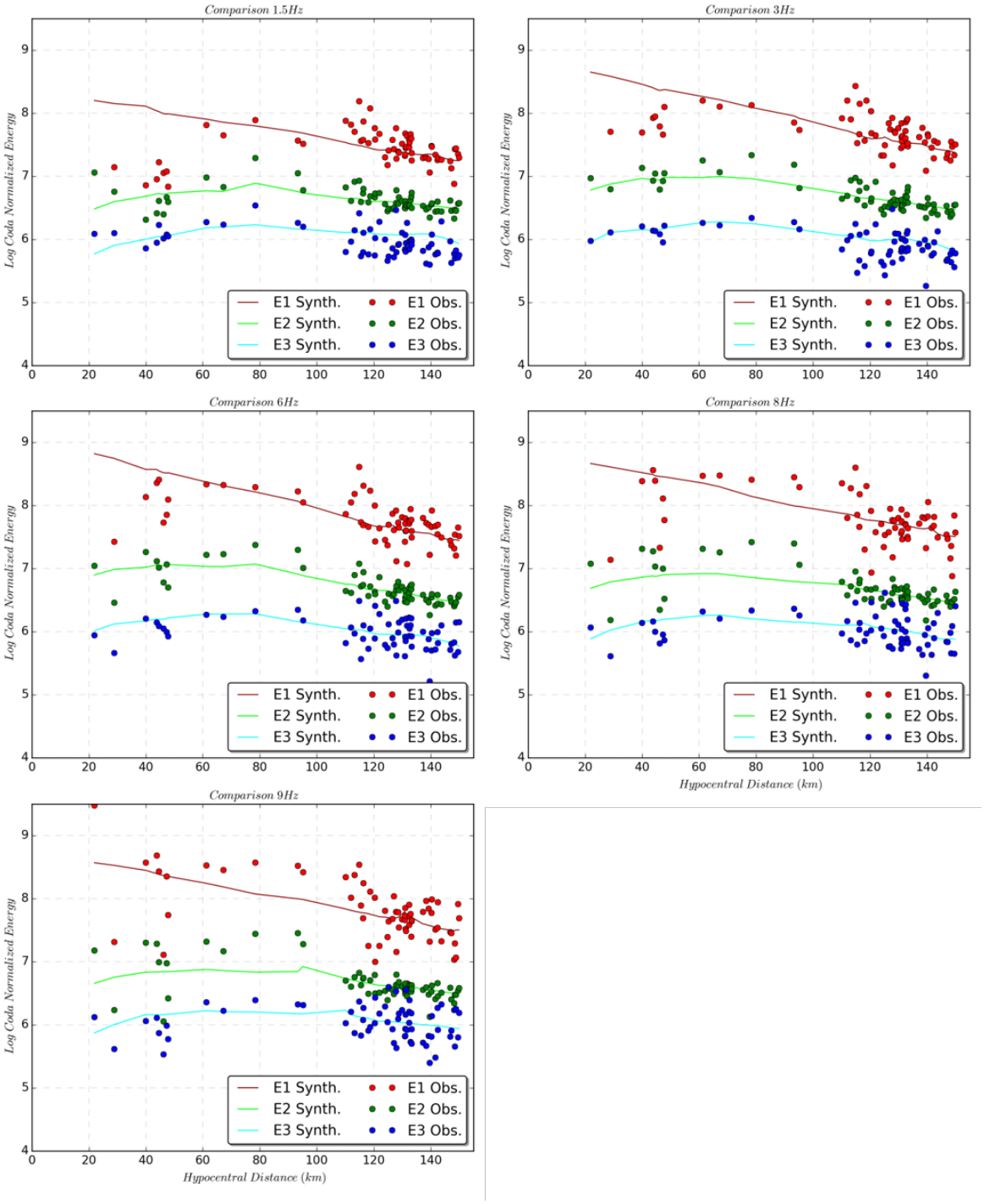

Figure 3.27. Comparison of observed energy density(circles) and the synthetic energy curves given by the best pair of L_e^{-1} and B_0 versus hypocentral distance for SVRH station. Colors represents each time-windows.

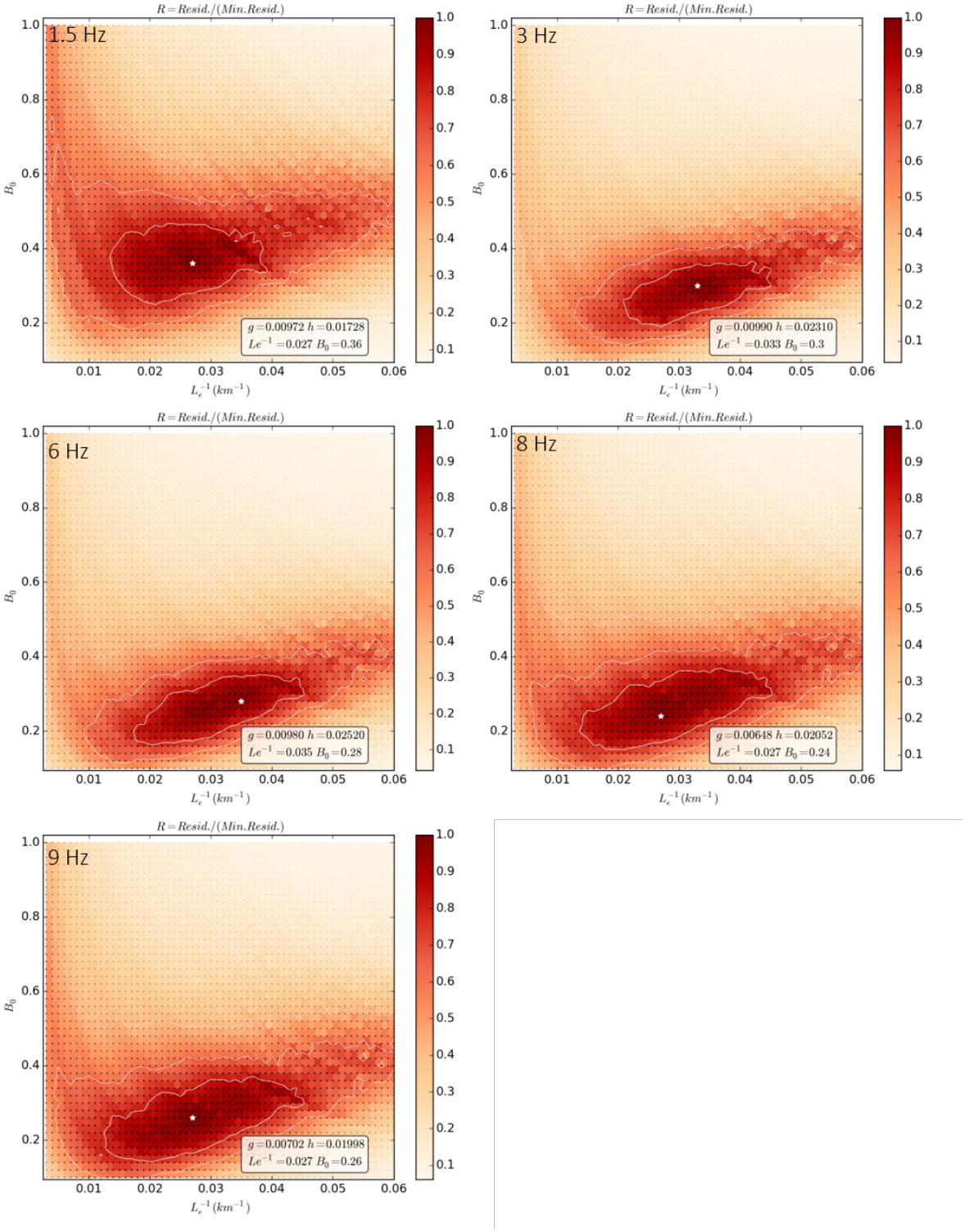

Figure 3.28. Residual maps of best fitting process of SVRH station for each center frequency is shown. Colors vary according to normalized residual value. The white star shows the best pair that fits the observed data.

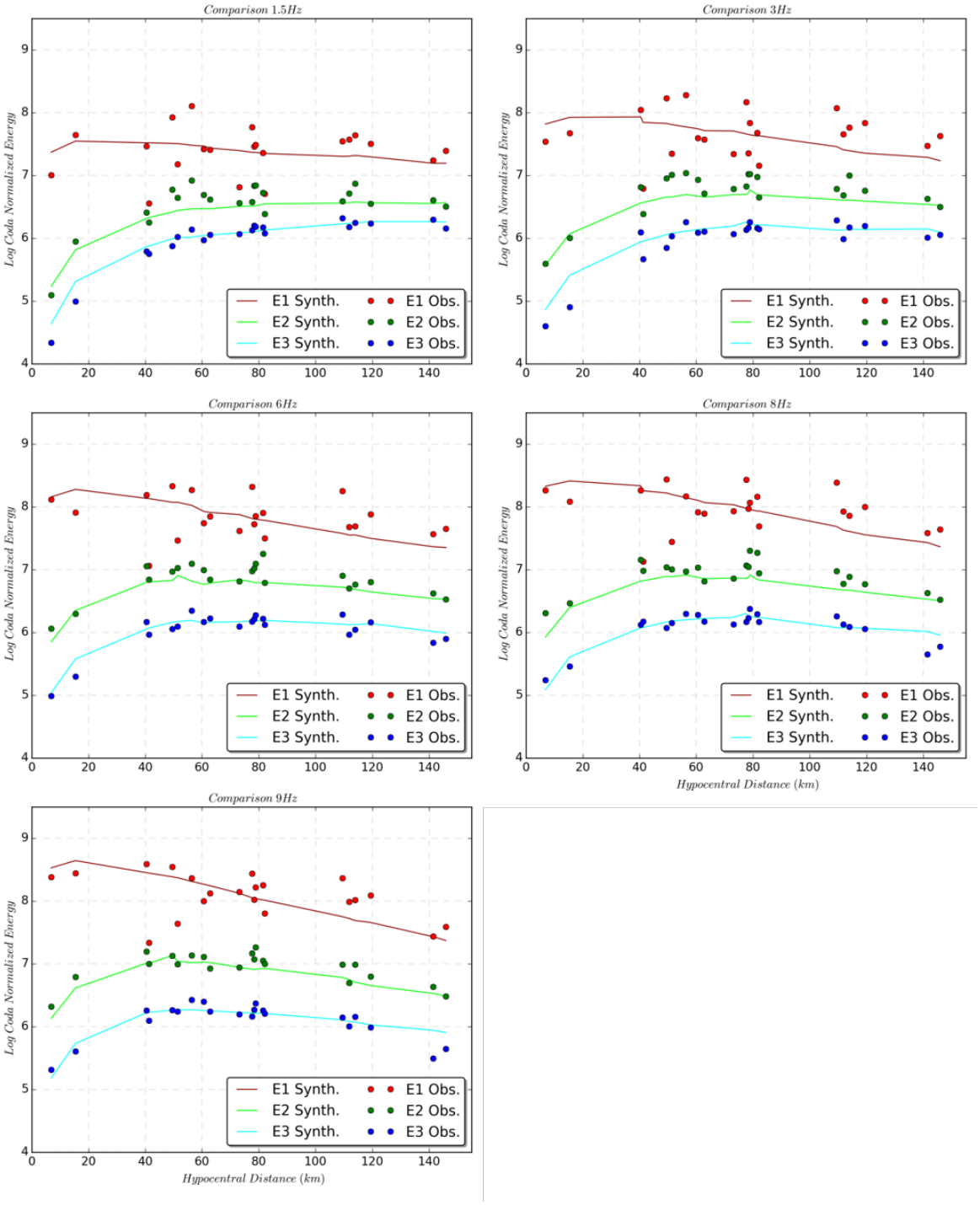

Figure 3.29. Comparison of observed energy density(circles) and the synthetic energy curves given by the best pair of L_e^{-1} and B_0 versus hypocentral distance for YAYX station. Colors represents each time-windows.

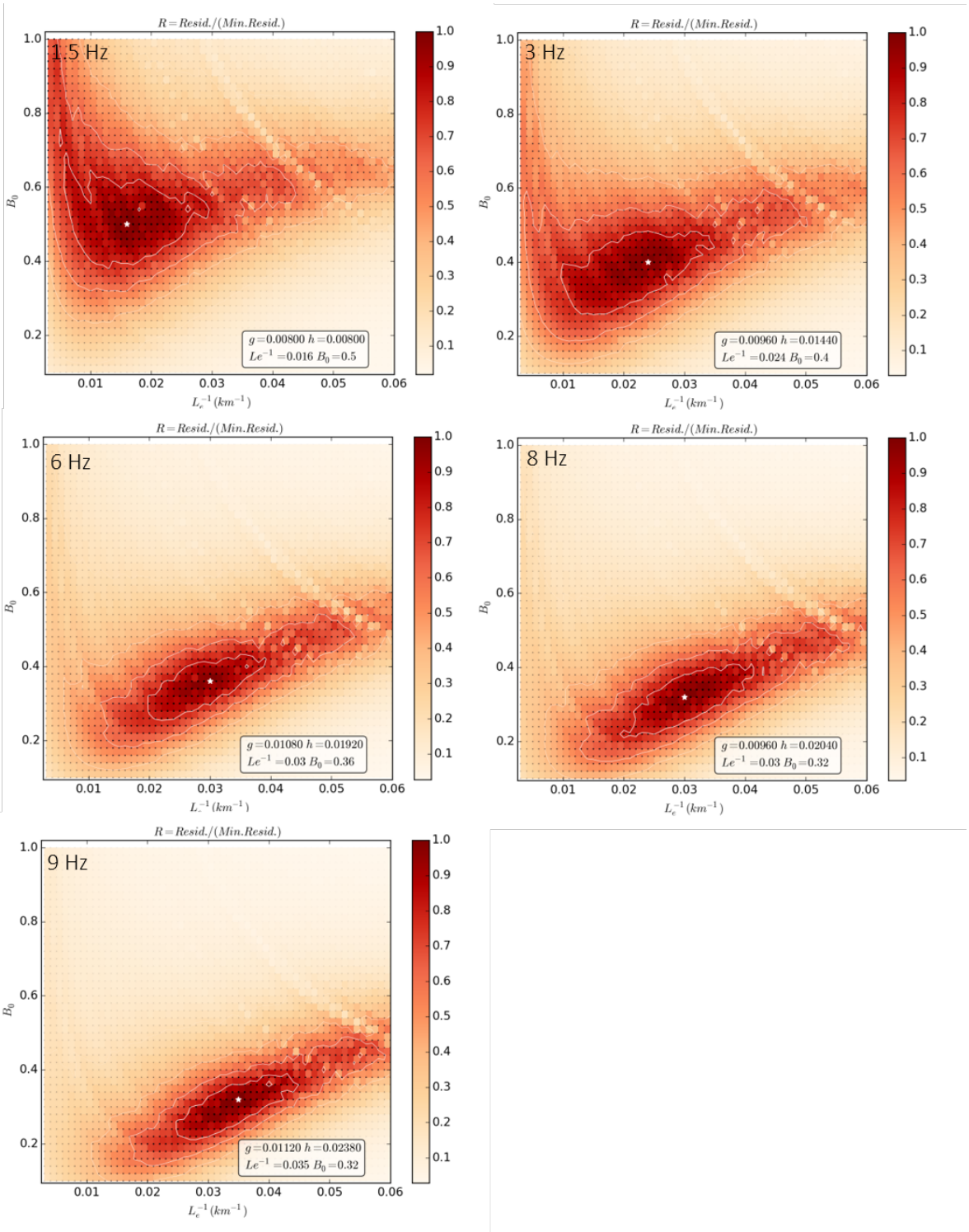

Figure 3.30. Residual maps of best fitting process of YAYX station for each center frequency is shown. Colors vary according to normalized residual value. The white star shows the best pair that fits the observed data.

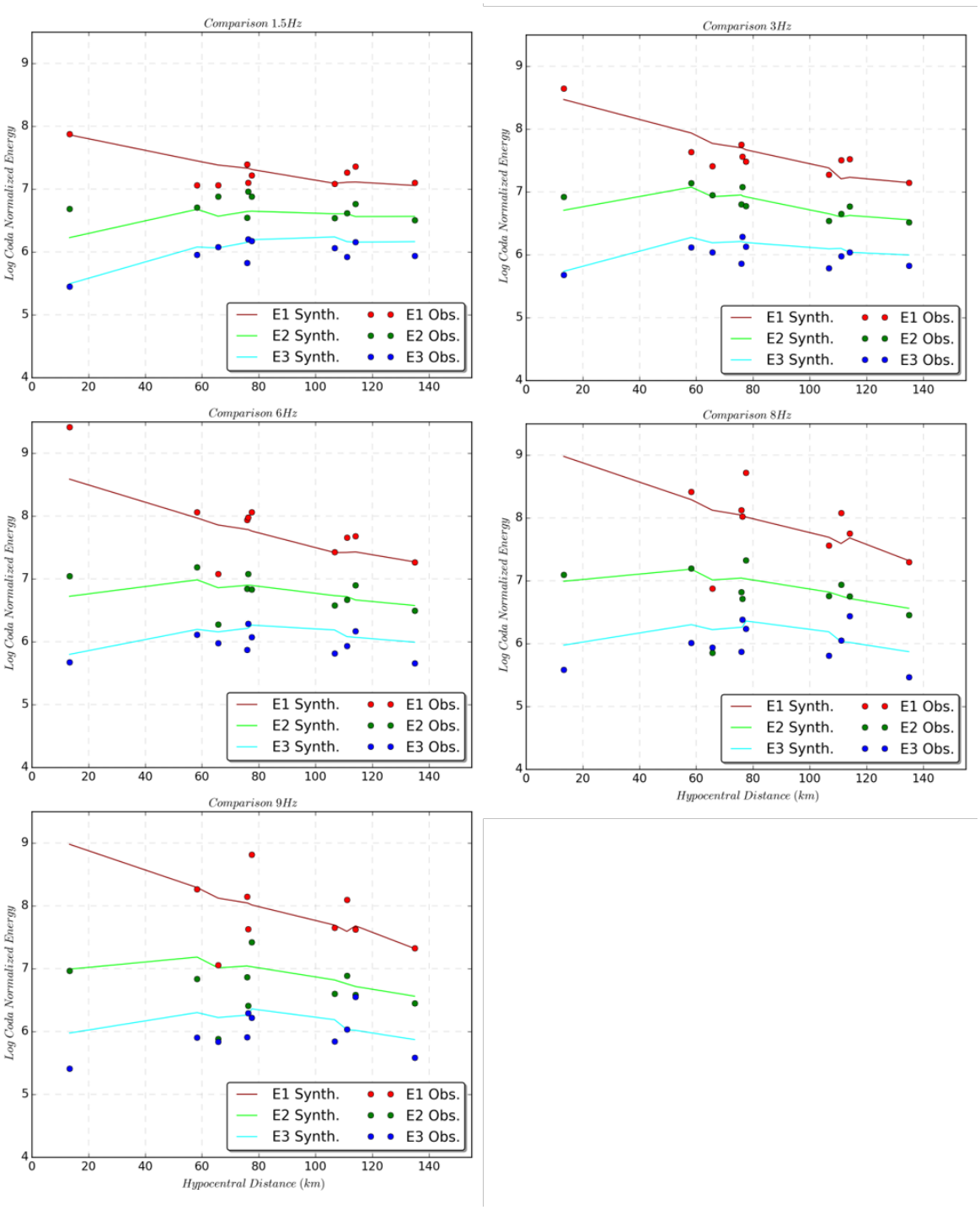

Figure 3.31. Comparison of observed energy density(circles) and the synthetic energy curves given by the best pair of L_e^{-1} and B_0 versus hypocentral distance for YESY station. Colors represents each time-windows.

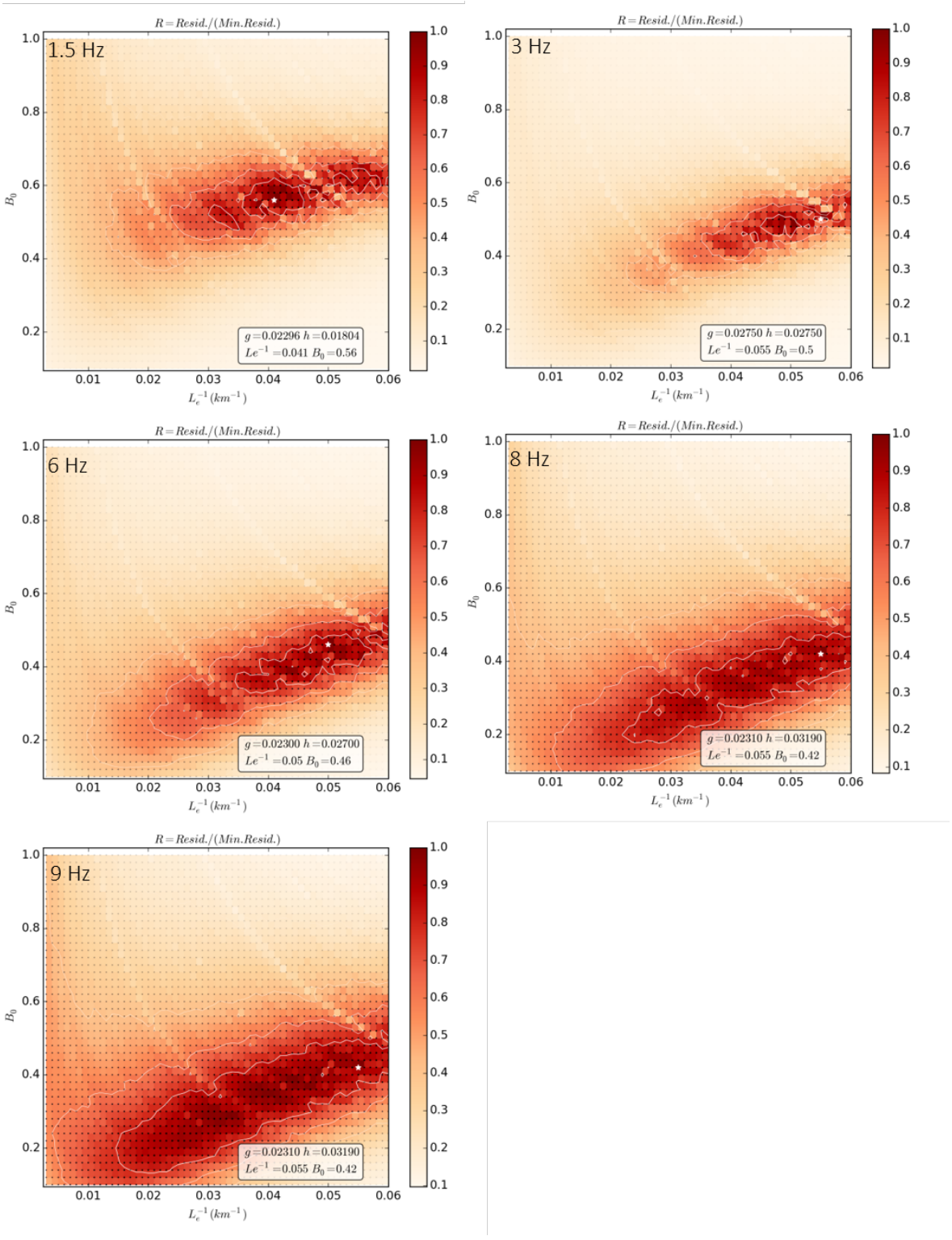

Figure 3.32. Residual maps of best fitting process of YESY station for each center frequency is shown. Colors vary according to normalized residual value. The white star shows the best pair that fits the observed data.

3.2. Final Attenuations

3.2.1. Individual attenuation estimates

Estimations of attenuation values Q_t^{-1}, Q_s^{-1}, and Q_i^{-1} are calculated using respective Equations 2.5 from the best pair of B_0 and L_e^{-1} values at each station for frequencies 1.5, 3, 6, 8, and 9 Hz. Calculated scattering and intrinsic attenuation values are visualized against frequency in Figure 3.33 and the exact values are tabulated for each centre frequency in Table 3.2, Table 3.3, Table 3.4, Table 3.5, and Table 3.6.

Using single stations for attenuation calculations allows us to assess lateral variations in attenuation structure, consequently providing better insight into the tectonics of the region. A regional average is also calculated for Central Anatolia as the dominant mechanism does not vary from region to region.

The general trend observed in Figure 3.33 is that the intrinsic attenuation is the main mechanism effecting the seismic wave amplitudes within Central Anatolia and both attenuation mechanisms decrease with increasing frequency. There are a few sites where both of the attenuation mechanisms are close to each other in terms of effectiveness such as YESY, SERE, and SULT. Scattering becomes notable for almost all stations for frequencies lower than 3 Hz and in fact, it surpasses intrinsic absorption at stations AFSR, SULT, SERE, and YESY. Array BB stations BR131 and BR231 have similar attenuation behavior albeit scattering is a little bit higher at BR231. The lowest level of total attenuation is observed at stations LOD and BNN depending on the frequency. At 1.5 Hz BNN station has the second-high attenuation following the AFSR but loses attenuation power rapidly with higher frequencies. YESY and SULT stations have highest total attenuations in all frequency ranges except 1.5 Hz.

3.2.2. Average attenuation estimates

I have also calculated the average of intrinsic, scattering, and total attenuations for Central Anatolia region and shown the results in Figure 3.34 and Table 3.7. Average

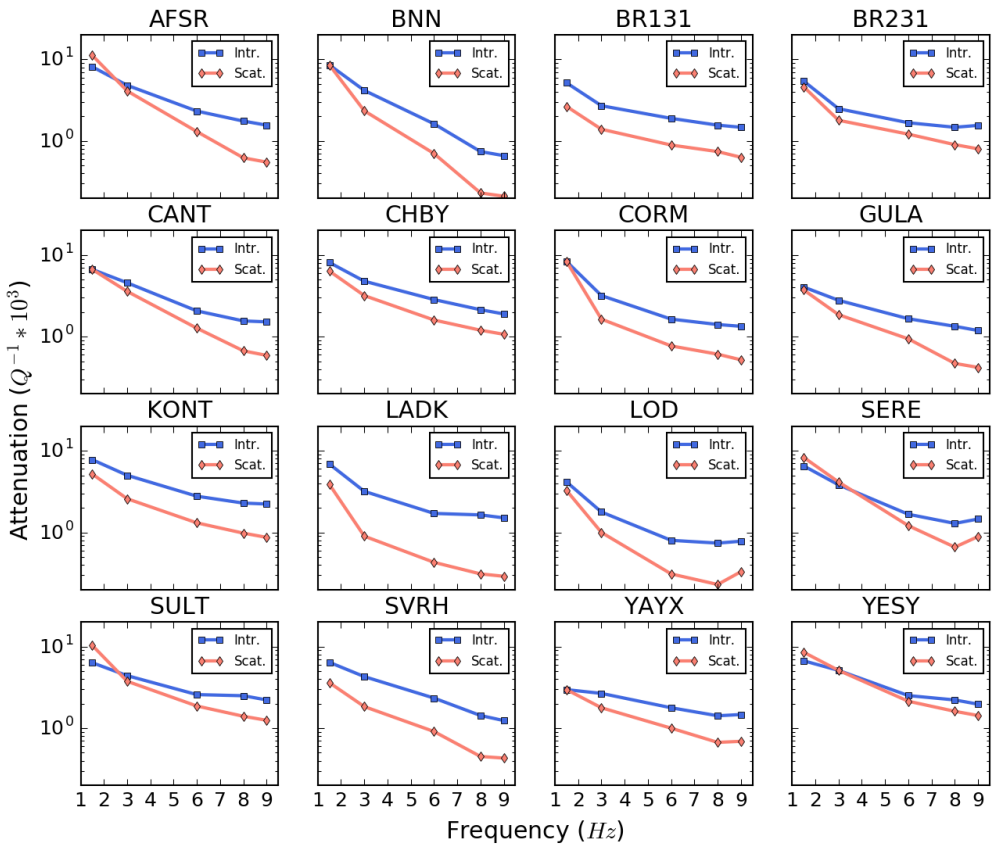

Figure 3.33. Attenuation mechanisms versus frequency at each site. Blue lines represent Intrinsic attenuation whereas pink ones denote scattering attenuation. It is obvious that the intrinsic absorption is the dominant attenuation factor in the Central Anatolia region.

Table 3.2. Best fitting parameters and corresponding attenuation values at 1.5 Hz frequency.

Station	L_e^{-1}	B_0	$Q_i^{-1}(10^3)$	$Q_s^{-1}(10^3)$	$Q_t^{-1}(10^3)$
AFSR	0.052 (0.008,-0.01)	0.58 (0.04,-0.08)	7.42	10.24	17.66
BNN	0.046 (0.003,-0.009)	0.5 (0.02,-0.08)	7.81	7.81	15.62
BR131	0.021 (0.009,-0.003)	0.34 (0.08,-0.02)	4.71	2.42	7.13
BR231	0.027 (0.01,-0.006)	0.46 (0.08,-0.04)	4.95	4.22	9.17
CANT	0.036 (0.012,-0.006)	0.5 (0.06,-0.04)	6.11	6.11	12.22
CHBY	0.039 (0.002,-0.003)	0.44 (0.04,-0.02)	7.42	5.83	13.25
CORM	0.045 (-0.021)	0.5 (0.01,-0.12)	7.64	7.64	15.28
GULA	0.021 (0.017,-0.006)	0.48 (0.08,-0.06)	3.71	3.42	7.13
KONT	0.035 (0.002)	0.4 (-0.02)	7.13	4.75	11.88
LADK	0.029 (0.003,-0.008)	0.36 (0.02,-0.08)	6.3	3.54	9.84
LOD	0.02 (0.002,-0.009)	0.44 (0.02,-0.08)	3.8	2.99	6.79
SERE	0.04 (0.005,-0.005)	0.56 (0.06)	5.98	7.61	13.59
SULT	0.045 (0.002,-0.022)	0.62 (0.06,-0.06)	5.81	9.47	15.28
SVRH	0.027 (0.01,-0.009)	0.36 (0.06,-0.04)	5.87	3.3	9.17
YAYX	0.016 (0.007,-0.004)	0.5 (0.06,-0.08)	2.72	2.72	5.44
YESY	0.041 (0.017,-0.009)	0.56 (0.1,-006)	6.13	7.8	13.93

attenuations also indicate that the intrinsic attenuation is dominant for all frequencies in this region. Estimating the frequency dependency of attenuation structure in the form of $Q_0^{-1} * f^{-n}$, observations indicate that the scattering has higher dependency rate as evident from power-law fitting of its slope with $n = 1.24$, whereas total attenuation has $n = 0.99$, and finally 0.83 for intrinsic absorption. It is observed that the intrinsic attenuation is less frequency dependent compared to scattering attenuation. The reason for the high frequency dependence of scattering could be related to the size of the heterogeneities as mentioned by Akinci and Eyidoğan [13] as they have found very high frequency dependence for Q_s^{-1} in Erzincan region. Finally, average estimates of Q_t^{-1}, Q_s^{-1}, and Q_i^{-1} for Central Anatolia are compared with results from other regions around the world in Figure 3.35.

Table 3.3. Best fitting parameters and corresponding attenuation values at 3 Hz frequency.

Station	L_e^{-1}	B_0	$Q_i^{-1}(10^3)$	$Q_s^{-1}(10^3)$	$Q_t^{-1}(10^3)$
AFSR	0.048 (0.012,-0.012)	0.46 (0.1,-0.08)	4.4	3.75	8.15
BNN	0.035 (0.017,-0.008)	0.36 (0.12,-0.08)	3.8	2.14	5.94
BR131	0.022 (0.008,-0.0039	0.34 (0.06,-0.04)	2.46	1.27	3.73
BR231	0.023 (0.007,-0.005)	0.42 (0.06,-0.04)	2.26	1.64	3.9
CANT	0.044 (0.006,-0.006)	0.44 (0.02,-0.02)	4.18	3.29	7.47
CHBY	0.043 (-0.002)	0.4 (0.02)	4.38	2.92	7.3
CORM	0.026 (0.013,-0.005)	0.34 (0.08,-0.02)	2.91	1.5	4.41
GULA	0.025 (0.003,-0.006)	0.4 (0.02,-0.08)	2.55	1.7	4.25
KONT	0.041 (-0.002)	0.34 (0.02)	4.59	2.37	6.96
LADK	0.022 (0.011,-0.003)	0.22 (0.1,-0.02)	2.91	0.82	3.73
LOD	0.015 (0.003,-0.007)	0.36 (0.06,-0.08)	1.63	0.92	2.55
SERE	0.043 (0.002,-0.016)	0.52 (0.02,-0.1)	3.5	3.8	7.3
SULT	0.044 (0.012,-0.009)	0.46 (0.08,-0.04)	4.03	3.44	7.47
SVRH	0.033 (0.008,-0.007)	0.3 (0.02,-0.06)	3.92	1.68	5.6
YAYX	0.024 (0.005,-0.009)	0.4 (0.04,-0.08)	2.44	1.63	4.07
YESY	0.055 (0.004,-0.013)	0.5 (0.04,-0.06)	4.67	4.67	9.34

Table 3.4. Best fitting parameters and corresponding attenuation values at 6 Hz frequency.

Station	L_e^{-1}	B_0	$Q_i^{-1}(10^3)$	$Q_s^{-1}(10^3)$	$Q_t^{-1}(10^3)$
AFSR	0.039 (0.015,-0.014)	0.36 (0.1,-0.14)	2.12	1.19	3.31
BNN	0.025 (0.008,-0.012)	0.3 (0.12,-0.1)	1.49	0.64	2.13
BR131	0.03 (0.003,-0.007)	0.32 (0.04,-0.04)	1.73	0.81	2.54
BR231	0.031 (-0.014)	0.42 (0.04,-0.06)	1.53	1.11	2.64
CANT	0.036 (0.009,-0.009)	0.38 (0.06,-0.08)	1.89	1.16	3.05
CHBY	0.048 (0.011,-0.014)	0.36 (0.1,-0.06)	2.61	1.47	4.08
CORM	0.026 (0.015,-0.002)	0.32 (0.08,-0.02)	1.5	0.71	2.21
GULA	0.028 (0.001,-0.007)	0.36 (-0.1)	1.52	0.86	2.38
KONT	0.044 (-0.007)	0.32 (0.02,-0.04)	2.54	1.2	3.74
LADK	0.023 (0.009,-0.004)	0.2 (0.06,-0.04)	1.56	0.39	1.95
LOD	0.012 (0.007,-0.003)	0.28 (0.08,- 0.02)	0.73	0.29	1.02
SERE	0.031 (0.013,-0.007)	0.42 (0.06,-0.04)	1.53	1.11	2.64
SULT	0.048 (0.011,-0.005)	0.42 (0.06,-0.04)	2.36	1.71	4.07
SVRH	0.035 (0.008,-0.013)	0.28 (0.04,-0.06)	2.14	0.83	2.97
YAYX	0.03 (0.002,-0.006)	0.36 (0.02,-0.06)	1.63	0.92	2.55
YESY	0.05 (0.01,-0.014)	0.46 (0.04,-0.12)	2.29	1.95	4.24

Table 3.5. Best fitting parameters and corresponding attenuation values at 8 Hz frequency.

Station	L_e^{-1}	B_0	$Q_i^{-1}(10^3)$	$Q_s^{-1}(10^3)$	$Q_t^{-1}(10^3)$
AFSR	0.034 (0.019,-0.013)	0.26 (0.18,-0.12)	1.6	0.56	2.16
BNN	0.014 (0.013,-0.007)	0.24 (0.16,-0.06)	0.68	0.21	0.89
BR131	0.033 (0.006,-0.006)	0.32 (0.02,-0.06)	1.43	0.67	2.1
BR231	0.034 (0.002,-0.012)	0.38 (-0.1)	1.34	0.82	2.16
CANT	0.032 (0.002,-0.002)	0.3 (0.02,-0.02)	1.43	0.61	2.04
CHBY	0.048 (0.003,-0.024)	0.36 (0.02,-0.16)	1.96	1.1	3.06
CORM	0.029 (0.014,-0.003)	0.3 (0.08,-0.04)	1.29	0.55	1.84
GULA	0.026 (0.007,-0.011)	0.26 (0.08,-0.1)	1.22	0.43	1.65
KONT	0.047 (0.003,-0.012)	0.3 (0.02,-0.1)	2.09	0.9	2.99
LADK	0.028 (0.004,-0.009)	0.16 (0.06,-0.04)	1.5	0.29	1.79
LOD	0.014 (0.007,-0.003)	0.24 (0.08,-0.04)	0.68	0.21	0.89
SERE	0.028 (0.01,-0.004)	0.34 (0.06,-0.04)	1.18	0.61	1.79
SULT	0.056 (0.001,-0.004)	0.32 (0.02,-0.02)	2.28	1.28	3.56
SVRH	0.027 (0.014,-0.009)	0.24 (0.1,-0.04)	1.31	0.41	1.72
YAYX	0.03 (0.007,-0.004)	0.32 (0.04,-0.04)	1.3	0.61	1.91
YESY	0.055 (0.005,-0.030)	0.42 (0.04,-0.22)	2.03	1.47	3.5

Table 3.6. Best fitting parameters and corresponding attenuation values at 9 Hz frequency.

Station	L_e^{-1}	B_0	$Q_i^{-1}(10^3)$	$Q_s^{-1}(10^3)$	$Q_t^{-1}(10^3)$
AFSR	0,034 (0.026, -0.013)	0,26 (0.2, -0.14)	1.42	0.5	1.92
BNN	0,014 (0.015, -0.004)	0,24 (0.16, -0.06)	0.6	0.19	0.79
BR131	0,034 (0.006, -0.002)	0,3 (0.04, -0.02)	1.35	0.58	1.93
BR231	0.038 (-0.13)	0.34 (0.02, -0.1)	1.42	0.73	2.15
CANT	0.034 (0.014, -0.003)	0.28 (0.08, -0.04)	1.39	0.54	1.93
CHBY	0.048 (0.006, -0.047)	0.36 (-0.2)	1.74	0.98	2.72
CORM	0.03 (0.023, -0.003)	0.28 (0.16, -0.02)	1.22	0.48	1.7
GULA	0.026 (0.009, -0.008)	0.26 (0.08, -0.08)	1.09	0.38	1.47
KONT	0.05 (-0.015)	0.28 (0.04, -0.08)	2.04	0.79	2.83
LADK	0.029 (0.009, -0.006)	0.16 (0.06, -0.06)	1.38	0.26	1.64
LOD	0.018 (0.007, -0.007)	0.3 (0.06, -0.1)	0.71	0.31	1.02
SERE	0.038 (-0.012)	0.38 (0.02, -0.08)	1.33	0.82	2.15
SULT	0.056 (0.003, -0.006)	0.36 (-0.06)	2.03	1.14	3.17
SVRH	0.027 (0.017, -0.01)	0.26 (0.08, -0.08)	1.13	0.4	1.53
YAYX	0.035 (0.007, -0.006)	0.32 (0.04, -0.06)	1.35	0.63	1.98
YESY	0.055 (0.005, -0.038)	0.42 (0.08, -0.22)	1.81	1.31	3.12

Table 3.7. Variation of average scattering and intrinsic attenuation values and Standard deviations (SD) with respect to frequency.

Frequency (Hz)	$Q_s^{-1}(SD)$	$Q_i^{-1}(SD)$	$Q_t^{-1}(SD)$
1.5	5.61 (±2.46)	5.84 (±1.47)	11.46 (±3.61)
3.0	2.34 (±1.12)	3.41 (±0.93)	5.76 (±1.93)
6.0	1.02 (± 0.43)	1.82 (±0.48)	2.85 (±0.85)
8.0	0.67 (± 0.35)	1.45 (±0.44)	2.13 (±0.77)
9.0	0.62 (± 0.31)	1.37 (±0.39)	2.00 (±0.66)

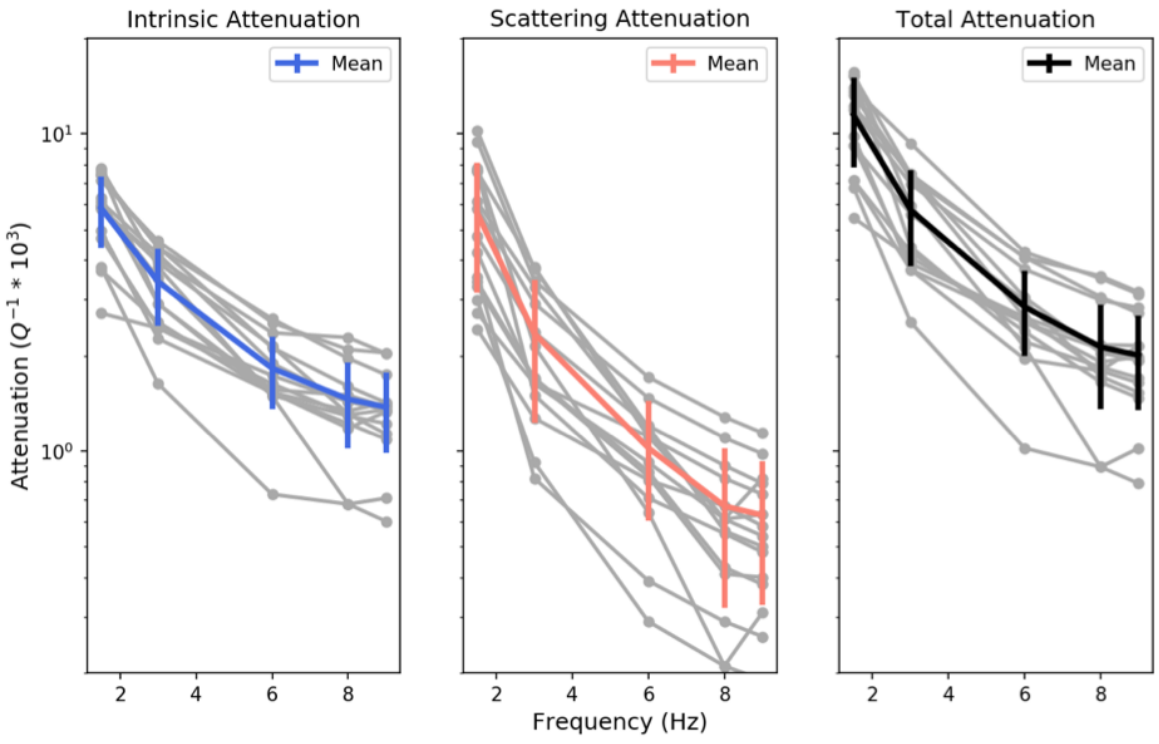

Figure 3.34. Average intrinsic (left), scattering (middle), and total (right) attenuation of Central Anatolia region is given in the figure. Frequency dependencies are also shown on each figure.

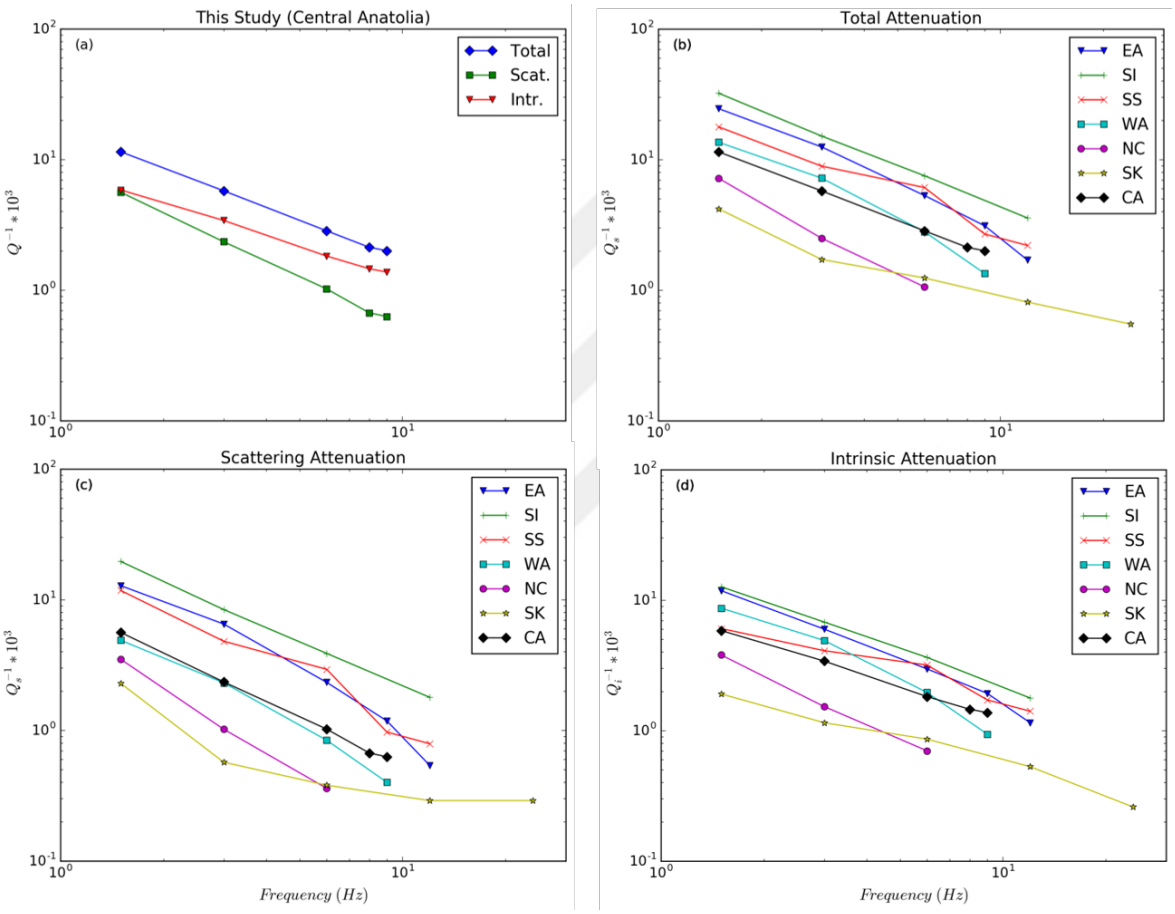

Figure 3.35. Comparison of results from this study and the other regions. On (a), average attenuation values of Central Anatolia is shown. (b), (c), and (d) figures compares the total, scattering, and intrinsic attenuation of this study to other researches conducted at different regions.

4. DISCUSSION AND CONCLUSION

I have analyzed the attenuation structure of Central Anatolia in the scope of Bala earthquake sequence using the high-quality array data and KOERI stations. The single station approach of the Multiple Lapse Time Window (MLTW) method was applied to the seismic data to find the best pair of L_e^{-1} and B_0 at hypocentral distances between 5-150 km for center frequencies of 1.5, 3, 6, 8, 9 Hz using the Monte Carlo simulation code of Hoshiba [49]. Due to sampling rate constraints, data from short period vertical and medium period array stations were not used in the study. Total attenuation structure around the stations were obtained and separated into the components of scattering and intrinsic absorption to better understand the underlying mechanisms that define the tectonics and the seismicity of the region. There have been many studies of regional attenuation around the world in addition to many velocity determinations using a wide array of methods. The order of the variety for attenuation is usually higher than velocity changes depending on the medium. Therefore, attenuation is very sensitive to the type of heterogeneities in the lithosphere.

Overall, the results of the analysis show that the region is characterized by high intrinsic attenuation. As shown in Figure 3.33, the total attenuation decreases with increasing frequency, as is the case for many regions studied by other researchers. Highest scattering attenuation is observed in the middle of the Central Anatolia along the Tuz Gölü fault zone in the NW-SE direction at stations AFSR, SULT, SERE, and YESY for frequencies 1.5 Hz and 3 Hz. This result is also compatible with the increased tectonic activity observed in the northern part of this area (Afşar fault zone) following the recent 2005 and 2007 mid-sized earthquakes and their aftershocks. High scattering associated with fault zones and active tectonics is also reported by previous studies in other regions around the world. The western part of Central Anatolian block is dominated by intrinsic attenuation for all the frequencies investigated. However, since there is only one station (SVRH) in this area and it has abnormalities in its first energy-density window (E1) for near hypocentral distances (Figure 3.27), this estimate might not be reliable. The north – northeast section of the Central Anatolia near

Ankara, Çankırı, and Çorum provinces shows dominant intrinsic absorption compared to scattering for frequencies higher than 1.5 Hz. Total attenuation is also lower than the southern areas. BR131, BR231, CORM, and CANT stations have stable low frequency dependence of intrinsic attenuation. The areas covering the middle of the Kırşehir Massiff are tectonically stable as inferred from low seismicity of the region and defined by low attenuation values. In this study, this area is characterized by predominant intrinsic attenuation. The south - southeastern area of Central Anatolia displays the highest total attenuation for frequencies higher than 1.5 Hz. In general, analestic absorption is again the type of attenuation mechanism effecting the seismic wave amplitudes. The southwestern part of Central Anatolian block, which is the boundary by the Isparta angle, also exhibits strong intrinsic absorption.

As mentioned in the introduction, merging seismic velocity and attenuation studies could shed better light into the tectonics of the region. In fact, there have been many recent seismic velocity studies conducted in Anatolia, Turkey, especially for eastern Anatolia ([31–33, 57–59]). Most of these studies investigate the Pn velocity variation within the mantle except Gök et al. [31] in which they mapped Sn attenuation with tomography for Anatolian and Iranian plateau and concluded that the Sn phase is highly attenuated for eastern and central Anatolia caused by the lack of lithospheric mantle beneath the Anatolian plateau. They also argued that the lack of Sn most likely is the result of intrinsic absorption in the upper mantle caused by partial melting according to low Pn velocities within the mantle. Low Pn velocities across the Anatolian plateau are also observed by other authors; Al-Lazki et al. [57] using a tomography method obtained low Pn velocities under the Anatolian plateau. Similarly, Mutlu and Karabulut [33] found a significant low velocity zone beneath the crust along the Central Anatolian Volcanic Zone, an area in which Quaternary volcanism plays an important role. In summary, seismic velocity studies in this region agrees that the Neogene Quaternary volcanism affects the seismic velocities due to very thin lithospheric mantle underneath the South-Southeast Central Anatolia. The observations that has been found in this study coincides well with the previous seismic studies in this region. Higher intrinsic attenuation is most likely related to the high heat flow beneath the region.

There have been many applications of the MLTW method to estimate the relative contributions of scattering and anelastic attenuations in various regions around the world. Akinci et al., [9], applied this technique to Southern Spain and Western Anatolia and they concluded that scattering is dominant over intrinsic absorption for frequencies lower than 4 Hz. Whereas they had unreliable fit of data for hypocentral distances between 0-80 km for Western Anatolia however, for greater distances they obtained better results indicating stronger intrinsic absorption. The Erzincan basin of eastern Anatolia is also investigated using the MLTW method in the study of Akinci and Eyidoğan [13]. They have obtained comparable results to this study as the scattering and intrinsic attenuation is similar for frequencies 3 Hz and lower, while intrinsic attenuation becomes dominant for 6 Hz and higher frequencies. They have pointed out the very high Q_s^{-1} frequency dependence with $f^{1.48}$. Hoshiba et al. [14] employed MLTW analysis to investigate the attenuation structure in northern Chile with both a uniform and depth dependent velocity structure using appropriate model parameters and sub-crustal earthquakes. He concluded that the uniform and depth dependent models result in higher intrinsic attenuation than scattering but not by a big margin. He pointed out the importance of velocity selection for the simulation. Southern Italy has been studied by (Tuvè et al. [17]) in center frequencies of 1.5, 3, 6, and 12 Hz using coda Q_c^{-1} and MLTW methods. They have found that for frequencies higher than 3 Hz both types of attenuations are at the same level and in the case of lower frequencies, scattering predominates the region. Another study carried out in Asia performed by Chung et al., [60] have separated Q_s^{-1} and Q_i^{-1} for South Korea. They also employed both a depth-dependent velocity model along with a uniform model to estimate the attenuation structure. According to the results, South Korea region has one of the lowest attenuation estimates in comparison to other regions caused most likely by the lack of seismic activity.

I have compared the results for Central Anatolia to other regions that employed the same method to infer the attenuation mechanism. The comparison is shown in Figure 3.35, starting with the total, scattering, and intrinsic attenuation obtained in this study in the upper left figure (a), The total and scattering attenuation resemble each other in terms of frequency dependence. Intrinsic absorption is higher than

scattering and less dependent on the frequency for all frequencies investigated. I have put together the results from different regions in Figure 3.35b and compared the total attenuation level with this study. Central Anatolia is situated in the middle of attenuation scale among the other regions. Southern Italy followed by Eastern Anatolia has the highest degree of attenuation. Central Anatolia has a similar level of total attenuation to Western Anatolia. The comparison reveals that northern Chile and South Korea have lower attenuation than other regions including Central Anatolia. Scattering attenuation variation between these regions is shown in Figure 3.35c. The trend is almost the same as the total attenuation. However, Central Anatolia has slightly higher scattering attenuation compared to Western Anatolia. Lastly, intrinsic attenuation variation for several regions is displayed in Figure 3.35. The values of intrinsic absorption are closer to each other except northern Chile and South Korea. Central Anatolia has lower Q_i^{-1} for frequencies lower than 6 Hz compare to Western Anatolia. Southern Italy and Eastern Anatolia have the highest Q_i^{-1} among the regions. There are other studies in different regions that can be compared.

This study attempted to distinguish the Q_s^{-1} and Q_i^{-1} contributions at Central Anatolia for frequencies of 1.5, 3, 6, 8, 9 Hz. The results showed that the intrinsic attenuation is stronger and supported by the previous work done with different approaches. Detailed attenuation structure determination is important for many applications. One of the important uses of accurate attenuation measurements is the discrimination of explosions and earthquakes since many regional discriminants (such as P/S ratio and mb/Ms) rely on the amplitude measurements and their corrections [61].

REFERENCES

1. Tan, O., M. C. Tapırdamaz, S. Ergintav, S. İnan, Y. İravul, R. Saatçılar, B. Tüzel, A. Tarancıoğlu, S. Karakısa, R. F. Kartal, S. Zünbül, K. Yanık, M. Kaplan, F. Şaroğlu, A. Koçyiğit, E. Altunel and N. M. Özel, "Turkish journal of earth sciences.", *Turkish Journal of Earth Sciences*, Vol. 19, No. 4, pp. 449–471, nov 2010.

2. Sipkin, S. and T. Jordan, "Frequency dependence of QScS", *Bulletin of the Seismological Society of America*, Vol. 69, No. 4, pp. 1055–1079, 1979.

3. Schubert, G., *Treatise on Geophysics*, Elsevier Science, 2015.

4. Sato, H., M. C. Fehler and T. Maeda, *Seismic Wave Propagation and Scattering in the Heterogeneous Earth: Second Edition*, Springer-Verlag, 2012.

5. Fehler, M., M. Hoshiba, H. Sato and K. Obara, "Separation of scattering and intrinsic attenuation for the Kanto-Tokai region, Japan, using measurements of S-wave energy versus hypocentral distance", *Geophysical Journal International*, Vol. 108, No. 3, pp. 787–800, 1992.

6. Hoshiba, M., "Separation of scattering attenuation and intrinsic absorption in Japan using the multiple lapse time window analysis of full seismogram envelope", , 1993.

7. Mayeda, K., S. Koyanagi, M. Hoshiba, K. Aki and Y. Zeng, "A comparative study of scattering, intrinsic, and coda Q -1 for Hawaii, Long Valley, and central California between 1.5 and 15.0 Hz", *Journal of Geophysical Research*, Vol. 97, No. B5, p. 6643, may 1992.

8. Jin, A., K. Mayeda, D. Adams and K. Aki, "Separation of intrinsic and scattering attenuation in southern California using TERRAscope data", *Journal of Geophys-*

ical Research: Solid Earth, Vol. 99, No. B9, pp. 17835–17848, sep 1994.

9. Akinci, A., E. Pezzo and J. M. Ibáñez, "Separation of scattering and intrinsic attenuation in southern Spain and western Anatolia (Turkey)", *Geophysical Journal International*, Vol. 121, No. 2, pp. 337–353, may 1995.

10. Pujades, L. G., A. Ugalde, J. A. Canas, M. Navarro, F. J. Badal and V. Corchete, "Intrinsic and scattering attenuation from observed seismic codas in the Almeria Basin (southeastern Iberian Peninsula)", *Geophysical Journal International*, Vol. 129, No. 2, pp. 281–291, may 1997.

11. Canas, J. A., A. Ugalde, L. G. Pujades, J. C. Carracedo, V. Soler and M. J. Blanco, "Intrinsic and scattering seismic wave attenuation in the Canary Islands", *Journal of Geophysical Research: Solid Earth*, Vol. 103, No. B7, pp. 15037–15050, jul 1998.

12. Ugalde, A., L. G. Pujades, J. A. Canas and A. Villaseñor, "Estimation of the Intrinsic Absorption and Scattering Attenuation in Northeastern Venezuela (Southeastern Caribbean) Using Coda Waves", *Pure and Applied Geophysics*, Vol. 153, No. 2-4, pp. 685–702, dec 1998.

13. Akinci, A. and H. Eyidoğan, "Scattering and anelastic attenuation of seismic energy in the vicinity of north anatolian fault zone, eastern Turkey", *Physics of the Earth and Planetary Interiors*, Vol. 122, No. 3-4, pp. 229–239, dec 2000.

14. Hoshiba, M., A. Rietbrock, F. Scherbaum and H. Nakahara, "Scattering attenuation and intrinsic absorption using uniform and depth dependent model – Application to full seismogram envelope recorded in Northern Chile", *Journal of Seismology*, pp. 157–179, 2001.

15. Bianco, F., E. Del Pezzo, M. Castellano, J. Ibanez and F. Di Luccio, "Separation of intrinsic and scattering seismic attenuation in the Southern Apennine zone, Italy", *Geophysical Journal International*, Vol. 150, No. 1, pp. 10–22, jul 2002.

16. Bianco, F., E. D. Pezzo, L. Malagnini, F. D. Luccio and A. Akinci, "Separation of depth-dependent intrinsic and scattering seismic attenuation in the northeastern sector of the Italian Peninsula", *Geophysical Journal International*, Vol. 161, No. 1, pp. 130–142, apr 2005.

17. Tuvè, T., F. Bianco, J. Ibáñez, D. Patanè, E. Del Pezzo and A. Bottari, "Attenuation study in the Straits of Messina area (southern Italy)", *Tectonophysics*, Vol. 421, No. 3-4, pp. 173–185, aug 2006.

18. Şahin, Ş., M. Erduran, Ö. Alptekin and Ö. Çakir, "Intrinsic and scattering seismic attenuation in Southwestern Anatolia", *Pure and Applied Geophysics*, 2007.

19. Mukhopadhyay, S., J. Sharma, E. Del-Pezzo and N. Kumar, "Study of attenuation mechanism for Garwhal–Kumaun Himalayas from analysis of coda of local earthquakes", *Physics of the Earth and Planetary Interiors*, Vol. 180, No. 1-2, pp. 7–15, may 2010.

20. Carcolé, E. and H. Sato, "Spatial distribution of scattering loss and intrinsic absorption of short-period S waves in the lithosphere of Japan on the basis of the Multiple Lapse Time Window Analysis of Hi-net data", *Geophysical Journal International*, Vol. 180, No. 1, pp. 268–290, 2010.

21. Şengör, A. and Y. Yılmaz, "Tethyan evolution of Turkey: A plate tectonic approach", *Tectonophysics*, Vol. 75, No. 3-4, pp. 181–241, jun 1981.

22. Tatar, O., J. D. Piper, H. Gürsoy and H. Temiz, "Regional significance of neotectonic counterclockwise rotation in central turkey", *International Geology Review*, 1996.

23. Gürsoy, H., J. D. Piper, O. Tatar and L. Mesci, "Palaeomagnetic study of the Karaman and Karapinar volcanic complexes, central Turkey: Neotectonic rotation in the south-central sector of the Anatolian Block", *Tectonophysics*, 1998.

24. Piper, J. D., H. Gürsoy and O. Tatar, "Palaeomagnetism and magnetic properties of the Cappadocian ignimbrite succession, central Turkey and Neogene tectonics of the Anatolian collage", *Journal of Volcanology and Geothermal Research*, 2002.

25. Bozkurt, E., "Neotectonics of Turkey – a synthesis", *Geodinamica Acta*, Vol. 14, No. 1-3, pp. 3–30, may 2001.

26. Koçyiğit, A. and A. Beyhan, "A new intracontinental transcurrent structure: The Central Anatolian Fault Zone, Turkey", *Tectonophysics*, 1998.

27. Dirik, K. and M. C. Göncüoglu, "Neotectonic characteristics of central anatolia", *International Geology Review*, 1996.

28. Çemen, I., M. Göncüoglu and K. Dirik, "Structural Evolution of the Tuzgölü Basin in Central Anatolia, Turkey.", *The Journal of geology*, 1999.

29. Pearce, J. A., J. F. Bender, S. E. De Long, W. S. Kidd, P. J. Low, Y. Güner, F. Saroglu, Y. Yilmaz, S. Moorbath and J. G. Mitchell, "Genesis of collision volcanism in Eastern Anatolia, Turkey", *Journal of Volcanology and Geothermal Research*, 1990.

30. Al-Lazki, A. I., E. Sandvol, D. Seber, M. Barazangi, N. Turkelli and R. Mohamad, "Pn tomographic imaging of mantle lid velocity and anisotropy at the junction of the Arabian, Eurasian and African plates", *Geophysical Journal International*, 2004.

31. Gök, R., E. Sandvol, N. Türkelli, D. Seber and M. Barazangi, "Sn attenuation in the Anatolian and Iranian plateau and surrounding regions", *Geophysical Research Letters*, Vol. 30, No. 24, 2003.

32. Gans, C. R., S. L. Beck, G. Zandt, C. B. Biryol and A. A. Ozacar, "Detecting the limit of slab break-off in central Turkey: new high-resolution Pn tomography results", *Geophysical Journal International*, Vol. 179, No. 3, pp. 1566–1572, dec

2009.

33. Mutlu, A. K. and H. Karabulut, "Anisotropic Pn tomography of Turkey and adjacent regions", *Geophysical Journal International*, 2011.

34. Schivardi, R. and A. Morelli, "EPmantle: A 3-D transversely isotropic model of the upper mantle under the European Plate", *Geophysical Journal International*, 2011.

35. Shearer, P., *Introduction to Seismology*, Cambridge University Press, 2009.

36. Lay, T. and T. C. Wallace, *Modern global seismology*, Academic Press, 1995.

37. Stein, S. and M. Wysession, *An introduction to seismology, earthquakes, and earth structure*, Blackwell Pub, 2003.

38. Aki, K., "Analysis of the seismic coda of local earthquakes as scattered waves", *Journal of Geophysical Research*, Vol. 74, No. 2, pp. 615–631, 1969.

39. Rautian, T. and V. Khalturin, "The use of the coda for determination of the earthquake source spectrum", *Bulletin of the Seismological Society of America*, Vol. 68, No. 4, pp. 923–948, aug 1978.

40. Aki, K., "Source and scatering effects on the spectra of small local earthquakes", *Bulletin of the Seismological Society of America*, Vol. 71, No. 6, pp. 1687–1700, 1981.

41. Frankel, A. and R. W. Clayton, "Finite difference simulations of seismic scattering: Implications for the propagation of short-period seismic waves in the crust and models of crustal heterogeneity", *Journal of Geophysical Research*, Vol. 91, No. B6, p. 6465, 1986.

42. Matsunami, K., "Laboratory tests of excitation and attenuation of coda waves using 2-D models of scattering media", *Physics of the Earth and Planetary Interiors*,

Vol. 67, No. 1-2, pp. 36–47, 1991.

43. Aki, K. and B. Chouet, "Origin of coda waves: Source, attenuation, and scattering effects", *Journal of Geophysical Research*, Vol. 80, No. 23, pp. 3322–3342, aug 1975.

44. Sato, H., "Energy propagation including scattering effects sengle isotropic scattering approximation", *Journal of Physics of the Earth*, Vol. 25, No. 1, pp. 27–41, 1977.

45. Wu, R. S., "Multiple scattering and energy transfer of seismic waves – separation of scattering effect from intrinsic attenuation – I. Theoretical modelling", *Geophysical Journal of the Royal Astronomical Society*, Vol. 82, No. 1, pp. 57–80, 1985.

46. Zeng, Y., F. Su and K. Aki, "Scattering wave energy propagation in a random isotropic scattering medium: 1. Theory", *Journal of Geophysical Research*, Vol. 96, No. B1, p. 607, 1991.

47. Hoshiba, M., "Simulation of multiple-scattered coda wave excitation based on the energy conservation law", *Physics of the Earth and Planetary Interiors*, Vol. 67, No. 1-2, pp. 123–136, 1991.

48. Wessel, P., W. H. F. Smith, R. Scharroo, J. Luis and F. Wobbe, "Generic Mapping Tools: Improved Version Released", *Eos, Transactions American Geophysical Union*, Vol. 94, No. 45, pp. 409–410, nov 2013.

49. Hoshiba, M., "Seismic coda wave envelope in depth-dependent S wave velocity structure", *Physics of the Earth and Planetary Interiors*, Vol. 104, No. 1-3, pp. 15–22, nov 1997.

50. Frankel, A. and L. Wennerberg, "Energy-flux model of seismic coda: Separation of scattering and intrinsic attenuation", *Bulletin of the Seismological Society of America*, Vol. 77, No. 4, pp. 1223–1251, 1987.

51. Sato, H., "Energy Transportation In One and Two-Dimensional Scattering Media: Analytic Solutions of the Multiple Isotropic Scattering Model: Energy transportation in one and two-dimensional scattering media", *Geophysical Journal International*, Vol. 112, No. 1, pp. 141–146, 1993.

52. Mamada, Y. and H. Takenaka, "Comparison of Q-C1 Estimates from Coda Envelopes Constructed from One- and Multi-Component Seismograms.", *Journal of Physics of the Earth*, Vol. 45, No. 6, pp. 455–466, 1997.

53. Aki, K., "Scattering and attenuation of shear waves in the lithosphere", *Journal of Geophysical Research*, Vol. 85, No. B11, p. 6496, 1980.

54. Hoshiba, M., "Simulation of coda wave envelope in depth dependent scattering and absorption structure", *Geophysical Research Letters*, Vol. 21, No. 25, pp. 2853–2856, dec 1994.

55. Beyreuther, M., R. Barsch, L. Krischer, T. Megies, Y. Behr and J. Wassermann, "ObsPy: A Python Toolbox for Seismology", *Seismological Research Letters*, Vol. 81, No. 3, pp. 530–533, may 2010.

56. Hunter, J. D., "Matplotlib: A 2D Graphics Environment", *Computing in Science & Engineering*, Vol. 9, No. 3, pp. 90–95, 2007.

57. Al-Lazki, A. I., D. Seber, E. Sandvol, N. Turkelli, R. Mohamad and M. Barazangi, "Tomographic Pn velocity and anisotropy structure beneath the Anatolian plateau (eastern Turkey) and the surrounding regions", *Geophysical Research Letters*, Vol. 30, No. 24, dec 2003.

58. Gök, R., M. E. Pasyanos and E. Zor, "Lithospheric structure of the continent-continent collision zone: eastern Turkey", *Geophysical Journal International*, Vol. 169, No. 3, pp. 1079–1088, jun 2007.

59. Berk Biryol, C., S. L. Beck, G. Zandt and A. A. Özacar, "Segmented African

lithosphere beneath the Anatolian region inferred from teleseismic P-wave tomography", *Geophysical Journal International*, Vol. 184, No. 3, pp. 1037–1057, mar 2011.

60. Chung, T. W., K. Yoshimoto and S. Yun, "The Separation of Intrinsic and Scattering Seismic Attenuation in South Korea", *Bulletin of the Seismological Society of America*, Vol. 100, No. 6, pp. 3183–3193, dec 2010.

61. Pasyanos, M. E. and W. R. Walter, "Improvements to regional explosion identification using attenuation models of the lithosphere", *Geophysical Research Letters*, Vol. 36, No. 14, p. L14304, jul 2009.

APPENDIX A: EVENT LIST

Table A.1: The event list of the thesis.

NO	DATE	TIME	LON	LAT	DEPTH	MAG
1	20090607	234108,4	32,8682	39,3567	3,0	3,1
2	20090611	155438,4	33,0178	39,5032	5,3	3,1
3	20090712	053017.65	32,9700	39,5155	5,0	3,4
4	20090722	171744.00	33,0420	39,5503	5,0	3
5	20090723	030629.52	32,9598	39,5198	5,0	3,2
6	20090728	073313.38	33,0445	39,4477	5,0	3,4
7	20090820	072328.00	33,1097	39,3080	5,0	3
8	20090918	085606.52	33,2373	39,5718	2,1	3,1
9	20091011	034249.00	33,0435	39,4225	5,0	3
10	20091015	005153.98	33,0517	39,4597	5,2	3
11	20091102	122449.40	33,2015	39,2252	7,1	3,2
12	20091119	221347.17	33,0950	39,4435	3,2	3,2
13	20091203	223948.42	33,1332	39,3457	6,4	3,2
14	20091224	004254.53	33,0693	39,4178	5,3	3,2
15	20091229	222549.77	33,0860	39,5115	5,0	3,1
16	20100108	120932.83	32,9972	39,4858	2,4	3,6
17	20100122	174815.50	33,1532	39,1597	10,6	3
18	20100212	025424.54	33,1480	39,3698	6,3	3,2
19	20100212	035840.10	33,0542	39,3533	5,0	3,2
20	20100212	173735.32	33,1853	39,3835	7,6	3
21	20100213	041411.07	33,1350	39,3635	6,0	3
22	20100213	131619.20	33,1657	39,3378	13,8	3,2
23	20100215	201553.80	32,9922	39,4587	5,0	3,3
24	20100218	180047.37	33,1715	39,3420	5,0	3,3
25	20100221	023437.62	33,0323	39,4548	5,0	3,4
26	20100221	205424.65	33,0150	39,4485	2,3	3,4

Table A.1 continued from previous page

NO	DATE	TIME	LON	LAT	DEPTH	MAG
27	20100316	171240.47	33,0517	39,4785	4,9	3
28	20100319	062133.53	33,1497	39,3852	4,6	3,4
29	20100402	021852.25	33,0770	39,3828	8,6	3
30	20100417	004907.78	33,0612	39,4868	5,0	3
31	20100709	082752.00	33,0897	39,4108	5,0	3
32	20100727	195817.28	33,2343	39,1213	2,3	3,2
33	20100728	125243.14	33,2735	39,1438	5,0	3,2
34	20100912	182514.37	32,8260	39,5920	5,0	3,5
35	20100919	191632.94	33,0470	39,4578	5,3	3
36	20100929	221800.50	33,2448	39,2597	5,0	3,1
37	20101019	143212.96	33,1285	39,4032	3,5	3,9
38	20101103	042108.47	33,1148	39,3972	2,3	3,3
39	20101118	014539.07	33,2295	39,5455	5,0	3,1
40	20110317	225037.37	33,0683	39,4275	4,1	3,2
41	20090609	121150,10	32,0233	39,3483	7,0	2,9
42	20090704	171852,36	32,4723	39,0128	5,0	3
43	20090725	030308,92	32,5002	38,7852	8,2	2,9
44	20090818	215223,07	32,2332	39,4507	5,0	3,4
45	20090823	114350,47	34,4762	39,1840	5,2	3
46	20090823	215201,16	34,4838	39,1652	2,6	3,1
47	20090824	013341,17	33,7423	39,8275	5,0	3,2
48	20090826	194443,11	34,4728	39,1545	2,2	3,3
49	20090827	214349,69	34,4987	39,1860	5,0	3,2
50	20090902	044117,63	32,8953	39,0832	5,0	3
51	20090902	204354,39	32,8290	39,1285	3,7	3,3
52	20090902	211548,84	32,8608	39,1392	2,3	3
53	20090918	034618,34	34,0782	39,9597	5,0	3
54	20090926	043346,59	32,9210	38,8177	13,4	3,3

Table A.1 continued from previous page

NO	DATE	TIME	LON	LAT	DEPTH	MAG
55	20091003	192518,22	32,7953	39,1045	5,0	3,1
56	20091016	092307,96	32,7912	39,1145	2,8	3,6
57	20091016	221020,92	32,6775	39,5135	5,0	3,1
58	20091029	163053,14	32,8580	39,0882	7,9	3,3
59	20091103	073341,86	33,3178	39,7675	6,1	3,3
60	20091113	041019,81	33,0887	39,0547	12,1	3,8
61	20091123	162933,19	32,9092	39,0373	5,0	3,3
62	20091124	155219,74	32,7218	39,2322	5,7	3,1
63	20091210	015759,27	33,1392	39,9337	5,4	2,9
64	20091229	134627,49	34,1572	40,1510	5,0	3,3
65	20100109	213333,04	33,3968	39,8450	16,2	3
66	20100117	193724,85	33,5872	38,7063	7,6	3,1
67	20100201	082710,20	32,7600	38,3200	7,0	3
68	20100215	052509,67	32,7382	39,9893	5,0	3
69	20100323	075928,21	33,9485	40,0432	5,0	3,5
70	20100420	005311,78	32,9723	38,6877	7,7	3,5
71	20100420	120008,73	33,5733	39,9737	6,1	3,1
72	20100430	163654,40	32,7492	39,9413	2,5	3,5
73	20100509	035824,66	34,6688	40,0752	4,9	3,6
74	20100804	113228,10	33,9610	38,4445	5,0	3,2
75	20100919	021156,48	33,4455	38,3012	5,3	3,1
76	20101116	053047,29	33,3798	38,6470	7,7	3
77	20110110	084429,92	34,1835	39,6062	6,2	3
78	20110114	154151,70	34,9205	39,0180	5,0	3,2
79	20110219	032818,01	34,5312	39,0087	5,0	3,2
80	20110224	034226,77	32,5137	38,0090	5,0	3,2
81	20110224	130748,47	33,4682	38,2852	5,0	3,2
82	20110301	193013,52	33,1787	39,8302	5,0	3,3

Table A.1 continued from previous page

NO	DATE	TIME	LON	LAT	DEPTH	MAG
83	20080104	050313.00	33,1643	39,3732	5,0	4
84	20080201	091103.37	33,0655	39,4143	5,0	4,1
85	20080731	050209.62	33,3500	39,7268	5,0	4,2
86	20080911	083358.20	33,0700	39,4067	5,0	4,1
87	20080923	090942.50	33,0425	39,4627	4,0	4,5
88	20081010	063655.13	35,5577	38,8280	8,2	4,6
89	20090620	221203.42	33,2745	39,1090	6,2	2,9
90	20090621	161250.78	35,5028	38,8143	5,4	2,8
91	20090826	151430.16	35,5977	38,8165	15,4	2,8
92	20090826	201804.61	32,8742	39,0783	6,2	2,9
93	20090910	182952,06	32,5197	37,9422	2,0	4,7
94	20091006	225811.78	34,2982	39,7515	6,9	2,8
95	20091212	100501.36	32,9165	40,2490	5,4	2,9
96	20091213	104503.44	32,7917	40,0510	2,9	2,9
97	20091221	051236.87	33,1865	39,3505	7,5	2,9
98	20100203	051116.20	33,9000	39,1600	5,0	2,8
99	20100320	221652.77	33,5200	37,8113	9,4	2,9
100	20100322	140132.76	33,5727	39,9733	6,6	2,8
101	20100323	081029.95	33,9343	39,9828	5,8	2,9
102	20100408	142931.41	31,8125	39,5775	5,0	2,8
103	20100413	071614.65	32,9608	38,7005	5,3	2,9
104	20100428	105615.74	34,1003	38,4873	3,9	2,8
105	20100503	143349.63	32,3872	39,9572	7,8	2,8
106	20100616	135545.17	31,9803	39,2320	5,0	2,9
107	20100716	001304.83	34,6427	40,0847	5,3	2,9
108	20100718	023926.11	34,3732	39,5348	16,5	2,8
109	20100808	111413.73	33,6343	38,9367	3,3	2,8
110	20100813	091600.76	34,7928	39,5050	5,0	2,8

Table A.1 continued from previous page

NO	DATE	TIME	LON	LAT	DEPTH	MAG
111	20100814	021051.78	32,2742	39,0330	6,8	2,8
112	20100924	220707.65	32,5623	38,8038	5,5	2,8
113	20101119	062133.63	33,2745	37,8730	5,0	2,9
114	20101224	090950.07	35,1763	38,7387	7,0	2,8
115	20110219	185626.32	33,4213	40,3068	5,0	2,9
116	20110224	082203.75	34,9208	37,9208	5,0	2,9
117	20110306	183758.56	34,3807	40,4117	7,6	2,9
118	20110308	164822.80	34,7060	39,7313	9,4	2,8
119	20110330	000921.71	32,3120	38,3388	7,3	2,9
120	20110613	113025.89	33,9202	38,3463	5,0	3,9
121	20090713	223003,88	34,0970	39,8428	5,0	2,8
122	20090715	134809,15	31,9640	39,3353	5,0	2,8
123	20090724	103724,3	35,5853	38,7573	5,0	3
124	20090816	161001,07	34,5518	39,5493	5,4	3
125	20090822	135159,57	32,2650	37,8813	2,1	2,5
126	20090904	015729,29	33,8187	39,5312	5,4	2,8
127	20090906	173000,13	33,5687	37,8340	6,8	3,3
128	20090911	073221,05	32,4760	37,9093	4,8	3,5
129	20090920	224200,64	32,3373	37,8557	7,7	2,8
130	20090927	210120,60	32,6808	40,1735	4,3	3,6
131	20091004	223621,25	34,1077	39,9950	3,4	3,6
132	20091019	005201,16	32,7152	38,4875	5,5	2,7
133	20091021	072100.99	34,5817	39,5315	5,6	2,7
134	20091110	052014,14	33,3760	40,4465	5,4	3,6
135	20091123	103620,04	35,6832	38,6903	5,1	3,1
136	20091208	165251,29	33,8722	37,9368	7,7	3,3
137	20100112	130311,73	32,5460	38,1222	12,0	2,8
138	20100208	233410,41	33,5080	38,6778	10,9	2,9

Table A.1 continued from previous page

NO	DATE	TIME	LON	LAT	DEPTH	MAG
139	20100225	220001,66	33,1925	39,9452	5,6	2,9
140	20100226	152045,36	32,0098	39,3342	5,0	2,9
141	20100319	114452,04	31,9670	39,1968	5,0	3,1
142	20100321	180024,19	31,9270	38,8148	4,8	3,6
143	20100328	074927,29	32,8863	38,7302	11,5	2,9
144	20100330	034504,46	33,1603	38,4342	9,6	2,9
145	20100613	154821,23	33,0168	37,9198	9,2	2,9
146	20100805	132111,07	34,9732	40,2377	5,0	2,6
147	20100901	151547,51	34,3278	39,1670	8,4	2,8
148	20100928	222019,78	33,3455	38,9382	6,0	2,9
149	20101012	145522,01	34,0738	38,3133	4,3	2,9
150	20101013	034538,44	33,9528	40,2083	5,0	2,8
151	20101020	051633,02	34,7480	38,1538	4,0	2,7
152	20101102	141258,50	31,9903	39,6808	7,2	3,1
153	20101106	131537,08	34,2443	39,0947	5,0	2,8
154	20101112	112918,86	31,6368	39,6238	5,0	2,7
155	20101204	202448,58	32,9873	38,1428	7,9	2,8
156	20101207	142241,23	35,6650	38,9370	5,6	3
157	20101226	072322,58	35,8297	39,0010	3,8	3,2
158	20110103	132903,99	32,3955	39,9277	8,7	2,8
159	20110118	182734,57	33,8295	38,9987	5,4	2,6
160	20110128	083652,48	34,1748	38,4830	11,3	2,5
162	20110207	140450,02	33,4335	39,9795	7,9	2,9
161	20110207	052629,95	34,1323	40,4928	5,2	3,2
163	20110215	154234,14	32,4785	38,0098	6,1	2,7
164	20110219	140734,07	34,2428	38,3438	16,8	2,9
165	20110226	024249,13	33,5237	38,2778	22,4	2,6
166	20110312	213653,58	33,8273	39,9107	12,3	2,8

Table A.1 continued from previous page

NO	DATE	TIME	LON	LAT	DEPTH	MAG
167	20110323	225008,96	34,9425	39,9950	6,9	3,1
168	20110424	033131,14	31,9075	38,6617	4,6	3
169	20110429	044102,90	33,6000	37,8205	4,6	3,2
170	20110604	185201,31	34,6652	40,0738	4,9	3,1
171	20110605	015459,90	33,6020	38,7372	5,0	3,2
172	20110609	065241,28	32,2358	39,2040	7,0	2,9
173	20110612	054419,16	32,9068	40,4508	5,0	3,4
174	20110614	191600,91	32,9568	40,4087	5,2	3,2
175	20110630	184236,48	35,1668	38,2390	5,0	3,4
176	20110722	053436,38	31,8002	38,4795	5,0	3,2
177	20110728	042805,10	31,8588	38,2838	4,5	2,5